

SPATTER, SCORIA BOMBS, AND UPPER MANTLE XENOLITHS:  
COOLING HISTORIES OF ROCKS IN THREE TERRESTRIAL SETTINGS

A Dissertation

Presented in Partial Fulfillment for the Requirements for the

Degree of Doctorate of Philosophy

with a

Major in Geology

in the

College of Graduate Studies

University of Idaho

by

Erika Rader

May 2014

Major Professor: Dennis Geist, Ph.D.

### Authorization to Submit Dissertation

This dissertation of Erika Rader, submitted for the degree of Doctor of Philosophy with a major in Geology and titled “Spatter, Scoria Bombs, and Upper Mantle Xenoliths: Cooling Histories of Rocks in Three Terrestrial Settings,” has been reviewed in final form. Permission, as indicated by the signatures and dates below, is now granted to submit final copies to the College of Graduate Studies for approval.

Major Professor: \_\_\_\_\_ Date: \_\_\_\_\_  
Dennis Geist, Ph.D.

Committee  
Members: \_\_\_\_\_ Date: \_\_\_\_\_  
Karen Harpp, Ph.D.

\_\_\_\_\_ Date: \_\_\_\_\_  
John Wolff, Ph.D.

\_\_\_\_\_ Date: \_\_\_\_\_  
Josef Dufek, Ph.D.

Department  
Administrator: \_\_\_\_\_ Date: \_\_\_\_\_  
Mickey Gunter, Ph.D.

Discipline’s  
College Dean: \_\_\_\_\_ Date: \_\_\_\_\_  
Paul Joyce, Ph.D.

Final Approval and Acceptance:

Dean of the College  
of Graduate Studies: \_\_\_\_\_ Date: \_\_\_\_\_  
Jie Chen, Ph.D.

**Abstract**

The thermal history of a rock can provide information about a process that is much larger than the rock itself. In this dissertation, I present three studies that evaluate a larger earth process that is illuminated by the speed and conditions of cooling or heating each rock type experienced. Chapter 1 looks at how a chemical boundary layer might form in the upper mantle due to the cooling path that hydrated cratonic lithosphere takes. I study this seismically-distinct layer using the geochemistry of xenoliths I retrieved from the online database, PetDB. Chapter 2 and 3 use the cooling history of volcanic products to evaluate surface processes. The second chapter illustrates how the cooling history of lithic and juvenile clasts in pyroclastic density currents reveal that boiling-over eruptions result in high air entrainment and a thermally heterogeneous deposit. The final chapter characterizes spatter, an explosive volcanic product, at Devil's Garden, OR and quantifies the accumulation and cooling rates required to produce spatter deposits.

**Acknowledgments**

I would like to thank the people and institutions who made this project possible. Thanks to my advisor, Dennis Geist, and my committee, who helped guide me through this process and provided many helpful comments. My fieldwork for these projects was assisted by Madison Myers, Mary Benage, Nick Pollock, Jesse Meyers, Alexa Van Eaton, Frankie Daschell, and Matthew Pendleton. Funding was primarily provided by the National Science Foundation as well as additional funding by the University of Idaho and National Aeronautics and Space Administration.

Further assistance was provided by Debbie Jensen, Mickey Gunter, Tom Williams, David Alexander, Katherine Cooper, Eric Mittelstaedt, Thomas Morrow, and Helena Buurman. I also want to thank my family for being loving, supportive, and persistent.

### **Dedication**

The accomplishment that this document represents is dedicated to Jessica and Mickey who, along with my family, encouraged my whole existence.

## Table of Contents

Authorization to Submit Dissertation .....	ii
Abstract.....	iii
Acknowledgements .....	iv
Dedication.....	v
Table of Contents.....	vi
List of Figures .....	ix
List of Tables .....	xi
<b>Chapter 1. Introduction .....</b>	<b>1</b>
<b>Chapter 2. Characterization and petrologic constraints of the mid-lithospheric discontinuity ..</b>	<b>5</b>
1. Abstract.....	6
2. Introduction .....	7
3. Methods.....	9
3.1 The seismological database .....	9
3.2 Geochemistry and petrology of xenoliths .....	10
4. Seismological results.....	10
4.1 Active source seismology.....	10
4.2 Surface waves .....	11
4.3 Receiver functions .....	11
4.4 Underside reflections .....	12
4.5 ScS reverberations .....	13
4.6 Summary of seismic results .....	13
5. Results for xenoliths .....	13
6. Discussion .....	14
6.1 Seismic characteristics of the MLD .....	14
6.2 Shear wave velocity modeling .....	14
6.3 A stalled melt layer .....	15
6.4 Relationship to the LAB .....	16
7. Conclusions .....	16
8. Acknowledgements .....	17

8 References .....	17
<b>Chapter 3. Hot clasts and cold blasts: Thermal heterogeneity in boiling-over pyroclastic density currents .....</b>	<b>41</b>
1. Introduction .....	41
2. Background .....	42
2.1 Location and eruptive history .....	42
2.2 Pyroclastic density currents from boiling-over eruptions .....	43
2.3 Estimation of temperature of volcanic deposits using paleomagnetic methods .....	44
3. Methods .....	46
3.1 Sample collected and preparation .....	46
3.2 Magnetization measurements .....	46
4. Results .....	47
4.1 Description of deposits .....	47
4.2 Rock magnetism .....	47
4.3 Juvenile clasts .....	48
4.4 Lithic clasts .....	49
5. Discussion .....	50
5.1 Emplacement temperatures at Tungurahua and Cotopaxi .....	50
5.2 Thermal heterogeneity of boiling-over pyroclastic density currents .....	52
5.3 Scoria-rich pyroclastic density currents .....	53
5.4 Model of thermal heterogeneity .....	53
5.5 Importance of sampling lithic and juvenile clasts .....	54
5.6 Implication of boiling-over pyroclastic density currents for hazard assessment .....	55
6. Conclusions .....	56
7. Acknowledgements .....	57
<b>Chapter 4. The use of spatter deposits to constrain eruption conditions .....</b>	<b>79</b>
1. Introduction .....	79
1.1 Importance of understanding basaltic eruptions .....	79
1.2 Spatter: A poorly quantified yet distinct field indicator .....	80
2. Field characteristics of spatter .....	80
2.1 Location description .....	80

2.2 Spatter deposits at Devil's Garden .....	81
2.3 Morphology of spatter deposits .....	82
2.4 Glaze on spatter .....	82
2.5 Textural descriptions of natural samples .....	83
3. Thermal experiments.....	83
3.1 Temperature range of spatter deposits .....	83
3.2 Cooling rates of spatter .....	83
3.3 Experimental methodology .....	84
3.4 Eruption temperature.....	84
3.5 Tensile strength measurements .....	85
3.6 Weld strength .....	85
3.7 Cooling rate of deposit .....	85
3.8 Failed experiments .....	86
4. Accumulation rates in explosive basaltic eruptions .....	86
4.1 Cooling model of repeated deposition of spatter clasts .....	86
4.2 Accumulation rate of Devil's Garden spatter deposits.....	87
4.3 Constraints on eruption of spatter .....	87
5. Conclusion.....	88

## List of Figures

2.1 Generalized shear velocity profile underneath a continent .....	32
2.2 Ray paths for the seismic methods used to image the MLD .....	33
2.3 Geographic distributions of seismic detections of the MLD.....	34
2.4 Spatial frequency of observed depths of the MLD .....	35
2.5 Pressure and temperatures of hydrous mineral-bearing xenoliths.....	36
2.6 Selected trace element ratios for xenoliths.....	37
2.7 Effect of adding proportion of minerals to peridotite on shear velocity.....	38
2.8 Perple_X models of elastic properties of mantle rock mixtures .....	39
2.9 Dynamical model of the formation of a trapped melt layer.....	40
3.1 Location map of Tungurahua and Cotopaxi in Ecuador.....	65
3.2. Map showing the extent of pyroclastic flows and sample locations.....	66
3.3 Photo of Tungurahua emitting a boiling-over pyroclastic density current.....	67
3.4 Field photographs showing juvenile bombs at both Cotopaxi and Tungurahua sagging under their own weight .....	68
3.5 Pyroclastic flows are largely channelized in steep-sided quebradas.....	69
3.6 Plots of bulk, low field susceptibility from Cotopaxi.....	70
3.7 Plots of bulk, low field susceptibility from Tungurahua .....	71
3.8 Orthogonal demagnetization diagram of typical juvenile clast.....	72
3.9 Equal area projection of juvenile clasts .....	73
3.10 Equal area projections of lithic clasts .....	74
3.11 Orthogonal demagnetization diagrams showing two juvenile samples from Cotopaxi that do not align with NRM .....	75
3.12 Orthogonal demagnetization diagram showing the response by a juvenile sample from Tu-10-07 .....	76
3.13 Orthogonal demagnetization illustrating that the abrupt change in declination .....	77
3.14 Example of a thermal model to constrain the temperature .....	78
4.1 Location map of Devil's Garden Volcanic Field.....	98
4.2 Aerial image of the Blowouts, Devil's Garden .....	99
4.3 Photo of cross-section of spatter pile at the Blowouts .....	100
4.4 Drips on the inside of Devil's Hot tub .....	101

4.5 Slopes of scoria cones and spatter vents.....	102
4.6 Photo of two examples of glaze at Devil's Garden .....	103
4.7 Photomicrograph and SEM image of glaze from Devil's Garden.....	104
4.8 Cubes of sample stacked on a graphite plate .....	105
4.9 The tensile strength of artificial welds.....	106
4.10 Model of the interrelationship of accumulation rate, deposit thickness, and clast size....	107
4.11 Model results for cooling and accumulation rates for 5 cm clasts.....	108
4.12 Schematic diagram for explosive basaltic products .....	109

**List of Tables**

2.1 Seismological database .....	25
2.2 Depths of xenoliths .....	28
2.3 Selected trace elements for xenoliths .....	31
3.1 Estimated minimum emplacement temperatures .....	64
4.1 Chemical analyses of Devil’s Garden lava .....	92
4.2 Height and width comparisons between spatter vents and scoria cones .....	93
4.3 Modal mineralogy of spatter clasts from Devil’s Garden .....	94
4.4 Experimental and natural cooling rates of spatter .....	95
4.5 Thermal constants used in model .....	96
4.6 Cooling rates for modeled accumulation rates .....	97

## Chapter 1. Introduction

All igneous rocks exposed at the earth's surface start hot and end cold, but the path they take can vary greatly. This dissertation comprises three studies in which the cooling history of rocks can reveal fundamental knowledge about the igneous processes that create cratonic lithosphere, boiling-over pyroclastic density currents, and spatter ramparts. The methods used to study these rocks include geochemistry, experimental volcanology, seismology, and paleomagnetism.

Chapter Two addresses the question of how cratons remain stable over billions of years. Most hypotheses invoke a 'keel' of buoyant mantle lithosphere, which prevents recycling of the crustal material (e.g., Lenardic et al., 2003; King, 2005). The ancient timing of building cratons, and how they resist subduction, remains contentious (Campbell, 2003). A key component to understanding how cratonic lithosphere stabilizes involves the structures within cratonic lithosphere. (e.g., Bapanayya et al., 2011; Chu et al., 2012; O'Donnell et al., 2013). I propose a cooling history for cratonic lithosphere based on the geochemistry of xenoliths that sample the low-velocity zone known as the mid-lithospheric discontinuity (MLD). The chapter begins by reviewing seismic observations of the MLD from the literature and discusses the robustness of the various methods researchers have used to image the MLD (this section was largely written by student colleagues). I use geochemical data from mantle xenoliths from depths and locations consistent with the MLD to evaluate the lithologic constitution of the layer. I propose that the boundary formed due to melt transfer and a cooling history that concentrates hydrous minerals at the depth at which the MLD is observed.

Cooling rates of explosive volcanic rocks are important indicators of eruptive processes. One of the most destructive hazards of intermediate-composition volcanoes is pyroclastic density currents (e.g., Tilling, 2009; Perucca & Moreiras, 2009; Power et al., 1998). Pyroclastic density currents can only be studied remotely and through their deposits. In addition to gaseous, ballistic, and burial hazards, pyroclastic density currents also pose a thermal hazard (Parshley et al., 1982; Fujii & Nakada, 1999; Baxter et al., 2005). Chapter Three focuses on the cooling of boiling-over pyroclastic density currents, which are produced at moderately explosive volcanoes and typically occur from eruptions that do not result in a large convective plume (Branney & Kokelaar, 2002; Wolf, 1878; Hall et al. 2013; Clarke et al. 2002). The moderate energy output and the mode of transport of all PDCs have implications for the temperature of the final deposits. Paleomagnetism can be used to constrain the cooling history of volcanic deposits (e.g., Paterson et al., 2010; McClelland et al., 2004), because it is set as a rock cools

from above the Curie temperature ( $\sim 590^{\circ}\text{C}$ ). I report detailed measurements on samples taken from rims-to-cores of juvenile and lithic clasts from boiling-over PDC deposits erupted at Tungurahua and Cotopaxi volcanoes. The paleomagnetism of juvenile clasts and lithic clasts records the maximum and minimum temperature of the PDC deposit as a whole. I have discovered extraordinary thermal heterogeneity in these deposits and hypothesize on the origins of that heterogeneity.

Chapter Four addresses another type of volcanism that is not well understood: basaltic spatter-producing eruptions. Most basaltic eruptions produce spatter, and they are the most common eruption on Earth and all of the terrestrial planets (Self et al., 1998; Keszthelyi et al., 2000). Additionally, spatter deposits are important for identifying the eruptive vent for expansive flood basalts (Hooper, 1997; Reidel, 1998; Self et al., 1997; Nemeth et al., 2003). A qualitative model proposes that spatter accumulates faster and cools slower than scoria, but accumulates slower and cools faster than lava (Sumner et al., 2005). I use field observations and experiments to assess the cooling rate of spatter deposits at Devil's Garden, Oregon, USA. The spatter deposits at Devil's Garden are ideal for study as they are relatively fresh and easily accessible. After constraining cooling rates by comparing experimental simulations of natural samples, I model the rate of accumulation for a cooling deposit. Since the morphology of basalt is depended on eruption conditions (such as accumulation and cooling rate), these constrains allow eruption conditions to be determined by the presence of eruptive products, such as scoria and spatter. This model can be applied to any spatter deposit, via observation of deformation textures and measurement of the tensile strength of welded spatter clasts.

#### References:

- Bapanayya, C., Raju, P. A., Sharma, S. D., & Ramesh, D. S. (2011). Information theory-based measures of similarity for imaging shallow-mantle discontinuities. *Lithosphere*, 3(4), 289-303.
- Baxter, P. J., Boyle, R., Cole, P., Neri, A., Spence, R., & Zuccaro, G. (2005). The impacts of pyroclastic surges on buildings at the eruption of the Soufrière Hills volcano, Montserrat. *Bulletin of volcanology*, 67(4), 292-313.
- Branney, M. J., & Kokelaar, B. P. (2002). Pyroclastic density currents and the sedimentation of ignimbrites. Geological Society of London.
- Campbell, I. H. (2003). Constraints on continental growth models from Nb/U ratios in the 3.5 Ga

- Barberton and other Archaean basalt-komatiite suites. *American Journal of Science*, 303(4), 319-351.
- Chu, R., Schmandt, B., & Helmberger, D. V. (2012). Upper mantle P velocity structure beneath the Midwestern United States derived from triplicated waveforms. *Geochemistry, Geophysics, Geosystems*, 13(2).
- Clarke, A. B., Voight, B., Neri, A., & Macedonio, G. (2002). Transient dynamics of vulcanian explosions and column collapse. *Nature*, 415(6874), 897-901.
- Fujii, T., & Nakada, S. (1999). The 15 September 1991 pyroclastic flows at Unzen Volcano (Japan): a flow model for associated ash-cloud surges. *Journal of Volcanology and Geothermal Research*, 89(1), 159-172.
- Hall, M. L., Steele, A. L., Mothes, P. A., & Ruiz, M. C. (2013). Pyroclastic density currents (PDC) of the 16–17 August 2006 eruptions of Tungurahua volcano, Ecuador: Geophysical registry and characteristics. *Journal of Volcanology and Geothermal Research*, 265, 78-93.
- Hooper, P. R. (1997). The Columbia River flood basalt province: current status. *Geophysical Monograph Series*, 100, 1-27.
- Keszthelyi, L., McEwen, A. S., & Thordarson, T. (2000). Terrestrial analogs and thermal models for Martian flood lavas. *Journal of Geophysical Research: Planets (1991–2012)*, 105(E6), 15027-15049.
- King, S. D. (2005). Archean cratons and mantle dynamics. *Earth and Planetary Science Letters*, 234(1), 1-14.
- Lenardic, A., Moresi, L. N., & Mühlhaus, H. (2003). Longevity and stability of cratonic lithosphere: insights from numerical simulations of coupled mantle convection and continental tectonics. *Journal of Geophysical Research: Solid Earth (1978–2012)*, 108(B6).
- McClelland, E., Wilson, C. J., & Bardot, L. (2004). Palaeotemperature determinations for the 1.8-ka Taupo ignimbrite, New Zealand, and implications for the emplacement history of a high-velocity pyroclastic flow. *Bulletin of volcanology*, 66(6), 492-513.
- Németh, K., Suwesi, S. K., Peregi, Z., Gulácsi, Z., & Ujszászi, J. (2003). Plio/pleistocene flood basalt related scoria and spatter cones, rootless lava flows, and pit craters, Al Haruj Al Abiyad, Libya. *GeoLines*, 15, 98-103.
- O'Donnell, J. P., Adams, A., Nyblade, A. A., Mulibo, G. D., & Tugume, F. (2013). The uppermost mantle shear wave velocity structure of eastern Africa from Rayleigh wave tomography: constraints

- on rift evolution. *Geophysical Journal International*, 194(2), 961-978.
- Parshley, P. F., Kiessling, P. J., Antonius, J. A., Connell, R. S., Miller, S. H., & Green, F. H. (1982). Pyroclastic flow injury: Mount St. Helens, May 18, 1980. *The American Journal of Surgery*, 143(5), 565-568.
- Paterson, G. A., Roberts, A. P., Mac Niocaill, C., Muxworthy, A. R., Gurioli, L., Viramonté, J. G., ... & Weider, S. (2010). Paleomagnetic determination of emplacement temperatures of pyroclastic deposits: an under-utilized tool. *Bulletin of volcanology*, 72(3), 309-330.
- Perucca, L. P., & Moreiras, S. M. (2009). Seismic and volcanic hazards in Argentina. *Developments in Earth Surface Processes*, 13, 267-300.
- Power, J. A., Richter, D. H., & McGimsey, R. G. (1998). *Preliminary volcano-hazard assessment for Akutan Volcano east-central Aleutian Islands, Alaska*. Alaska Volcano Observatory.
- Reidel, S. P. (1998). Emplacement of Columbia River flood basalt. *Journal of Geophysical Research: Solid Earth (1978–2012)*, 103(B11), 27393-27410.
- Self, S., & Keszthelyi, L. Thordarson Th (1998) The importance of pahoehoe. *Ann. Rev. Earth Planet. Sci*, 26, 81-110.
- Self, S., Thordarson, T., & Keszthelyi, L. (1997). Emplacement of continental flood basalt lava flows. *Geophysical Monograph Series*, 100, 381-410.
- Sumner, J. M., Blake, S., Matela, R. J., & Wolff, J. A. (2005). Spatter. *Journal of Volcanology and Geothermal Research*, 142(1), 49-65.
- Tilling, R. I. (2009). Volcanism and associated hazards: the Andean perspective. *Advances in Geosciences*, 22.
- Wolf, T. (1878). *Memoria sobre el Cotopaxi y su última erupcion, acaecida el 26 de junio de 1877, por Teodoro Wolf: Con una lámina y una carta topográfica*. Imp. del comercio.

## Chapter 2. Characterization and petrological constraints of the mid-lithospheric discontinuity

Erika Rader<sup>1</sup>, Cheng Cheng<sup>2</sup>, Erica Emry<sup>3</sup>, Daniel Frost<sup>4</sup>, Julie Menard<sup>5</sup>, Nicholas Schmerr<sup>6</sup>, Chun-Quan Yu<sup>7</sup>, Dennis Geist<sup>1</sup>, Marc Hirschmann<sup>8</sup>, Cin-Ty Lee<sup>9</sup>

<sup>1</sup>\*Department of Geological Sciences, University of Idaho, 875 Perimeter Dr. Moscow ID, 83844

<sup>2</sup>Department of Earth and Planetary Science, Univ. of California Berkeley, 307 McCone Hall, Berkeley, CA 94720-4767

<sup>3</sup>Department of Geosciences, Penn State University, 503 Deike Building, University Park, PA 16802

<sup>4</sup>School of Earth and Environment, Univ. of Leeds, Maths/Earth and Environment Building  
Leeds. LS2 9JT, United Kingdom

<sup>5</sup>School of the Environment, Washington State University, PO Box 642812, Washington State University, Pullman WA 99164-2812

<sup>6</sup>Department of Geology, University of Maryland, College Park, MD, 20742-4211 USA

<sup>7</sup>Department of Earth, Atmospheric and Planetary Sciences, Massachusetts Institute of Technology, 77 Mass. Ave., Cambridge, MA 02139

<sup>8</sup>Department of Earth Sciences, University of Minnesota, 310 Pillsbury Drive SE, Minneapolis, MN 55455-0231

<sup>9</sup>Department of Earth Science, Rice University, 6100 Main Street, Houston, Texas 77005

\*Corresponding author email: rade5583@vandals.uidaho.edu

To be submitted to Earth and Planetary Science Letters

## 1. Abstract

Within the continental lithosphere, there is widespread seismic evidence for the presence of a discontinuity falling near 60-150 km depth. The so-called mid-lithospheric discontinuity (MLD) is detected by several seismic techniques, including shear wave anisotropy, P and S receiver functions, active-source seismic experiments, SS and PP precursors, and ScS reverberation phases. Here we compile observations of the MLD into a seismological database that includes the observed depths, velocity contrasts, gradients, and locales of MLD detections. Our analysis of this seismological database indicates that MLD observations are primarily found in regions of thick continental lithosphere and are manifested as abrupt decreases in seismic shear velocity (2-7% over 10-20 km) at 60-160 km depth, with the majority of global observations clustering around 80-90 km depth. We compare these seismological parameters to petrological and geochemical constraints provided by xenoliths that originated near the depth of the MLD. Xenolith populations from depths consistent with the MLD (2-5 GPa; 60-160 km) are compared to xenolith populations from regions and depths where the MLD has not been observed. We find that within the confines of the existing data on xenoliths, 25% of amphibole-bearing xenoliths, 90% of phlogopite-bearing xenoliths, and none of carbonate-bearing xenoliths were formed at 2-5 GPa. High Zr/Y and Ba/Nb of mantle xenoliths from the MLD are consistent with hydrous minerals in contrast to the low Zr/Y exhibited by carbonatite lavas. PERPLEX modeling of the elastic moduli and densities of carbonate, hydrous, and iron-rich minerals was used to evaluate the mode of candidate mineral phases required to achieve the velocity decrease seen at the MLD. The addition of 5-10% phlogopite, 10-15% carbonate, or 45-100% pyroxenite to mantle peridotite produces a shear velocity decrease of 2-7%. We thus propose the MLD may originate from a chemical interface related to the paleo-intersection of a volatile-rich solidus and progressively cooling thermal lithosphere. The presence of crystallized fluid-rich melt (amphibole or phlogopite-rich residues) implies the MLD may represent a remnant chemical tracer of the lithosphere-asthenosphere boundary (LAB) from when the lithosphere was young and thin.

## 2. Introduction

Seismological investigations of continental lithosphere are uncovering increasing evidence for the presence of a discontinuous seismic velocity reduction between 60 and 150 km (e.g., Fischer et al., 2010). These depths are within the tomographically defined cratonic lithosphere but are similar to the location of a velocity reduction associated with the lithosphere-asthenosphere boundary (LAB) near active margins. This velocity reduction has been named “the mid-lithospheric discontinuity” (MLD) (Fischer et al., 2010; Yuan & Romanowicz, 2010, Figure 1). Detections of the MLD span a wide suite of seismic methods, including long-range, active-source seismic refractions (Thybo & Perchuc, 1997), shear wave anisotropy (Yuan et al., 2011), P and S receiver functions (e.g., Abt et al., 2010; Ford et al., 2010; Geissler et al., 2010; Kumar et al., 2013; Savage & Silver, 2008; Wolbern et al., 2012), SS and PP precursors (Heit et al., 2010, Shearer, 1993, Zheng & Romanowicz, 2012), ScS core reflected phases (Courtier & Revenaugh, 2006), and surface wave tomography (Adams et al., 2012; Fishwick & Rawlinson, 2012; Heeszel et al., 2013; Jiang et al., 2012).

A variety of mechanisms has been proposed to explain the observed velocity reductions at the MLD, including: 1) the presence of modern carbonatite (Dasgupta & Hirschman, 2010); silicate (Dasgupta et al., 2013); or sulfuric (Helffrich et al., 2011) melts near the depth of the interface; 2) preserved ancient subduction zone fabrics that generate an anisotropic fabric during accretion (Yuan & Romanowicz, 2010); 3) an interface formed globally by the relaxation of the shear modulus due to frequency-dependent attenuation in the presence of hydrated phases (Karato 2012; Ologboji et al., 2013); or 4) an abrupt change in the chemical composition of the lithospheric mantle, caused by metasomatism or crystallized melts (Griffen et al., 2009; Savage & Silver 2008). The presence of melt typically requires high geothermal gradients and thus is less likely within ancient cratons that have very low geothermal gradients (e.g., Jaupart & Mareschal, 1999; Michaut et al., 2009). Another possibility is the presence of relatively exotic melt compositions, such as sulfuric melt, with a low solidus temperature (Helffrich et al., 2011). The preservation of anisotropy (lattice-preferred orientation) associated with paleosubduction has been proposed on the basis of xenolith textures. However, a preferred orientation and reduction of crystal size is found in xenoliths below the depths where the MLD is observed (Fischer et al., 2010). The presence of a global interface indicative of mantle hydration state has also been proposed, although it still remains unclear if whether the seismological evidence supports this model. Here, we use the mineralogy and geochemistry of xenoliths originating from the depth of

the MLD to evaluate these hypotheses, with particular focus on the feasibility of crystallized melt and its ability to concentrate certain elements and change the mode of the rock.

The hypothesis that we explore is that magma thermally equilibrates with surrounding rock and will crystallize where the geotherm crosses the solidus. A component of this hypothesis is that melts created by small extents of melting will be relatively rich in carbon and hydrogen compared to the dry surrounding peridotite. When this volatile-rich melt crystallizes, the resulting rocks bear hydrous or carbonate accessory minerals. Xenoliths have been reported to contain carbon in the form of diamond, graphite, calcium carbonate, dolomite, and aragonite (Ionov et al., 1993; Humphreys et al., 2010; Deines & Gold, 1973; Ionov et al., 1996; Lee et al., 2000). Carbonatite melts and associated silica-depleted igneous rocks are shown to have deep mantle sources (Jones et al., 2013; Dasgupta & Hirschmann, 2007; Bailey, 1990). Furthermore, the presence of carbon-rich fluid in the mantle has also been inferred from xenoliths containing Na-rich amphiboles (Yaxley et al., 1998), Na-rich glasses (Coltorti et al., 1998), and major and trace element signatures of partial melting at significant depths within the mantle (Lee & Wiley, 1997; Aulbach et al., 2013; Chakhmouradian et al., 2008). Hydrous minerals, such as amphiboles and micas, also occur in xenoliths from the continental lithosphere all over the globe (e.g., Yaxley et al., 1998; Lee & Wyllie, 1997; Lee et al., 2000).

Our approach is to investigate the presence, and type of, infiltrated melt in xenoliths via trace element analyses of xenoliths (e.g., McKenzie & O'Nions, 1991; Michard, 1989). Because the MLD occurs at a depth interval that is well represented in the xenolith database, chemical observations are a key tool for determining if the MLD has a compositional origin. Experiments have shown that carbon-rich fluids increase key trace elements like U, Th, and Sr relative to high-field strength elements (HFSE) such as Zr, Hf, and Ti (Green et al., 1992; Blundy & Dalton, 2000; Dasgupta et al., 2009). Increased U, Th, and Sr relative to Zr, Hf, and Ti in oceanic mantle xenoliths have been cited as evidence for interaction between peridotite and carbon-rich fluid at depths of 0.7-1.2 GPa (Delpech et al., 2004; Coltorti et al., 1999). In continental arc settings, many xenoliths possess carbonatite signatures at depths of 0.9-1.8 GPa (Ionov et al., 1993). Other mantle xenoliths from 1.5-2 GPa show trace element patterns indicative of cryptic carbonatite metasomatism (Yaxley et al., 1998). Negative Ti-Zr-Hf anomalies in mantle xenoliths were identified in the Slave craton and attributed to the presence of carbon-rich melt above 145 km (Aulbach et al., 2013). Thus it is clear that crystallized volatile-rich melts are preserved in the mid-continental lithosphere.

To investigate the expression of the MLD in continental mantle, we seek to clarify the uncertainty underlying the origin and evolution of the boundary by creating: 1) a seismological database that collects a wide variety of observations across seismic methods and quantifies the regions where the MLD has been observed as well as characteristics of the observations (i.e. depth, % velocity decrease, and boundary width); 2) a petrological database of xenoliths that originate within the depth range and vicinity of the observed seismological MLDs and; 3) thermodynamic modeling to assess the feasibility of crystallized melts producing the observed seismological constraints.

### 3. Methods

#### 3.1 The seismological database

We have constructed a database of seismological observations that detect a sharp seismic discontinuity in the mid-continental regions. We limited our search to observations within the depth range of 60-160 km, and to velocity decrease with depth to eliminate confusion with other seismic discontinuities, such as the Hales interface (positive velocity contrast at similar depth), the Gutenberg discontinuity (only observed in oceanic mantle), and the lithosphere-asthenosphere boundary (LAB). The MLD is thus defined in our study as occurring only beneath continental regions, though we acknowledge that the boundary shares many qualities of the Gutenberg discontinuity beneath the oceans, and may coincide with the LAB at continental margins. We only include observations of the MLD within cratonic lithosphere older than 1 Ga to avoid confusion with other seismically identified features.

Several different seismic phases were examined (Fig. 2): P to s receiver functions (Pds, conversion of an incoming P wave to a S wave), S to P receiver functions (Sdp, conversion of an incoming S wave to a P wave), SS and PP precursors (SdS, or PdP, underside reflections of S or P wave from a discontinuity at depth halfway between a station and source), ScS reverberations (reverberation of S wave energy that reflects from the core-mantle boundary prior to being reflected off of the MLD), decreases in shear velocity at mid-lithospheric depths from surface wave tomography that is sensitive to lithospheric and asthenospheric depths, and long-range, active-source seismic refraction experiments that identify scattering in the arrivals around distances of 8-14 degrees.

We compiled depth, location, and the approximate magnitude of the velocity decrease with depth across the discontinuity in different locations (Table 1). In some cases the extent of velocity decrease is not reported (N/A in Table 1). We also consider the resolutions of the different methods, both laterally and with depth. For example, S receiver functions average over a larger area than P

receiver functions. Alternatively, a MLD signal in the P receiver function, if not processed carefully, can be obscured by crustal reverberations (Rychert et al. 2010). In subsequent sections, we discuss pertinent details of each detection method and how they can affect observations interpreted as an MLD.

### 3.2 Geochemistry and petrology of xenoliths

The geochemical database PetDB (Lehnert et al., 2000) was systematically searched for compositional information on xenoliths originating beneath cratonic crust. To test our hypothesis regarding the presence of crystallized melts, search criteria selected xenoliths that hosted amphibole, phlogopite, carbonate minerals, graphite, or had published trace element (TE) concentrations. If estimated pressures are published, we use those values for determining the depth of melt formation. Some xenoliths were assigned the depth range based on the stability of spinel lherzolite of 0.9-1.8 Gpa (Demeny et al., 2004; Ionov et al., 1996; Delpuch et al., 2004). In the absence of pressure estimates, the two-pyroxene thermobarometers of Brey & Kohler (1990) were applied to analyses of orthopyroxene, clinopyroxene, and garnet to estimate the pressure of origin (Table 2). We also report on xenoliths from regions of the mantle where the MLD does not exist as a comparison and an additional test of our hypothesis. Trace-element analyses of carbonates and hydrous minerals were selected to represent a wide variety of compositions and include material irrespective of tectonic setting or depth.

Xenoliths from regions and depths consistent with the MLD observations are all peridotites while the control xenoliths are gabbro-norites, pyroxenites, norites, and granulites.

## 4. Seismological results

We compiled seismological results from six methodologies to illustrate the robustness of the MLD. This also allows further research to target regions with the highest resolution of the MLD and possibly use these observations to decipher the evolution of cratonic crust. All the results are summarized in Table 1.

### 4.1 Active source seismology

Active source seismic surveys provide a spatially high-resolution approach for studying lithospheric structures. A global compilation of high-density seismic refraction experiments that sample the continental lithosphere at long ranges (300 – 2500 km) reveals the existence of strong scattering beyond the 700-900-km offset, called the “8° Discontinuity” (Thybo & Perchuc, 1997). The 8° Discontinuity has been proposed to be a low-velocity zone (LVZ) below depths of 100 km (Thybo &

Perchuc, 1997; Chu et al., 2012), falling within our search criterion for the depth of the MLD. Thybo & Perchuc (1997) modeled these LVZ scatterers with fine-layered (40 km-thick) structures, which can extend to depths of about 180 km in “cold” regions and about 400 km in “hot” regions.

#### 4.2 Surface waves

Surface wave tomography probes the three-dimensional absolute shear wave velocity structure within the deep earth. Surface waves are dispersive, and the phase velocities of different frequency bands are sensitive to structures at different depths. Global surface-wave tomography studies reveal a low isotropic shear wave velocity zone (LVZ) beneath oceans, with a top that falls at greater depth with plate age (Nettles & Dziewonski, 2008; Maggi et al., 2006). This deepening of a low velocity zone indicates the melt boundary deepens with age. As a craton ages, this melt interface would migrate as well. Whereas the depth of a low-velocity layer beneath cratonic regions remains under debate, surface wave studies image an intra-lithospheric low-velocity layer at ~100 km depth beneath continental cratons (Cammarano & Romanowicz, 2007). The shear-wave velocity profile reveals that a transition from a fast seismic lid to a deeper slower zone coincides spatially with negative discontinuities found using receiver functions (Cammarano & Romanowicz, 2007). Various regional studies have identified a MLD, although the depth varies within different cratons. Also, vertical variations in velocity and azimuthal anisotropy from surface-wave tomography indicate seismic anisotropy might be another possible explanation for the middle lithosphere low velocity layer (Yuan & Romanowicz, 2010). Because surface waves are insensitive to sharp velocity jumps, it is desirable to compare surface-wave velocity models with those from other techniques.

#### 4.3 Receiver functions

Receiver functions (Pds and Sdp conversions) have been used to identify the relatively sharp changes in seismic velocity with depth associated with mantle discontinuities. They have relatively sharp spatial resolution, sampling deep structures within ~50 km laterally from the station for Pds and ~500 km for Sdp (Rychert et al., 2010; Kind et al., 2012). Earthquakes at epicentral distances of 30°-90° and 55°-85° are used for P and S receiver function analysis (e.g., Abt et al., 2010; Kind et al., 2012). Only Pds or Sdp phases are generally used to explore lithospheric structure, although SKSdp may also be useful (Kind et al., 2012). Studies that inspect multiple phases and dominant frequencies can help resolve the gradient across the discontinuity. P-receiver functions are able to detect fine structures of the

lithosphere due to their high frequency content, but Pds conversions from the MLD can be contaminated by crustal reverberations (Rychert et al., 2010). On the other hand, S-receiver functions are free from reverberations due to shallow structures, but their low frequency content limits the resolution of MLD. Changes in azimuthal anisotropy with depth can be obtained from receiver function studies for studies where incoming seismic energy comes in to a seismometer from all directions or backazimuths (Peng & Humphreys, 1997). Given the limited occurrence of usable earthquakes (i.e. distance, depth, magnitude), however, identification of changes in anisotropy with depth is not feasible in all regions.

Several Sdp and Pds studies have identified a sharp boundary from ~70 to 150 km deep at many locations (e.g., Fischer et al., 2010 and refs. therein; Rychert et al., 2010 and refs. therein; Kind et al., 2012 and refs. therein). The boundary has been called both the MLD or the LAB, making the distinction between the two ambiguous in some works. Furthermore, detailed characteristics of the boundary are not consistently reported, making comparison between different regions problematic. Nevertheless, many receiver function studies identify velocity decreases within the continental lithosphere of ~ 6% at 60-160 km depth (Table 1).

#### 4.4 Underside reflections

The underside reflection of shear and compressional wave energy from upper mantle seismic discontinuities produces precursory arrivals to the seismic phases SS and PP (and occasionally pP and sS depth phases from deep earthquakes). SS and PP precursors have been used extensively to map the lateral variations in the depth and sharpness of upper mantle discontinuity structure around the globe (e.g., Shearer, 1990; Gu & Dziewonski, 1998; Flanagan & Shearer, 1998). This technique has only recently been applied routinely to imaging structure in the 50-150 km depth range, although it is predominantly applied to oceanic regions (Rychert & Shearer, 2011; Schmerr, 2012). Nonetheless, sparse observations of the MLD with SS and PP precursors in continental settings exist (Heit et al., 2010), though a global survey has yet to be conducted using these seismic phases. Sampling points within a single survey are often clustered with depths of ~ 90 km, comparable to depths measured by the other seismic techniques. Precursors reflect from significantly greater depths under regions of active tectonics. Velocity deviations are rarely reported but are around -5% Vs (Heit et al., 2010).

#### 4.5 ScS reverberations

The ScS reverberation technique utilizes transversely polarized shear wave energy that reflects and reverberates from the core, crust, and seismic impedance contrasts in the upper and lower mantle. The multiple reverberations are typically used to produce a reflectivity profile of the mantle and, where above the background noise, are indicative of seismic discontinuities within the Earth (Revenaugh & Jordan, 1991). The observations are typically made in corridors that stretch between a source region of earthquakes and a series of seismic stations and utilize relatively long period (>30 second low-pass filtered) data. ScS reverberation investigations are predominantly beneath the oceanic regions, but a few studies of continental regions exist (e.g., Revenaugh & Sipkin, 1994; Courtier & Revenaugh, 2006). In addition to detecting positive velocity contrasts with depth, such as the Hales discontinuity (80-100 km) and the Lehmann discontinuity (200-250 km), some regions, such as China and the eastern United States, exhibit evidence for a sharp (10-20 km thick) velocity decrease with depth (5-12% decrease in shear velocity, assuming the reflectance is only due to velocity and not density) over a depth of 80-130 km.

#### 4.6 Summary of seismic results

Taken together, the seismic observations indicate the widespread occurrence of low velocity layers within the interior of thick continental lithosphere (Figure 3). There exists a strong regional bias in any analysis owing to the seismic data beneath the continental United States from the recent Earthscope Transportable Array. To account for this regional bias in our statistics, we consider regions that are most heavily studied by averaging the observations by area (Figure 4), which reveals that while MLDs have been detected at many locations and at many depths (from 60-160 km), the majority of detections occur  $\sim 90$  km deep. Regions with the most compelling indications for an MLD include the central United States, South Africa, and Australia, which are the best-studied locales.

### 5. Results for xenoliths

We find a total of 106 xenoliths in the global database PetDB (Table 2) that satisfy the criteria laid out in Section 2.2. Of this collection, 30 (28%) xenoliths contain carbonate or graphite and come from depths that range between 0.9 and 2 GPa. Forty-five (42%) xenoliths bear amphibole or phlogopite and come from depths of 0.2 to 6.5 GPa (Table 2, Fig 5). Phlogopite is far more common in xenoliths that

crystallize > 2 GPa. Thirty-two (30%) xenoliths have analyses for Ba, Nb, Y, and Zr concentrations, (Table 3).

Xenoliths from depths consistent with the MLD have Ba/Nb between 9.1 and 88.3 with a single outlier at 293.7 and Zr/Y of 2.9 to 21.7 (Fig. 6). Xenoliths from regions that lack a seismically detected MLD have Ba/Nb that ranges from 6.7 to 437 and Zr/Y of 0.3 to 8.3 (one outlier at 55.9) in 19 xenoliths. By comparison, carbonatite lava has Ba/Nb ranging from 2 to 1217 and rarely has Zr/Y > 10. Hydrous minerals also have large Ba/Nb of 1.5 to 1532 but have Zr/Y > 1 (Fig. 6). There is a distinct correlation between the location of hydrous-mineral bearing xenoliths and geographic regions with a seismic detection of the MLD (Figure 6).

## 6. Discussion

### 6.1 Seismic characteristics of the MLD

The MLD is best observed within ancient cratons. It has been observed using many methods including receiver functions on P and S waves, SS or PP precursors, surface waves, and active source (Table 1) and has been observed beneath cratons on almost every continent (Fig. 3). The depths tend to cluster around 80-90 km with a secondary peak at 120-130 km (Fig. 4). The depths at which shear velocity decreases occur can be as shallow as 47 km and as high as 400 km, although the latter value is likely a misidentification of the LAB. The measured seismic velocity decrease is 2-7% and is followed by an increase back to the regular gradient over a range of about 10 km. The region with the most observations is the North American craton, where in most localities the discontinuity is 80-115 km below the surface.

### 6.2 Shear wave velocity modeling

The elastic parameters of hydrous minerals have been compiled for subduction zones and other tectonic settings (e.g., Hacker et al., 2003). To model the relative shear velocity reduction associated with different mineral modes, we compare the contribution of individual minerals to a reference peridotite (4.75 km/s; Figure 7). Mineral velocities were obtained from the Hacker et al. (2003) at 1 GPa and 600°C. Using the seismic properties of hydrous and carbonate minerals, we calculate the mineral mode necessary to achieve the magnitude of shear velocity decrease characteristic of the MLD (Fig. 7). The decrease in velocity of 2-7% seen at the MLD can be achieved by adding 5-10% hydrous minerals or 10-25% carbonate minerals at 1 GPa. Mineralogical data suggest the presence of phlogopite in xenoliths

that equilibrated between 2 and 5 GPa (Fig. 5). Therefore, phlogopite is an attractive candidate for the origin of the 2-7% seismic velocity decrease at the MLD.

To account for a wider variety of lithologies than is represented by analyzed xenoliths, we use *Perple\_X* (Connolly, 2005) to model the density and seismic velocities of mantle carbonatites, eclogites, pyroxenites, Si-depleted melts, and both spinel-rich and garnet-rich peridotites (Fig. 8). *Perple\_X* uses a free-energy minimization algorithm developed by Ita & Stixrude (1992) to calculate stable assemblages over a range of pressures and temperatures for the system of Na<sub>2</sub>O, MgO, MnO, TiO<sub>2</sub>, Al<sub>2</sub>O<sub>3</sub>, SiO<sub>2</sub>, K<sub>2</sub>O, CaO, FeO, Cl<sub>2</sub>, Fe<sub>2</sub>O<sub>3</sub>, H<sub>2</sub>O, and CO<sub>2</sub>. We calculate phase diagrams for pressures from 1.5 to 8 GPa, and 500 to 1200°C. Density, P-wave, and S-wave velocities are then calculated as a Hill average of the Voigt-Reuss bounds on the elastic properties for different proportions of the constituent minerals to obtain a bulk rock velocity. Combinations of pressures and temperatures that result in melt were excluded as we are seeking the elastic parameters of solid lithologies, which is suggested by the low geothermal gradient in these cratonic environments.

At 1.5 GPa and 600°C, lithologies with 10-30% carbonatite, 40-100% cpx-pyroxenite or Si-depleted melt, or 55-100% carbonated eclogite reproduce the observed shear velocity reductions at the MLD (Figure 8). Carbonatitic compositions are 2-3% less dense than surrounding peridotites, and thus dynamically unstable. Si-depleted rocks, opx-pyroxenites and carbonated eclogite are denser (2-5%) than the surrounding peridotite, also introducing a dynamically unstable layer of material into the continental lithosphere. Of the lithologies we investigated, only cpx-pyroxenite appears to have the necessary properties to both reproduce the observed velocity contrast and remain dynamically stable over the timescales of continental lithosphere evolution.

### 6.3 A stalled melt layer

In mantle peridotite, the fluid-saturated solidus has a distinct near-horizontal segment at ~950-1200°C and ~2 GPa (Faloon & Green, 1989). Melt that is generated deeper and is in thermal equilibrium with surrounding peridotite can be trapped by the gently sloping part of the solidus over a broad range of geothermal gradients as crust cools (Fig. 9). The pressure at which ageing geothermal gradients intersect the volatile-rich solidus is equivalent to a depth of ~100 km and corresponds well to the observed depth of the MLD. As the lithospheric mantle cools over time, a permeability cap develops, as will a subsequent compaction layer that will sharpen the associated seismic discontinuity (Revenaugh & Meyer, 1997).

Xenoliths from regions where the MLD is present are chemically distinct from xenoliths originating from regions where no MLD has been detected (Fig. 6). Xenoliths from the MLD have higher Ba/Nb and Zr/Y than either primitive mantle or other mantle xenoliths from similar depths (Table 3). Individual analyses of hydrous minerals reveal high Ba/Nb and Zr/Y, which, when mixed with primitive mantle, have the compositional diversity observed in the MLD xenoliths. Carbonatite lavas have much lower Zr/Y than MLD xenoliths, indicating that the presence of hydrous minerals, not carbonates, raises the Ba/Nb and Zr/Y of these xenoliths.

#### 6.4 Relationship to the LAB

Low-velocity zones beneath thin oceanic lithosphere have been attributed to the physical boundary between the lithosphere and the asthenosphere. The LAB has been proposed to be a zone of ponded melt (Sakamaki et al., 2013). Our model is similar in that it calls on trapped melt within cratonic lithosphere at the same depth that the LAB has been observed near active margins. The difference is that at the MLD, the trapped melt crystallizes as a craton cools. The MLD, therefore, is a chemical boundary that develops as the LAB deepens and separates the active ponded melt from the crystallized layer that contains hydrous minerals (Fig. 9). This hypothesis is supported by the presence of carbonate-rich metasomatism (short of carbonatite melts) occurring at depths associated with the LAB at active margins (Delpech et al., 2004; Coltorti et al., 1999; Ionov et al., 1993; Yaxley et al., 1998) and occurring at depths associated with the MLD at inactive craton interiors.

#### 7. Conclusions

The seismic velocity decrease observed between 65 and 150 km beneath cratons older than 1 Ga can be attributed to a chemical boundary within the mantle. Phlogopite is found in xenoliths from these depths and regions, which yields high Ba/Nb and Zr/Y in these rocks. The addition of 5-15% phlogopite reduces the shear velocity of a peridotite to that observed at the MLD. This has led us to propose a mechanism that forms a chemically distinct layer ~65 km beneath the crust as it ages by crystallizing small pockets of volatile-rich melt that thermally equilibrate with the surrounding mantle as it ascends. The MLD is distinguishable from the LAB by remaining at a constant depth at the time of formation, whereas the LAB continues to deepen with time. With further study, the MLD could provide information about the evolution of cratons and cratonic lithosphere, and link seismic velocity to mineralogy within the mantle.

## 8. Acknowledgements

This manuscript originated from a small discussion group at the 2013 CIDER workshop at the University of California at Berkeley. We thank the following for organizing and contributing to our discussions at the workshop: B. Romanowicz, R. Dasgupta, C. Lee, D. Schutt, K. Rychert, N. Harmon, M. Hirschmann, C. Jaupart, I. Artemieva, R. Carlson, B., Stern, and L. Wagner. CIDER and the authors were supported by the National Science Foundation. GMT software (Wessel and Smith, 1998) was used for preparation of the figures.

## References

- Abt, D. L., Fischer, K. M., French, S. W., Ford, H. A., Yuan, H., & Romanowicz, B. (2010). North American lithospheric discontinuity structure imaged by Ps and Sp receiver functions. *Journal of Geophysical Research: Solid Earth (1978–2012)*, *115*(B9).
- Adams, A., Nyblade, A., & Weeraratne, D. (2012). Upper mantle shear wave velocity structure beneath the East African plateau: evidence for a deep, plateau-wide low velocity anomaly. *Geophysical Journal International*, *189*(1), 123-142.
- Aulbach, S., Griffin, W. L., Pearson, N. J., & O'Reilly, S. Y. (2013). Nature and timing of metasomatism in the stratified mantle lithosphere beneath the central Slave craton (Canada). *Chemical Geology*, *352*, 153-169.
- Bailey, D. K. (1990). Mantle carbonatite eruptions: crustal context and implications. *Lithos*, *26*(1), 37-42.
- Blundy, J., & Dalton, J. (2000). Experimental comparison of trace element partitioning between clinopyroxene and melt in carbonate and silicate systems, and implications for mantle metasomatism. *Contributions to Mineralogy and Petrology*, *139*(3), 356-371.
- Brey, G. P., & Köhler, T. (1990). Geothermobarometry in four-phase lherzolites II. New thermobarometers, and practical assessment of existing thermobarometers. *Journal of Petrology*, *31*(6), 1353-1378.
- Cammarano, F., & Romanowicz, B. (2007). Insights into the nature of the transition zone from physically constrained inversion of long-period seismic data. *Proceedings of the National Academy of Sciences*, *104*(22), 9139-9144.
- Chakhmouradian, A. R., Mumin, A. H., Demény, A., & Elliott, B. (2008). Postorogenic carbonatites at Eden Lake, Trans-Hudson Orogen (northern Manitoba, Canada): geological setting, mineralogy and geochemistry. *Lithos*, *103*(3), 503-526.
- Chu, R., Schmandt, B., & Helmberger, D. V. (2012). Upper mantle P velocity structure beneath the Midwestern United States derived from triplicated waveforms. *Geochemistry, Geophysics, Geosystems*, *13*(2).
- Coltorti, M., Bonadiman, C., Hinton, R. W., Siena, F., & Upton, B. G. J. (1999). Carbonatite metasomatism of the oceanic upper mantle: evidence from clinopyroxenes and glasses in ultramafic xenoliths of Grande Comore, Indian Ocean. *Journal of Petrology*, *40*(1), 133-165.
- Connolly, J.A.D. (2005) Computation of phase equilibria by linear programming: a tool for

- geodynamic modeling and its application to subduction zone decarbonation. *Earth and Planetary Science Letters*, 236, 524-541.
- Courtier, A. M., & Revenaugh, J. (2006). A water-rich transition zone beneath the eastern United States and Gulf of Mexico from multiple ScS reverberations. *Geophysical Monograph Series*, 168, 181-193.
- Dasgupta, R., & Hirschmann, M. M. (2007). A modified iterative sandwich method for determination of near-solidus partial melt compositions. II. Application to determination of near-solidus melt compositions of carbonated peridotite. *Contributions to Mineralogy and Petrology*, 154(6), 647-661.
- Dasgupta, R., Hirschmann, M. M., McDonough, W. F., Spiegelman, M., & Withers, A. C. (2009). Trace element partitioning between garnet lherzolite and carbonatite at 6.6 and 8.6 GPa with applications to the geochemistry of the mantle and of mantle-derived melts. *Chemical Geology*, 262(1), 57-77.
- Dasgupta, R., & Hirschmann, M. M. (2010). The deep carbon cycle and melting in Earth's interior. *Earth and Planetary Science Letters*, 298(1), 1-13.
- Dasgupta, R., Mallik, A., Tsuno, K., Withers, A. C., Hirth, G., & Hirschmann, M. M. (2013). Carbon-dioxide-rich silicate melt in the Earth's upper mantle. *Nature*, 493(7431), 211-215.
- Deines, P., & Gold, D. P. (1973). The isotopic composition of carbonatite and kimberlite carbonates and their bearing on the isotopic composition of deep-seated carbon. *Geochimica et Cosmochimica Acta*, 37(7), 1709-1733.
- Delpech, G., Grégoire, M., O'Reilly, S. Y., Cottin, J. Y., Moine, B., Michon, G., & Giret, A. (2004). Feldspar from carbonate-rich silicate metasomatism in the shallow oceanic mantle under Kerguelen Islands (South Indian Ocean). *Lithos*, 75(1), 209-237.
- Demény, A., Vennemann, T. W., Hegner, E., Nagy, G., Milton, J. A., Embey-Isztin, A., ... & Dobosi, G. (2004). Trace element and C–O–Sr–Nd isotope evidence for subduction-related carbonate–silicate melts in mantle xenoliths (Pannonian Basin, Hungary). *Lithos*, 75(1), 89-113. <http://dx.doi.org/10.1016/j.lithos.2003.12.016>.
- Duke, G. I. (2009). Black Hills–Alberta carbonatite–kimberlite linear trend: Slab edge at depth?. *Tectonophysics*, 464(1), 186-194.
- Falloon, T. J., & Green, D. H. (1989). The solidus of carbonated, fertile peridotite. *Earth and Planetary Science Letters* 94(3), 364-370.

- Flanagan, M. P., & Shearer, P. M. (1998). Global mapping of topography on transition zone velocity discontinuities by stacking SS precursors. *Journal of Geophysical Research: Solid Earth (1978–2012)*, *103*(B2), 2673-2692.
- Fischer, K. M., Ford, H. A., Abt, D. L., & Rychert, C. A. (2010). The lithosphere-asthenosphere boundary. *Annual Review of Earth and Planetary Sciences*, *38*, 551-575. doi: 10.1146/annurev-earth-040809-152438.
- Fishwick, S., & Rawlinson, N. (2012). 3-D structure of the Australian lithosphere from evolving seismic datasets. *Australian Journal of Earth Sciences*, *59*(6), 809-826.
- Ford, H. A., Fischer, K. M., Abt, D. L., Rychert, C. A., & Elkins-Tanton, L. T. (2010). The lithosphere–asthenosphere boundary and cratonic lithospheric layering beneath Australia from Sp wave imaging. *Earth and Planetary Science Letters*, *300*(3), 299-310.
- Geissler, W. H., Sodoudi, F., & Kind, R. (2010). Thickness of the central and eastern European lithosphere as seen by S receiver functions. *Geophysical Journal International*, *181*(2), 604-634.
- Green, T. H., Adam, J., & Siel, S. H. (1992). Trace element partitioning between silicate minerals and carbonatite at 25 kbar and application to mantle metasomatism. *Mineralogy and Petrology*, *46*(3), 179-184.
- Griffin, W.L., S.Y. O'Reilly, J.C. Afonso, and G.C. Begg, 2009, The composition and evolution of lithospheric mantle: a re-evaluation and its tectonic implications, *Journal of Petrology*, *50*(7), 1185-1204.
- Gu, Y., Dziewonski, A. M., & Agee, C. B. (1998). Global de-correlation of the topography of transition zone discontinuities. *Earth and Planetary Science Letters*, *157*(1), 57-67.
- Hacker, B. R., Abers, G. A., & Peacock, S. M. (2003). Subduction factory 1. Theoretical mineralogy, densities, seismic wave speeds, and H<sub>2</sub>O contents. *Journal of Geophysical Research: Solid Earth (1978–2012)*, *108*(B1).
- Heeszel, D. S., Wiens, D. A., Nyblade, A. A., Hansen, S. E., Kanao, M., An, M., & Zhao, Y. (2013). Rayleigh wave constraints on the structure and tectonic history of the Gamburtsev Subglacial Mountains, East Antarctica. *Journal of Geophysical Research: Solid Earth*, *118*(5), 2138-2153.
- Heit, B., Yuan, X., Bianchi, M., Kind, R., & Gossler, J. (2010). Study of the lithospheric and upper-mantle discontinuities beneath eastern Asia by SS precursors. *Geophysical Journal International*, *183*(1), 252-266.

- Helfrich, G., Kendall, J. M., Hammond, J. O. S., & Carroll, M. R. (2011). Sulfide melts and long-term low seismic wavespeeds in lithospheric and asthenospheric mantle. *Geophysical Research Letters*, *38*(11).
- Humphreys, E. R., Bailey, K., Hawkesworth, C. J., Wall, F., Najorka, J., & Rankin, A. H. (2010). Aragonite in olivine from Calatrava, Spain—Evidence for mantle carbonatite melts from > 100 km depth. *Geology*, *38*(10), 911-914.
- Ionov, D. A., Dupuy, C., O'Reilly, S. Y., Kopylova, M. G., & Genshaft, Y. S. (1993). Carbonated peridotite xenoliths from Spitsbergen: implications for trace element signature of mantle carbonate metasomatism. *Earth and Planetary Science Letters*, *119*(3), 283-297.
- Ionov, D. A., O'Reilly, S. Y., Genshaft, Y. S., & Kopylova, M. G. (1996). Carbonate-bearing mantle peridotite xenoliths from Spitsbergen: phase relationships, mineral compositions and trace-element residence. *Contributions to Mineralogy and Petrology*, *125*(4), 375-392.
- Ita, J., & Stixrude, L. (1992). Petrology, elasticity, and composition of the mantle transition zone. *Journal of Geophysical Research: Solid Earth (1978–2012)*, *97*(B5), 6849-6866.
- Jaupart, C. and J.C. Mareschal, 1999, The thermal structure and thickness of continental roots, *Lithos*, *48*, 93-114.
- Jiang, M., Ai, Y., Chen, L., & Yang, Y. (2013). Local modification of the lithosphere beneath the central and western North China Craton: 3-D constraints from Rayleigh wave tomography. *Gondwana Research*, *24*(3), 849-864.
- Jones, A. P., Genge, M., & Carmody, L. (2013). Carbonate melts and carbonatites. *Rev Mineral Geochem*, *75*, 289-322.
- Karato, S., 2012, On the origin of the asthenosphere, *Earth and Planetary Science Letters*, *321-322*, 95-103.
- Kind, R., Yuan, X., & Kumar, P. (2012). Seismic receiver functions and the lithosphere–asthenosphere boundary. *Tectonophysics*, *536*, 25-43. doi: 10.1016/j.tecto.2012.03.005.
- Kumar, P., X. Yuan, R. Kind, and J. Mechie, 2012, The lithosphere-asthenosphere boundary observed with USArray receiver functions, *Solid Earth*, *3*, 149-159.
- Kumar, P., Ravi Kumar, M., Sriyayanthi, G., Arora, K., Srinagesh, D., Chadha, R. K., & Sen, M. K. (2013). Imaging the lithosphere-asthenosphere boundary of the Indian plate using converted wave techniques. *Journal of Geophysical Research: Solid Earth*, *118*(10), 5307-5319.

- Lee, C. T., Rudnick, R. L., McDonough, W. F., & Horn, I. (2000). Petrologic and geochemical investigation of carbonates in peridotite xenoliths from northeastern Tanzania. *Contributions to Mineralogy and Petrology*, 139(4), 470-484.
- Lee, W. J., & Wyllie, P. J. (1997). Liquid immiscibility between nephelinite and carbonatite from 1.0 to 2.5 GPa compared with mantle melt compositions. *Contributions to Mineralogy and Petrology*, 127(1-2), 1-16.
- Lehnert, K., Su, Y., Langmuir, C. H., Sarbas, B., & Nohl, U. (2000). A global geochemical database structure for rocks. *Geochemistry, Geophysics, Geosystems*, 1(5).  
[doi:10.1029/1999GC000026](https://doi.org/10.1029/1999GC000026).
- Maggi, A., Debayle, E., Priestley, K., & Barruol, G. (2006). Multimode surface waveform tomography of the Pacific Ocean: a closer look at the lithospheric cooling signature. *Geophysical Journal International*, 166(3), 1384-1397.
- McKenzie, D. A. N., & O'Nions, R. K. (1991). Partial melt distributions from inversion of rare earth element concentrations. *Journal of Petrology*, 32(5), 1021-1091.
- Michard, A. (1989). Rare earth element systematics in hydrothermal fluids. *Geochimica et Cosmochimica Acta*, 53(3), 745-750.
- Michaut, C., Jaupart, C., & Mareschal, J. C. (2009). Thermal evolution of cratonic roots. *Lithos*, 109(1), 47-60.
- Nettles, M., & Dziewoński, A. M. (2008). Radially anisotropic shear velocity structure of the upper mantle globally and beneath North America. *Journal of Geophysical Research: Solid Earth (1978–2012)*, 113(B2).
- Olugboji, T. M., Karato, S. I., & Park, J. (2013). Structures of the oceanic lithosphere-asthenosphere boundary: Mineral-physics modeling and seismological signatures. *Geochemistry, Geophysics, Geosystems*, 14(4), 880-901.
- Peng, X., & Humphreys, E. D. (1997). Moho dip and crustal anisotropy in northwestern Nevada from teleseismic receiver functions. *Bulletin of the Seismological Society of America*, 87(3), 745-754.
- Revenaugh, J., & Jordan, T. H. (1991). Mantle layering from ScS reverberations: 1. Waveform inversion of zeroth-order reverberations. *Journal of Geophysical Research: Solid Earth (1978–2012)*, 96(B12), 19749-19762.
- Revenaugh, J., & Meyer, R. (1997). Seismic evidence of partial melt within a possibly ubiquitous low-velocity layer at the base of the mantle. *Science*, 277(5326), 670-673.

- Revenaugh, J., & Sipkin, S. A. (1994). Mantle discontinuity structure beneath China. *Journal of Geophysical Research: Solid Earth (1978–2012)*, 99(B11), 21911-21927.
- Rychert, C. A., Shearer, P. M., & Fischer, K. M. (2010). Scattered wave imaging of the lithosphere–asthenosphere boundary. *Lithos*, 120(1), 173-185.  
doi: 10.1016/j.lithos.2009.12.006.
- Rychert, C. A., & Shearer, P. M. (2011). Imaging the lithosphere–asthenosphere boundary beneath the Pacific using SS waveform modeling. *Journal of Geophysical Research: Solid Earth (1978–2012)*, 116(B7).
- Sakamaki, T., Suzuki, A., Ohtani, E., Terasaki, H., Urakawa, S., Katayama, Y., ... & Ballmer, M. D. (2013). Ponded melt at the boundary between the lithosphere and asthenosphere. *Nature Geoscience*.
- Savage, B., & Silver, P. G. (2008). Evidence for a compositional boundary within the lithospheric mantle beneath the Kalahari craton from S receiver functions. *Earth and Planetary Science Letters*, 272(3), 600-609.
- Schmerr, N. (2012). The Gutenberg Discontinuity: Melt at the Lithosphere-Asthenosphere Boundary. *Science*, 335, 1480–1483.
- Shearer, P. M. (1990). Seismic imaging of upper-mantle structure with new evidence. *Nature*, 344, 8.
- Shearer, P. M. (1993). Global mapping of upper mantle reflectors from long-period SS precursors. *Geophysical Journal International*, 115(3), 878-904.
- Sleep, N. H. (2005). Evolution of the continental lithosphere. *Annu. Rev. Earth Planet. Sci.*, 33, 369-393.
- Thybo, H. & Perchuc, E. (1997). The seismic 8° discontinuity and partial melting in continental mantle, *Science*, 275, 1626-1629. doi: 10.1126/science.275.5306.1626.
- Wittlinger, G., & Farra, V. (2007). Converted waves reveal a thick and layered tectosphere beneath the Kalahari super-craton. *Earth and Planetary Science Letters*, 254(3), 404-415.
- Wölbern, I., Rümpler, G., Link, K., & Sodoudi, F. (2012). Melt infiltration of the lower lithosphere beneath the Tanzania craton and the Albertine rift inferred from S receiver functions. *Geochemistry, Geophysics, Geosystems*, 13(8).
- Yaxley, G. M., Green, D. H., & Kamenetsky, V. (1998). Carbonatite metasomatism in the southeastern Australian lithosphere. *Journal of Petrology*, 39(11-12), 1917-1930.

Yuan, H. & Romanowicz, B. (2010), Lithospheric layering in the North American craton, *Nature*, *466*, 1063-1069. doi: 10.1038/nature09332.

Yuan, H., Romanowicz, B., Fischer, K. M., & Abt, D. (2011). 3-D shear wave radially and azimuthally anisotropic velocity model of the North American upper mantle. *Geophysical Journal International*, *184*(3), 1237-1260.

Zheng, Z., & Romanowicz, B. (2012). Do double 'SS precursors' mean double discontinuities?. *Geophysical Journal International*, *191*(3), 1361-1373.



	Profile2e	[45 46]	[-118 -91]		~100		Visual
	Profile2f	[35 38 46]	[-116 -103 -90]		~100		Visual
	Profile2g	[32 46]	[-100 -90]		~100		Visual
	Profile2h	[33 45]	[-92 -89]		~100		Visual
	Profile3	[50 38]	[-120 -120]		~100		Visual
	Profile4	[27 15]	[-110 -85]		~100		Visual
	Profile5	[36 30]	[-118 -116]		~100		Visual
	Profile6	[51 29]	[-124 -115]		~100		Visual
	Profile7	[59 32]	[-110 -109]		~100		Visual
Europe/Asia							
Geissler, et al, 2010	S-RF	49.631	22.708	Poland; KWP	129	-5	Exact
		54.958	37.767	Russia; MHV	102	-5	Exact
		55.685	12.433	Denmark; COP	125	-5	Exact
		59.649	9.598	Norway; KONO	116	-5	Exact
Saul, J. et al, 2000	P-RF	17.417	78.55	Indian Shield; HYB	90	n/a	Exact
Kumar, et al., 2007	S-RF	17.42	78.55	India; HYB	101	n/a	Exact
		23.52	45.5	Saudi Arabia; RAYN	138	n/a	Exact
Sodoudi, et al, 2006	S-RF	29 to 32	114.5 to 117	China; Yangtze Craton	72	n/a	Visual
		32 to 34.5	114.5 to 117	China; North China Platform	60	n/a	Visual
Kumar, et al, 2005	S-RF	45	77	Tianshan, China	120	n/a	Kind, et al, 2012
		44	77	Tianshan, China	100	n/a	Kind, et al, 2012
		43	77	Tianshan, China	120	n/a	Kind, et al, 2012
		33	77	Karakoram, China	120	n/a	Kind, et al, 2012
Revenaugh and Simpkin, 1995	ScS Reverb.	31.819	86.509	China	158	-8.6	
		37.148	87.1198	China	145	-6.2	
		40.506	78.8797	China	131	-9.2	
		46.952	114.12911	China	133	-2.4	
		46.424	131.372	China	84	-4.2	
		49.915	133.35605	China	80	-5.6	
		39.563	115.045	China	79	-6	
		35.66	127.099	China	64	-12	
		42.026	130.849	China	72	-7.6	
		36.537	122.618	China	123	-4.2	
		40.636	121.856	China	103	-7.8	
46.125	127.191	China	147	-4.4			
Heit, et al, 2010	SS precursor			Tibet/China			
Tonegawa and Hellfrich, 2012	sS precursors			Phillipine Sea Plate	59.3	-5.8	
				N Korea (weak MLD)	90	-11.4	
Zhang and Lay, 2003				Sea of Okhotsk (weak MLD)		-11.4	
				Izu Japan	66	-12.6	
Thybo et al, 2006	Refraction Profile8a	[71 61]	[26 19]		~100		Visual

Profile8b	[59 52]	[17 13]	~100	Visual				
Profile9	[65 53]	[23 18]	~100	Visual				
Profile10	[47 42]	[-8 8]	~100	Visual				
Profile11a	[49 35]	[-1 22]	~100	Visual				
Profile11b	[50 38]	[3 25]	~100	Visual				
Profile12a	[29 51]	[-1 17]	~100	Visual				
Profile12b	[34 52]	[-8 14]	~100	Visual				
Profile13a	[55 57 43]	[-1 32 73]	~100	Visual				
Profile13b	[50 68 74]	[-7 22 56]	~100	Visual				
Profile14	[70 64 49]	[42 71 95]	~100	Visual				
Profile15	[57 65 56]	[62 104 138]	~100	Visual				
Profile16	[65 73 65]	[61 104 143]	~100	Visual				
Profile17	[75 63 50]	[82 93 101]	~100	Visual				
Profile18	[76 53]	[95 116]	~100	Visual				
<hr/>								
South America								
<hr/>								
Heit et al., 2007	S-RF; SKS-RF	5.11	-52.64	French Guyana; MPG	70	n/a	Exact	
		-5.82	-35.9	NE Brazil; RCBR	80	n/a	Exact	
		-26.33	-57.33	Paraguay; CPUP	80	n/a	Exact	
		-8.94	-63.18	Amazonas; SAML	130	n/a	Exact	
		-15 to -	-49 to -					
		15.64	48.01	Central Brazil	140	n/a	Exact	
		-22	-52	Parana Basin	120	n/a	Exact	
		-23 to -	-45 to -					
		23.52	47.43	Brazilian Coast	80	n/a	Exact	
		-38.05	-61.97	Central Argentina; TRQA	120	n/a	Exact	
<hr/>								
Africa								
<hr/>								
Savage, B. and P. Silver, 2008	S-RF; P-RF	-19 to -30	23 to 31	South Africa	150	-4.5	Visual	
		Hansen, et al, 2009	S-RF	-26 to -31	21 to 32	South Africa	160	-4.5
Wittlinger and Farra, 2007	S-RF; SKS-RF; P-RF	-19 to -33	22 tp 30	South Africa	70-151	-5	Visual	
		Kumar, et al., 2007	S-RF	-19.2	17.58	Namibia; TSUM	127	n/a
-32.38	20.81		South Africa; SUR	134	n/a	Exact		
-28.61	25.26		South Africa; BOSA	150	n/a	Visual		
-15.28	28.19		Zambia; LSZ	150	n/a	Visual		
-25.02	25.6	Botswana; LBTB	150	n/a	Visual			
<hr/>								
Australia								
<hr/>								
Ford, et al, 2010	S-RF; P-RF	-18.1	125.64	FITZ	81	n/a	Exact	
		-30.78	128.06	FORT	79	n/a	Exact	
		-31.37	121.88	KMBL	85	n/a	Exact	
		-19.93	134.36	WRAB	81	n/a	Exact	
		-21.16	119.73	MBWA	69	n/a	Exact	
		-32.93	117.24	NWAO	81	n/a	Exact	
Thybo et al, 2006	Refraction Profile19a Profile19b							
		[-9 -22]	[113 135]		~100		Visual	
		[2 -21]	[129 138]		~100		Visual	
<hr/>								
Antarctica								
<hr/>								
Heeszel, et al, 2013	Surface Wave	-85 to -78	60 to 100	Gamburtsev Mtns	75	-2	Visual	

Table 2. Depths of xenoliths.

<sup>1</sup>Depth reported in PetDB, <sup>2</sup>Depth calculated from Brey and Kohler 1990, <sup>3</sup>Depth limited by spinel

Sample name	Source	Latitude	Longitude	Minerals	Depth (Gpa)	Temperature (°C)	Geologic Setting	Xenolith Type
MUKHSIE-BC-F-68 <sup>2</sup>	MUKHOPADHYAY, 1994	37.21	-119.26	Amph, Phlog	1.1	674	Convergent Margin	Pyroxenite
LOGERM-EE-S1 <sup>2</sup>	LOOCK, 1990	50.17	6.85	Amph	0.2	721	Intraplate, Off-Craton	Granulite
LOGERM-WE-S35 <sup>2</sup>	LOOCK, 1990	50.17	6.85	Amph	0.2	655	Intraplate, Off-Craton	Granulite
LOGERM-EE-S12	LOOCK, 1990	50.17	6.85	Amph	0.8	737	Intraplate, Off-Craton	Granulite
FRANAK-NUN-13004 <sup>2</sup>	FRANCIS, 1976	60	-166.5	Amph	0.9	964	Intraplate, Off-Craton	Pyroxenite
ARCAUST-LB-83-2 <sup>2</sup>	ARCULUS, 1988	-38.2	143.1	Amph	0.9	881	Intraplate, Off-Craton	Pyroxenite
LOGERM-WE-S16 <sup>2</sup>	LOOCK, 1990	50.17	6.85	Amph	1.0	864	Intraplate, Off-Craton	Granulite
LOGERM-WE-S37 <sup>2</sup>	LOOCK, 1990	50.17	6.85	Amph	1.1	853	Intraplate, Off-Craton	Granulite
LOGERM-EE-S1 <sup>2</sup>	LOOCK, 1990	50.17	6.85	Amph	1.2	816	Intraplate, Off-Craton	Granulite
MUKHSIE-PSM-PS20 <sup>2</sup>	MUKHOPADHYAY, 1994	37.21	-119.26	Amph	1.5	780	Convergent Margin	Pyroxenite
KEMRUSS-KOLA-436-17 <sup>2</sup>	KEMPTON, 1995	67	32.5	Amph	1.6	738	Intraplate, Craton	Granulite
LOGERM-WE-S35 <sup>2</sup>	LOOCK, 1990	50.17	6.85	Amph	1.6	791	Intraplate, Off-Craton	Granulite
LOGERM-WE-S37 <sup>2</sup>	LOOCK, 1990	50.17	6.85	Amph	1.6	883	Intraplate, Off-Craton	Granulite
LOGERM-WE-S16 <sup>2</sup>	LOOCK, 1990	50.17	6.85	Amph	1.6	902	Intraplate, Off-Craton	Granulite
FRANAK-NUN-14001 <sup>2</sup>	FRANCIS, 1976	60	-166.5	Amph	1.8	1080	Intraplate, Off-Craton	Pyroxenite
LITRUSS-VIT-V462 <sup>2</sup>	LITASOV, 2000	53.5	113.1	Amph	2.2	1112	Continental Rift	Peridotite
JANSLOV-POH-119-5 <sup>2</sup>	JANAK, 2006	46.4	15.5	Amph	2.5	918	Intraplate, Off-Craton	Peridotite
IONRUSS-VIT-313-103 <sup>2</sup>	IONOV, 1993	59.45	112.55	Amph	2.6	1105	Continental Rift	Peridotite
JANSLOV-POH-119-5 <sup>2</sup>	JANAK, 2006	46.4	15.5	Amph	2.9	770	Intraplate, Off-Craton	Peridotite
JANSLOV-POH-VI01/04 <sup>2</sup>	JANAK, 2006	46.4	15.5	Amph	3.5	1128	Intraplate, Off-Craton	Peridotite
MUKHSIE-PSM-PS20 <sup>2</sup>	MUKHOPADHYAY, 1994	37.25	-119.33	Amph	6.0	1209	Convergent Margin	Pyroxenite
MUKHSIE-BC-F-51 <sup>2</sup>	DANCHIN, 1979	-25.6593	28.5078	Phlog	1.1	681	Intraplate, Craton	Peridotite
LITRUSS-VIT-V439 <sup>2</sup>	DANCHIN, 1979	-25.6593	28.5078	Phlog	2.0	1097	Intraplate, Craton	Peridotite
GLASRUS-VIT-SG96B13 <sup>2</sup>	DANCHIN, 1979	-25.6593	28.5078	Phlog	2.0	1072	Intraplate, Craton	Peridotite
IONRUSS-VIT-313-110 <sup>2</sup>	EHRENBERG, 1982	36.6	-109.05	Phlog	2.1	1075	Intraplate, Off-Craton	Peridotite
LITRUSS-VIT-V857 <sup>2</sup>	EHRENBERG, 1982	36.6	-109.05	Phlog	2.3	1109	Intraplate, Off-Craton	Pyroxenite
IONRUSS-VIT-314-74 <sup>2</sup>	EHRENBERG, 1982	36.6	-109.05	Phlog	2.3	1203	Intraplate, Off-Craton	Peridotite
IONRUSS-VIT-313-7 <sup>2</sup>	EHRENBERG, 1982	36.6	-109.05	Phlog	2.4	1157	Intraplate, Off-Craton	Peridotite
LITRUSS-VIT-V462 <sup>2</sup>	GLASER, 1999	59.5	112.5	Phlog	2.5	1161	Continental Rift	Peridotite
LITRUSS-VIT-V202 <sup>2</sup>	IONOV, 1993	59.45	112.55	Phlog	2.9	1265	Continental Rift	Peridotite
REHFSAF-DJ0218 <sup>2</sup>	IONOV, 1993	59.45	112.55	Phlog	3.0	805	Continental Rift	Peridotite
REHFSAF-DJ0216 <sup>2</sup>	IONOV, 1993	59.45	112.55	Phlog	3.1	830	Continental Rift	Peridotite

LEETANZ-001-LB34 <sup>2</sup>	LEE, 1999	-3.6	36.75	Phlog	3.2	1116	Continental Rift	Peridotite
REHFSAF-DJ0217 <sup>2</sup>	LITASOV, 2000	53.5	113.1	Phlog	3.5	914	Continental Rift	Pyroxenite
REHFSAF-DJ0256F <sup>2</sup>	LITASOV, 2000	53.5	113.1	Phlog	4.0	1090	Continental Rift	Peridotite
DANCSAF-RVD175 <sup>2</sup>	LITASOV, 2000	53.5	113.1	Phlog	4.0	1023	Continental Rift	Peridotite
EHRECOL-THUMB-B712 <sup>2</sup>	LITASOV, 2000	53.5	113.1	Phlog	4.1	1253	Continental Rift	Peridotite
EHRECOL-THUMB-H077 <sup>2</sup>	MUKHOPADHYAY, 1994	37.21	-119.26	Phlog	4.2	1159	Convergent Margin	Pyroxenite
DANCSAF-RVD500 <sup>2</sup>	REHFELDT, 2008	-28	24.5	Phlog	4.4	1125	Intraplate, Craton	Peridotite
EHRECOL-THUMB-121 <sup>2</sup>	REHFELDT, 2008	-28	24.5	Phlog	4.4	1064	Intraplate, Craton	Peridotite
EHRECOL-THUMB-F077 <sup>2</sup>	REHFELDT, 2008	-28	24.5	Phlog	4.5	1215	Intraplate, Craton	Peridotite
RUDTANZ-089-674 <sup>2</sup>	REHFELDT, 2008	-28	24.5	Phlog	4.7	1207	Intraplate, Craton	Peridotite
RUDTANZ-089-664 <sup>2</sup>	RUDNICK, 1991	-3.4	36.43	Phlog	4.8	1191	Continental Rift	Peridotite
RUDTANZ-089-664 <sup>2</sup>	RUDNICK, 1991	-3.4	36.43	Phlog	5.2	1263	Continental Rift	Peridotite
DANCSAF-RVD501 <sup>2</sup>	RUDNICK, 1991	-3.4	36.43	Phlog	6.5	1414	Continental Rift	Peridotite
BALIHUN-SZEN-SZB21 <sup>1</sup>	BALI, 2002	46.8	17.3	CaCO <sub>3</sub>	1.6	953	Intraplate, Off-Craton	Peridotite
BALIHUN-SZEN-SZB50 <sup>1</sup>	BALI, 2002	46.8	17.3	CaCO <sub>3</sub>	1.5	815	Intraplate, Off-Craton	Pyroxenite
BALIHUN-SZEN-SZB55 <sup>1</sup>	BALI, 2002	46.8	17.3	CaCO <sub>3</sub>	1.9	913	Intraplate, Off-Craton	Peridotite
BALIHUN-SZEN-SZB59 <sup>1</sup>	BALI, 2002	46.8	17.3	CaCO <sub>3</sub>	2	1014	Intraplate, Off-Craton	Peridotite
CVETSRB-PNB-M/SB2 <sup>3</sup>	CVETKOVIC, 2007	45	19	CaCO <sub>3</sub>	0.9-1.8	N/A	Intraplate, Off-Craton	Peridotite
CVETSRB-PNB-M/SB6 <sup>3</sup>	CVETKOVIC, 2007	45	19	CaCO <sub>3</sub>	0.9-1.8	N/A	Intraplate, Off-Craton	Peridotite
DELPKER-LM/BY96-357 <sup>3</sup>	DELPECH, 2004	-49.5	60.5	CaCO <sub>3</sub>	0.9-1.8	N/A	Intraplate, Off-Craton	Peridotite
DELPKER-LM/BY96-381 <sup>3</sup>	DELPECH, 2004	-49.5	60.5	CaCO <sub>3</sub>	0.9-1.8	N/A	Intraplate, Off-Craton	Peridotite
DEMHUN-001-SZT-1111 <sup>3</sup>	DEMENY, 2004	47.1	17.9	CaCO <sub>3</sub>	0.9-1.8	N/A	Intraplate, Off-Craton	Peridotite
DEMHUN-001-SZT-1130 <sup>3</sup>	DEMENY, 2004	47.1	17.9	CaCO <sub>3</sub>	0.9-1.8	N/A	Intraplate, Off-Craton	Peridotite
IOSPTSB-21-5 <sup>3</sup>	IONOV, 1996	78.93	11.93	CaCO <sub>3</sub>	0.9-1.8	910	Intraplate, Off-Craton	Peridotite
IOSPTSB-21-5 <sup>3</sup>	IONOV, 1996	78.93	11.93	CaCO <sub>3</sub>	0.9-1.8	910	Intraplate, Off-Craton	Peridotite
IOSPTSB-21-6 <sup>3</sup>	IONOV, 1996	78.93	11.93	CaCO <sub>3</sub>	0.9-1.8	930	Intraplate, Off-Craton	Peridotite
IOSPTSB-315-6 <sup>3</sup>	IONOV, 1996	78.93	11.93	Dolomite	0.9-1.8	860	Intraplate, Off-Craton	Peridotite
IOSPTSB-318 <sup>3</sup>	IONOV, 1996	78.93	11.93	Dolomite	0.9-1.8	900	Intraplate, Off-Craton	Peridotite
IOSPTSB-4-24-90 <sup>3</sup>	IONOV, 1996	78.93	11.93	Dolomite	0.9-1.8	980	Intraplate, Off-Craton	Peridotite
IOSPTSB-4-36-90 <sup>3</sup>	IONOV, 1996	78.93	11.93	Dolomite	0.9-1.8	940	Intraplate, Off-Craton	Peridotite
IOSPTSB-4-90-9 <sup>3</sup>	IONOV, 1996	78.93	11.93	CaCO <sub>3</sub>	0.9-1.8	980	Intraplate, Off-Craton	Peridotite
IOSPTSB-43-86 <sup>3</sup>	IONOV, 1996	78.93	11.93	Dolomite	0.9-1.8	920	Intraplate, Off-Craton	Peridotite
IOSPTSB-63-90-18 <sup>3</sup>	IONOV, 1996	78.93	11.93	CaCO <sub>3</sub>	0.9-1.8	870	Intraplate, Off-Craton	Peridotite
LEETANZ-001-LB19-C <sup>3</sup>	LEE, 2000	-4.5	35.4	CaCO <sub>3</sub>	0.9-1.8	N/A	Continental Rift	Peridotite
LEETANZ-001-LB58 <sup>3</sup>	LEE, 2000	-4.5	35.4	CaCO <sub>3</sub>	0.9-1.8	N/A	Continental Rift	Peridotite

LEETANZ-001-MON-CARB <sup>3</sup>	LEE, 2000	-3.25	36.48	CaCO <sub>3</sub>	0.9-1.8	N/A	Continental Rift	Peridotite
LEETANZ-001-PEL2 <sup>3</sup>	LEE, 2000	-3.75	37.75	CaCO <sub>3</sub>	0.9-1.8	N/A	Continental Rift	Peridotite
LUCARG-CNCH-4-227 <sup>3</sup>	LUCASSEN, 2005	-26	-65.75	CaCO <sub>3</sub>	0.9-1.8	N/A	Continental Rift	Peridotite
LUCARG-CNCH-4-229 <sup>3</sup>	LUCASSEN, 2005	-26	-65.75	CaCO <sub>3</sub>	0.9-1.8	N/A	Continental Rift	Peridotite
LUCARG-CNCH-4-301A <sup>3</sup>	LUCASSEN, 2005	-26	-65.75	CaCO <sub>3</sub>	0.9-1.8	N/A	Continental Rift	Peridotite
LUCARG-CNCH-A-113E <sup>3</sup>	LUCASSEN, 2005	-26	-65.75	CaCO <sub>3</sub>	0.9-1.8	N/A	Continental Rift	Peridotite
LUCARG-CNCH-A57-1 <sup>3</sup>	LUCASSEN, 2005	-26	-65.75	CaCO <sub>3</sub>	0.9-1.8	N/A	Continental Rift	Peridotite
SON0166-G035-014 <sup>3</sup>	FRANZ, 2010	-3.5	152.5	CaCO <sub>3</sub>	0.9-1.8	N/A	Convergent Margin	Peridotite

Table 3. Selected trace elements for xenoliths.

<sup>1</sup>Depth reported in PetDB, <sup>2</sup>Depth calculated from Brey and Kohler 1990, <sup>3</sup>Depth limited by spinel

Sample Name	Source	Latitude	Longitude	Pressure (Gpa)	MLD (km)	Ba (ppm)	Nb (ppm)	Zr (ppm)	Y (ppm)	Ba/Nb	Zr/Y	Geologic Setting
Primitive Mantle	Sun, 1982	N/A	N/A	N/A	N/A	6.98	0.713	11.2	4.55	9.8	2.5	N/A
RWCMONA-BD2227 <sup>1</sup>	Carlson, 2004	-28.82	27.42	3.05	60-70	113	7.2	12	2.2	15.7	5.5	Intraplate, Craton
RWCMONA-BD2234 <sup>1</sup>	Carlson, 2004	-28.82	27.42	2.64	60-70	69	4.8	13	2.2	14.4	5.9	Intraplate, Craton
RWCMONA-ROM-189 <sup>1</sup>	Carlson, 2004	-28.82	27.42	3.65	60-70	184	4.8	15	1.7	38.3	8.8	Intraplate, Craton
RWCMONA-ROM-68 <sup>1</sup>	Carlson, 2004	-28.82	27.42	3.83	60-70	37	3.1	15	2.2	11.9	6.8	Intraplate, Craton
RWCMONA-ROM-69 <sup>1</sup>	Carlson, 2004	-28.82	27.42	3.33	60-70	70	7.7	15	1.7	9.1	8.8	Intraplate, Craton
RWCMONA-ROM194A <sup>1</sup>	Carlson, 2004	-28.82	27.42	3.76	60-70	76	5.8	26	5.2	13.1	5.0	Intraplate, Craton
LUGAUST-ARG-6504022 <sup>1</sup>	Luguet, 2009	-16.75	128.3	4.93	80-100	2314	7.88	24	2.55	293.7	9.4	Intraplate, Craton
LUGAUST-ARG-6504072 <sup>1</sup>	Luguet, 2009	-16.75	128.3	5.2	80-100	120	8.8	30.8	1.42	13.6	21.7	Intraplate, Craton
LUGAUST-ARG-6504096 <sup>1</sup>	Luguet, 2009	-16.75	128.3	4.9	80-100	1493	16.9	60.6	3.01	88.3	20.1	Intraplate, Craton
LUGAUST-ARG-6504148 <sup>1</sup>	Luguet, 2009	-16.75	128.3	5.95	80-100	566	7.08	20	3.23	79.9	6.2	Intraplate, Craton
LUGAUST-ARG-6504180 <sup>1</sup>	Luguet, 2009	-16.75	128.3	4.85	80-100	103	6.48	22	3.73	15.9	5.9	Intraplate, Craton
LUGAUST-ARG-6504271 <sup>1</sup>	Luguet, 2009	-16.75	128.3	5.89	80-100	108	7.96	22	7.58	13.6	2.9	Intraplate, Craton
LUGAUST-ARG-6504293 <sup>1</sup>	Luguet, 2009	-16.75	128.3	5.36	80-100	118	6.47	20.3	2.5	18.2	8.1	Intraplate, Craton
MUKMEXI-X12	MUKASA, 2007	19	-100.25	N/A	N/A	51	0.48	17	17.92	106.3	0.9	Convergent Margin
MUKMEXI-X30	MUKASA, 2007	19	-100.25	N/A	N/A	28	0.25	16	8.37	112.0	1.9	Convergent Margin
MUKMEXI-X33	MUKASA, 2007	19	-100.25	N/A	N/A	17	0.09	2	4.61	188.9	0.4	Convergent Margin
MUKMEXI-X4	MUKASA, 2007	19	-100.25	N/A	N/A	42	0.22	8	20.01	190.9	0.4	Convergent Margin
MUKMEXI-X45	MUKASA, 2007	19	-100.25	N/A	N/A	35	0.08	3	8.97	437.5	0.3	Convergent Margin
PETDB-2093-AG3I	WOODHEAD, 2011	18.77	145.67	N/A	N/A	65	0.46	8.7	25	141.3	0.3	Volcanic Arc
PETDB-2093-AG3II	WOODHEAD, 2011	18.77	145.67	N/A	N/A	18.9	0.08	1.5	3.9	236.3	0.4	Volcanic Arc
PETDB-2093-GU7I	WOODHEAD, 2011	17.307	145.845	N/A	N/A	23.3	0.1	5.4	8.9	233.0	0.6	Volcanic Arc
PETDB-2093-GU7II	WOODHEAD, 2011	17.307	145.845	N/A	N/A	51.6	0.2	11.3	20.2	258.0	0.6	Volcanic Arc
PETDB-2093-GUN	WOODHEAD, 2011	17.307	145.845	N/A	N/A	41.7	0.2	4.8	11.3	208.5	0.4	Volcanic Arc
PETDB-2093-PA	WOODHEAD, 2011	18.13	145.8	N/A	N/A	91.9	0.27	8.5	16.6	340.4	0.5	Volcanic Arc
PETDB-2093-SA3	WOODHEAD, 2011	16.708	145.78	N/A	N/A	28.6	0.2	8.5	10.8	143.0	0.8	Volcanic Arc
PETDB-2093-SA4I	WOODHEAD, 2011	16.708	145.78	N/A	N/A	29.8	0.1	2.8	6.1	298.0	0.5	Volcanic Arc
PETDB-2093-SA4II	WOODHEAD, 2011	16.708	145.78	N/A	N/A	115.8	0.5	13.6	20.6	231.6	0.7	Volcanic Arc
PETDB-2093-SAN	WOODHEAD, 2011	16.708	145.78	N/A	N/A	105.4	0.6	9.9	24.3	175.7	0.4	Volcanic Arc
PETDB-1925-FBV	Viccaro, 2009	37	14.6	N/A	N/A	752	70	615	11	10.7	55.9	Intraplate, Off-Craton
PETDB-1943-JMDDL13A	DAY, 2010	28.68	-17.87	N/A	N/A	83.7	12	165	20	7.0	8.3	Intraplate, Off-Craton
JANSLOV-POH-119-5	JANAK, 2006	46.4	15.5	28.37	N/A	5.5	0.08	1.9	2.7	72.4	0.7	Intraplate, Off-Craton
PETDB-1943-JMDDL13B	DAY, 2010	28.68	-17.87	N/A	N/A	73.4	11	142	18	6.7	7.9	Intraplate, Off-Craton

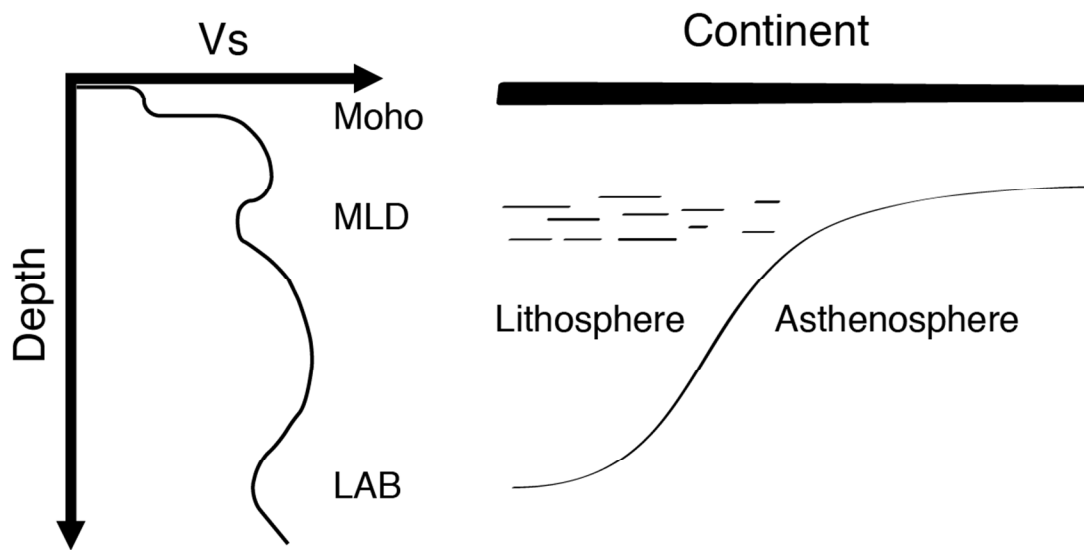


**Figure 1.** Generalized shear velocity profile ( $V_s$ ) underneath a continent showing the inferred relative depths of the mid-lithospheric discontinuity (MLD) and the lithosphere-asthenosphere boundary (LAB).

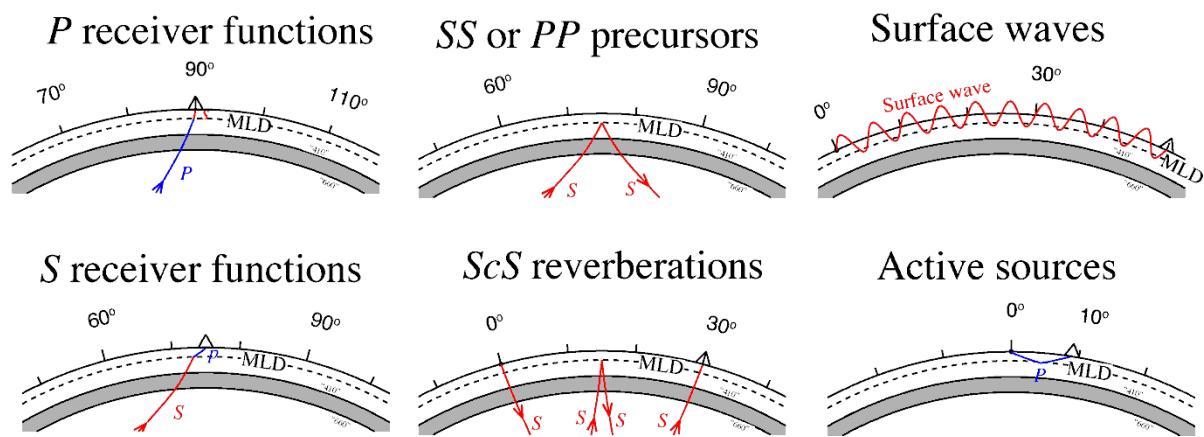


**Figure 2.** Ray paths for the seismic methods used to image the MLD and are cataloged in the database in Table 1. Typical epicentral distances for each phase are indicated in degrees above each cross section.

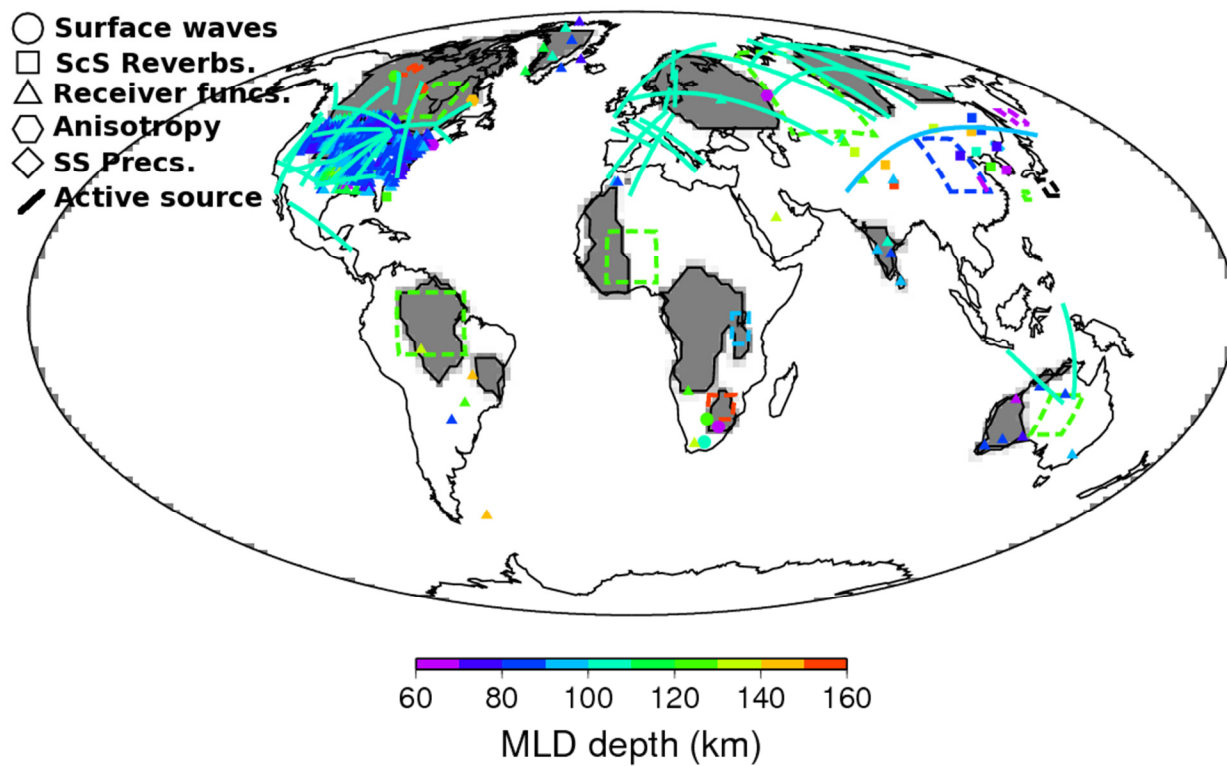


**Figure 3.** Geographic distribution of seismic detections of the MLD from Table 1. Cratonic bodies are indicated in gray. The symbol for each observation indicates the method used and the color indicates the depth at which the MLD was identified.

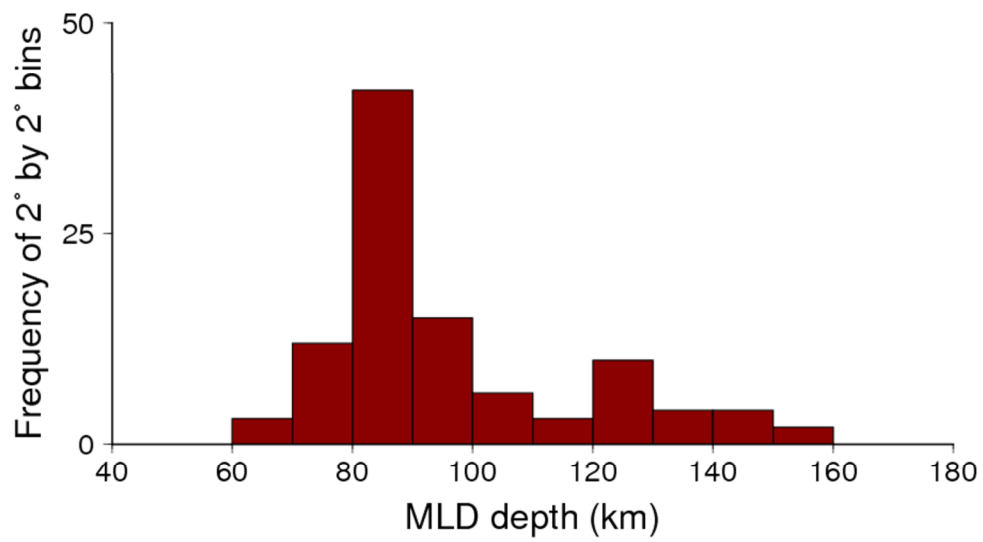


**Figure 4.** Spatial frequency of observed depths of the MLD. This diagram has been normalized to  $2^\circ \times 2^\circ$  bins across the globe.

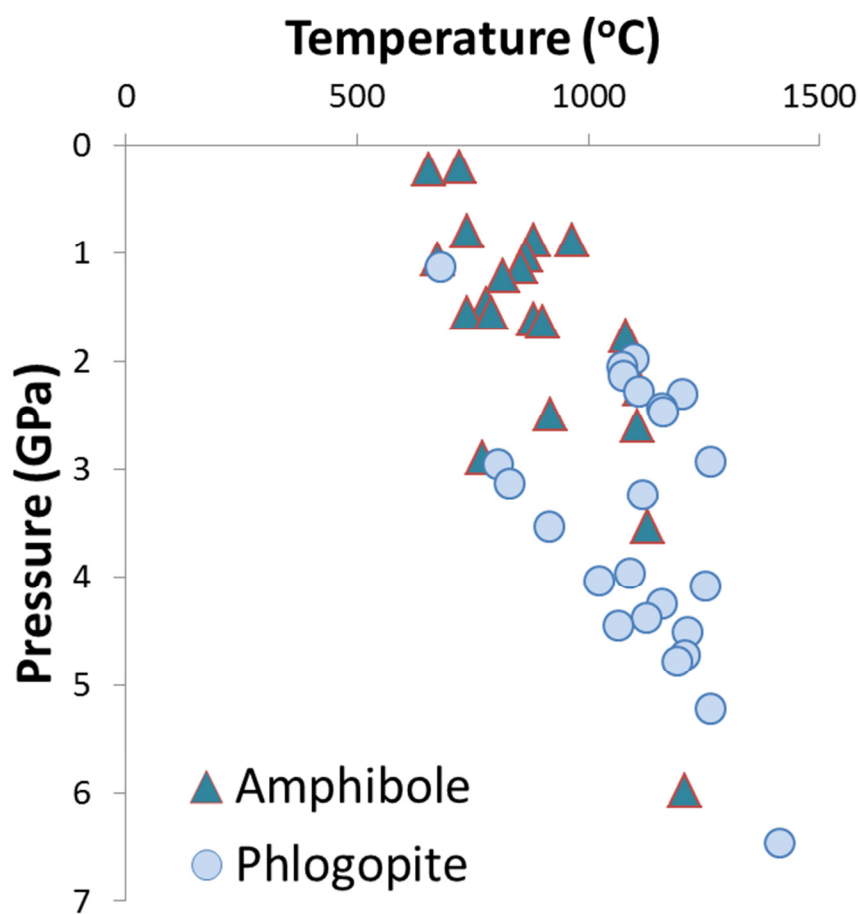


**Figure 5.** Pressure and temperatures of hydrous mineral-bearing xenoliths from PetDB. Dark triangles are xenoliths containing amphibole and lighter circles represent xenoliths that contain phlogopite. A search in PetDB revealed all xenoliths with phlogopite and depth information.

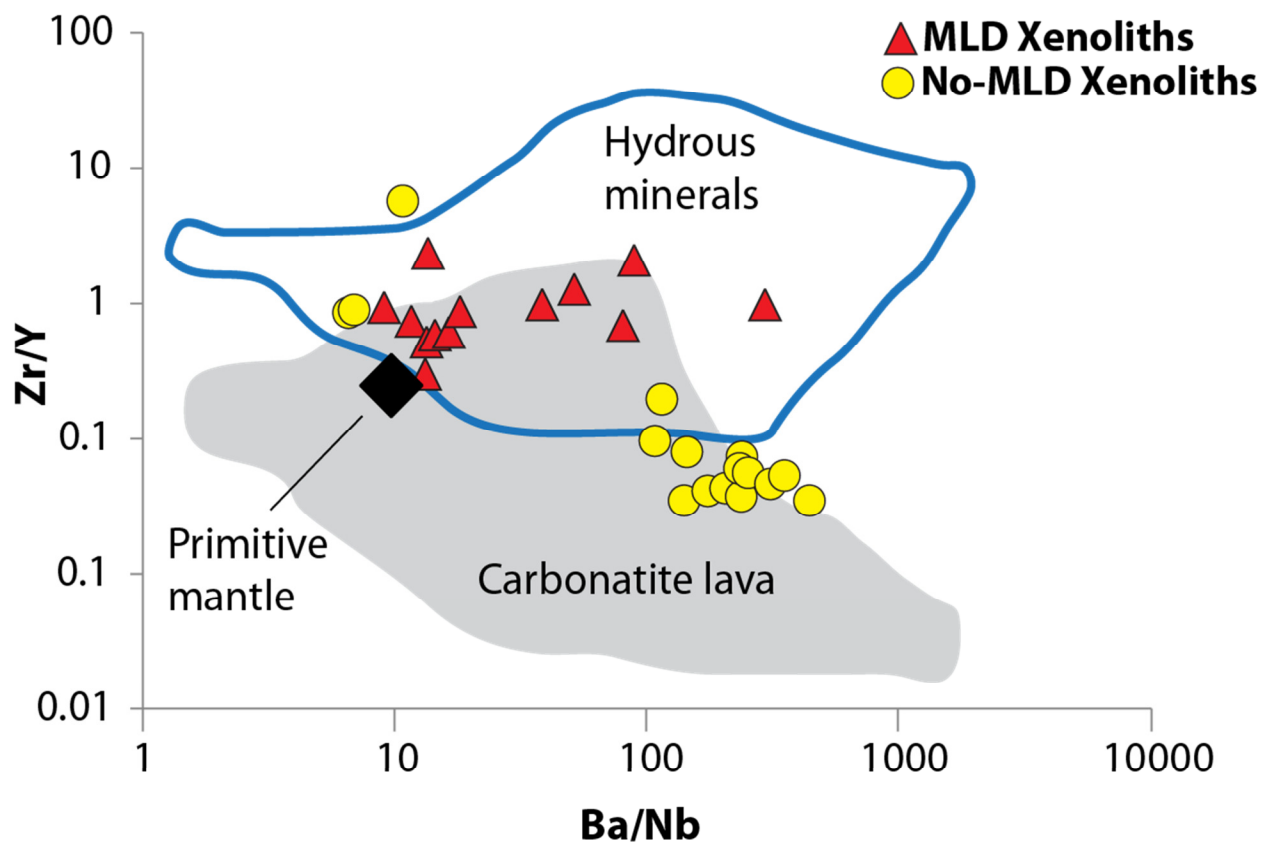


**Figure 6.** Selected trace element ratios for xenoliths from depths and regions where the MLD has been identified (red triangles) and regions or depths where it has not (yellow circles). Primitive mantle is shown as a black diamond, carbonatite lavas are shown in grey, and hydrous mineral analyses in the region outlined by a blue line.

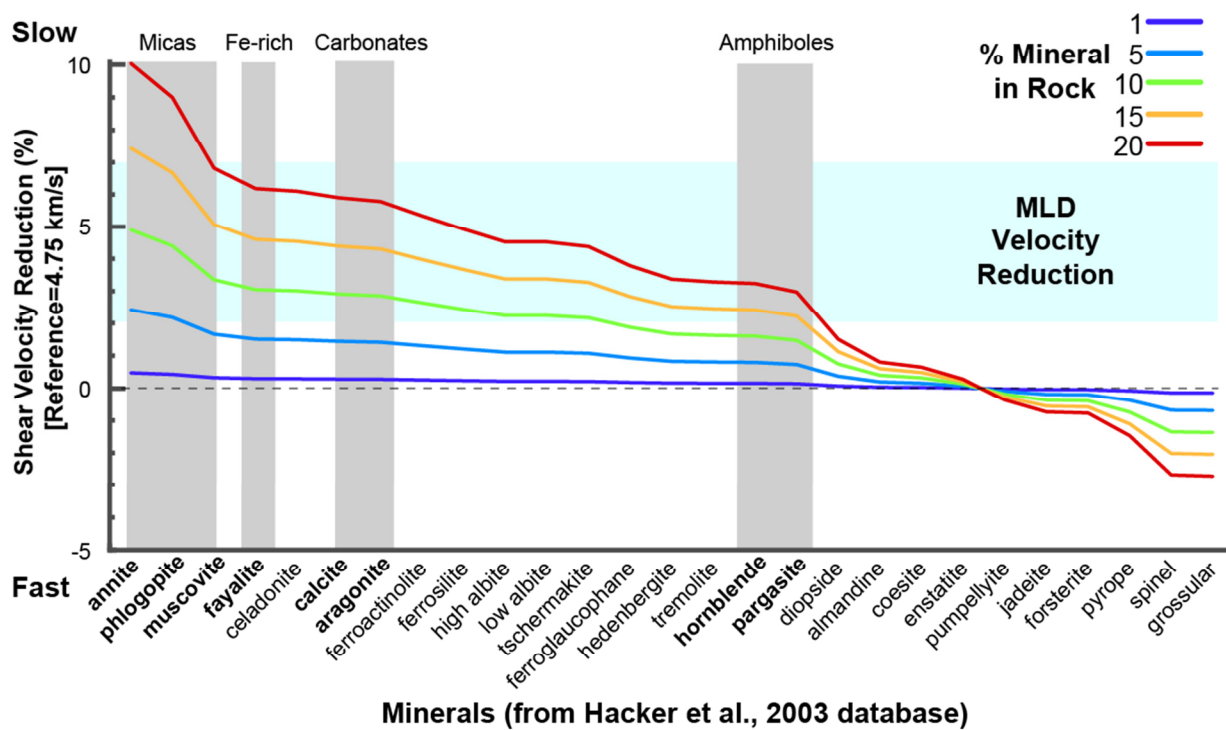


**Figure 7.** Effect of adding proportions of minerals to peridotite on shear velocity. Minerals with largest velocity reduction include iron-rich minerals, micas, carbonates, and amphiboles. The colored lines indicate the necessary proportions to achieve the shear velocity on the left axis.

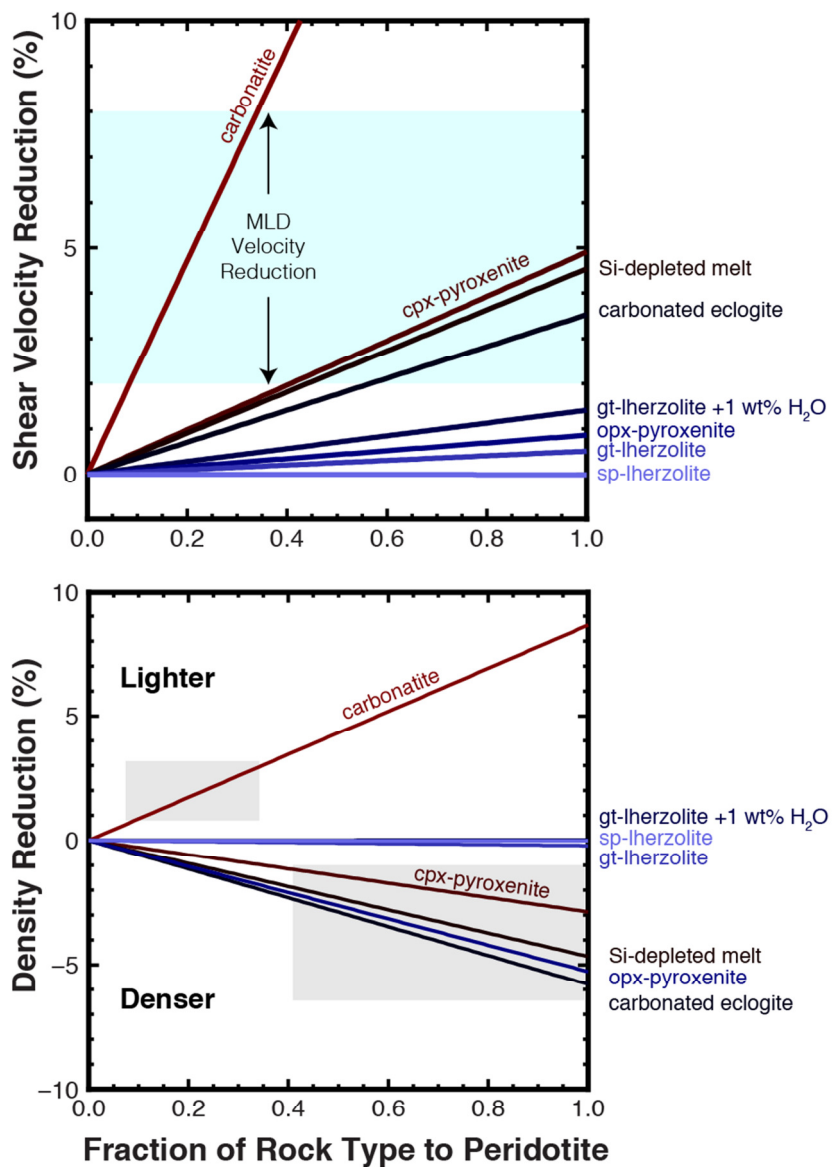


**Figure 8.** Perple\_X models of elastic properties of mantle rock mixtures. The shear velocity for each mixture of peridotite and associated accessory lithology is calculated with the Hill average of a Voigt-Reuss mixture of the two lithologies (see section 5.2).

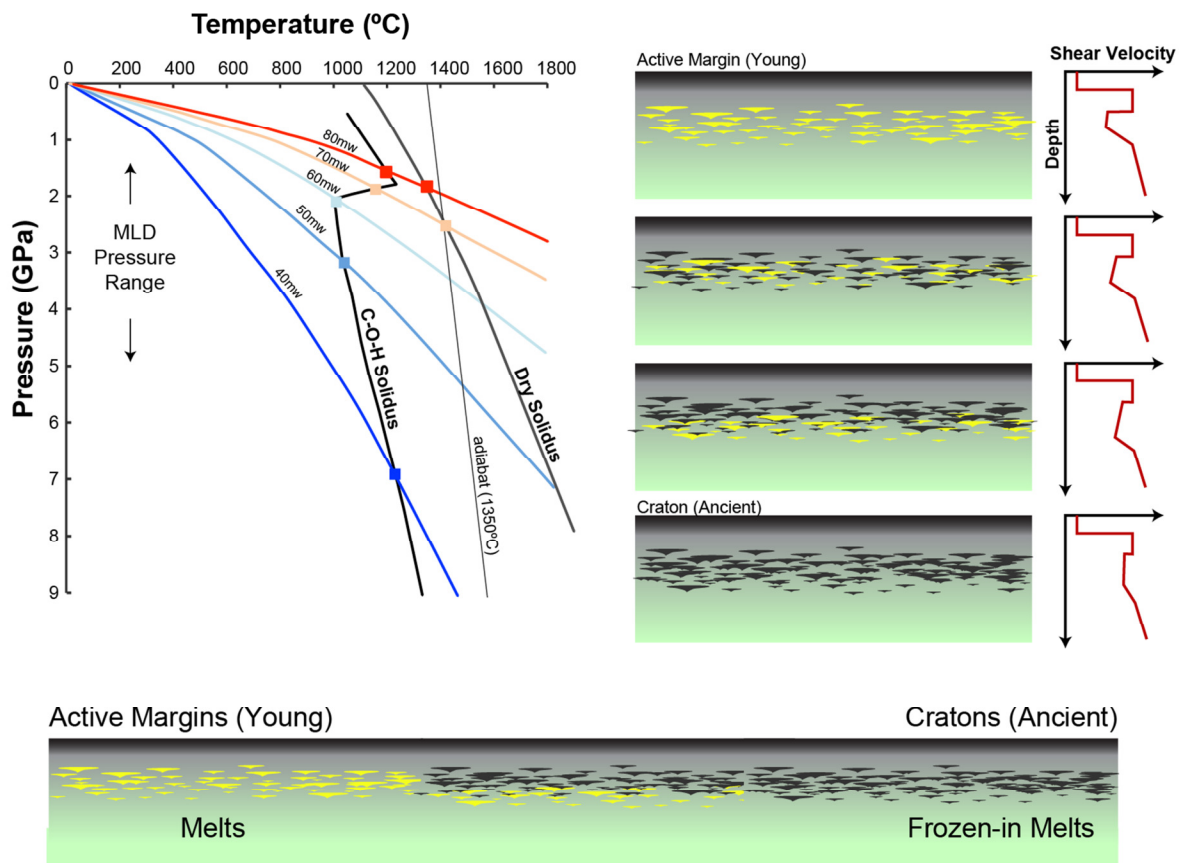


**Figure 9.** Dynamical model of the formation of a trapped melt layer solidifying in ancient crust and creating a chemical boundary at a depth consistent with the present-day MLD. Geothermal gradients illustrate the evolution of crust from hot ( $80 \text{ mW m}^{-2}$ ) to cold craton ( $40 \text{ mW m}^{-2}$ ) through a vapor-saturated solidus in the pressure-temperature diagram. The near horizontal kink in the solidus would result in a natural boundary that would concentrate melt at a narrow horizon, graphically represented on the left as crust aged. The MLD would begin to develop as a physical boundary between the lithosphere and asthenosphere, but as crust cooled and the LAB deepened, the chemical signature remains at the same depth.

### **Chapter 3. Hot clasts and cold blasts: Thermal heterogeneity in boiling-over pyroclastic density currents**

Erika Rader, Dennis Geist, John Geissman, Joe Dufek, Karen Harpp

#### Abstract

Paleomagnetic data, in the form of progressive thermal demagnetization results, from pyroclastic deposits provide information on the emplacement temperatures of both lithic and juvenile magmatic clasts contained in the deposits. We collected paleomagnetic data from pyroclastic deposits from two volcanoes in Ecuador, the 2006 eruption at Tungurahua and the 1877 eruption at Cotopaxi, which both commonly erupt what have been referred to as “boiling-over” pyroclastic flows, emplaced as pyroclastic density currents (PDCs). Most pyroclastic flow deposits from these volcanoes are similar and are characterized by cauliflower-textured scoria clasts up to 1 m in diameter and a diverse assemblage of lithic clasts surrounded by an unwelded ashy matrix. On the basis of progressive thermal demagnetization experiments, we infer that emplacement temperatures for most of the lithic clasts in PDC deposits are below 90°C, but the deposits also contain juvenile clasts that we interpret to have been deposited at temperatures above 540°C. These data indicate the PDC was thermally heterogeneous over short length scales (decimeters) and even after emplacement, contrary to the hypothesis that PDC deposits cool en masse. We hypothesize that PDCs emplaced by the boiling-over mechanism cool quickly from atmosphere entrainment, causing the juvenile clasts to form a rind that retains heat and that also prevents lithic clasts from appreciable heating. Several deposits on Cotopaxi, despite being morphologically similar to the PDC deposits, contain both cold lithic and juvenile clasts, which we interpret to be lahar deposits formed by PDCs traveling across glacial ice and snow. Rare deposits containing both hot lithic and hot juvenile clasts are classified as well-mixed, hot PDCs and were erupted during a more energetic phase at Tungurahua.

#### 1. Introduction

Eruptions in 2006 at Tungurahua volcano and in 1877 at Cotopaxi volcano, northern Ecuador, produced similar deposits, which resulted from similar eruption styles that have been described as ‘boiling-over’ (Kelfoun *et al.* 2009; Wolf 1878; Hall & Mothes 2008). Boiling-over occurs when

strongly vesiculated magma fountains or froths over a crater rim without forming a convective plume (or the plume is a small fraction of the eruptive output). The process is a poorly understood phenomenon, despite being widely cited to explain unusual pyroclastic deposits (e.g., Fulop 2002; Freundt 1999; Soler *et al.* 2007; Carrasco-Nunez & Rose 1995).

The 1877 Cotopaxi and 2006 Tungurahua boiling-over eruptions produced a characteristic type of pyroclastic density current (PDC) deposit, which is unusually rich in giant scoria bombs. These deposits are paradoxical, because charred wood and fluidal juvenile clasts suggest hot emplacement temperatures, yet the presence of un-charred wood and un-melted plastic have been interpreted to indicate low temperatures. We have attempted to estimate the deposition temperatures of lithic and juvenile clasts within these PDC deposits using the common paleomagnetic method of progressive thermal demagnetization (Paterson *et al.* 2010 and references therein), to examine the possibility that a pre-existing remanence in the lithic and juvenile clasts has been partially to completely thermally unblocked after the deposits came to rest, at elevated temperatures. We have supplemented this information with rock magnetic data. Because PDCs have strongly impacted the communities around Tungurahua and Cotopaxi, a better understanding of the eruption styles and emplacement mechanisms will advance efforts to minimize damage in future eruptions.

## 2. Background

### 2.1 Location and eruptive history

Cotopaxi and Tungurahua are stratovolcanoes located in the Andes of north-central Ecuador (Fig. 1). Cotopaxi is 50 km south of the capital city of Quito, and Tungurahua is 90 km farther south. Both Cotopaxi and Tungurahua have erupted PDCs that are generated by a boiling-over style, and the volcanoes' eruptive products are similar, especially the scoria-bomb PDC deposits (Wolf 1878; Kelfoun *et al.* 2009; Hall & Mothes 2008). Products from both volcanoes range from mafic andesite to dacite and rhyolite (Samaniego *et al.* 2011; Hall & Mothes 2008), but the most recent eruptions are almost entirely andesitic.

Between 1600 and 2000 CE, Tungurahua has 15 eruptions listed in the Smithsonian Global Volcanism Program database. Eruptions have been moderately explosive, typically VEI 2 to 4, and have produced lava flows, tephra, and PDCs. The flanks of the volcano are populated with farms and villages, and the town of Baños (current population: 9500; Fig. 2A) is ~8 km away from the summit vent. Several larger eruptions have damaged property and caused fatalities, including the eruptions

of 1886, 1916, and the recent cycle, which began in 1999. From 1999-2006, the activity at Tungurahua was mostly Strombolian, but in 2006 it became more explosive (Steffke *et al.* 2010). Steffke *et al.* (2010) used thermal infrared cameras to demonstrate that large amounts of air were entrained into the PDCs and the plume during the 2006 eruption. Tungurahua's activity continues to the present day. The paroxysm was in July and August, 2006, which produced explosions, lahars, lava flows, tephra, and PDCs (Samaniego *et al.* 2011; Douillet *et al.* 2013a,b). We focus on the 2006 PDC deposits in this study.

Twenty-four eruptions have occurred at Cotopaxi since the early 1700s, the most noteworthy being in 1768 (Pistolesi *et al.* 2011; Wolf 1878), which produced a lahar that traveled over 320 km in 18 hours (Mothes *et al.* 1998). The eruption in 1877 produced PDCs that melted much of the glacial icecap and also produced large-volume lahars (Fig. 2B) (Pistolesi *et al.* 2013). Tephra fell for several hours, and the final gasp of the eruption resulted in several thick andesite lava flows, which only traveled a few hundred meters from the summit (Pistolesi *et al.* 2011). We focused on the 1877 deposits at Cotopaxi, although similar deposits are abundant in the geologic record there.

## 2.2 Pyroclastic density currents from boiling-over eruptions

Pyroclastic density currents are produced by lateral blasts, dome collapse, column collapse, and pyroclastic fountaining (Branney & Kokelaar 2002). Most commonly, strong pyroclastic eruptions generate columns that lose their initial buoyancy and collapse to form PDCs. Low fountains lack convective columns and begin to flow as density currents as soon as they breach the crater rim (Fig. 3). These are referred to as "boiling-over" eruptions, a term coined from the 1877 eruption at Cotopaxi (Wolf, 1878).

Boiling-over eruptions have been witnessed and described at several volcanoes (e.g. Hall *et al.* 2013; Shea *et al.* 2011; Clarke *et al.* 2002; Hoblitt 1986; Taylor 1958; Wolf 1878) and inferred by inspection of deposits from unwitnessed eruptions (e.g., Fulop 2002; Soler *et al.* 2007; Carrasco-Nunez & Rose 1995). Numerical models have simulated PDCs sourced by boiling-over fountains (Clarke *et al.* 2002; Freundt 1999; Dufek & Bergantz 2007). Conditions in the models that result in boiling-over eruptions are high volume flux coupled with low exit velocity (Dufek & Bergantz 2007) and a low volatile content (Clarke *et al.* 2002; Myers *et al.* 2012). We also contend that the relatively low viscosity of mafic andesite plays a role in producing a boiling-over fountain as opposed to a

buoyant column, because measurements of pre-eruptive water contents in melt inclusions from 2006 Tungurahua products indicate concentrations up to 4% (Myers *et al.* 2012).

Density currents produced by boiling-over eruptions have short run-out distances due to their low initial velocity, and they tend to produce thick, poorly sorted deposits (Dufek & Bergantz 2007). Several studies interpret PDC deposits that lack contemporaneous large-volume fallout deposits as resulting from a boiling-over mechanism, exemplified by Chitelaltepetl volcano, Mexico (Carrasco-Nunez & Rose 1995; Branney & Kokelaar 2002). Some workers have proposed that boiling-over PDCs entrain less of the ambient atmosphere than other PDC types, resulting in little cooling of the flow prior to deposition (Freundt 1999; Cioni *et al.* 2004). Boiling-over has also been invoked for silicic eruptions, on the basis of interpretations of relatively high emplacement temperatures (Lesti *et al.* 2011), which have been attributed to the lack of atmospheric entrainment during flow. These deposits include welded units in the Gutai Mountains of Romania, Vilama in the Central Andes, Grey's Landing in the USA, the Garth tuff in Wales, the 79 AD eruption at Vesuvius in Italy, and the Cerro Galan ignimbrite, NW Argentina (Fulop 2002; Soler *et al.* 2007; Andrews & Branney 2011; McArthur & Orton 1998; Cioni *et al.* 2004; Cas *et al.* 2011; Lesti *et al.* 2011). We question the inference that boiling over results in less entrainment of air and less cooling during transport and deposition of PDCs, interpretations that are inconsistent with abundant evidence for substantial entrainment in collapsing fountains and jets (Hall *et al.* 2013; Suzuki *et al.* 2005 and references therein) as well as our observations of the physical characteristics of the Cotopaxi and Tungurahua deposits, and the paleomagnetic data we report in this paper.

### 2.3 Estimation of temperature of volcanic deposits using paleomagnetic methods

The extent of carbonization of wood (Sawada *et al.* 2000; Scott & Glasspool 2005), observations made during eruption (Fujinawa *et al.* 2008), thermal imaging, and paleomagnetic data based on progressive thermal demagnetization and the resolution of magnetization components acquired prior to and following mechanical emplacement of discrete clasts have been used to identify PDCs that were deposited at relatively cool temperatures (e.g. Cioni *et al.* 2004; Sawada *et al.* 2000). Estimated emplacement temperatures of PDC deposits range from  $\sim 48^{\circ}\text{C}$  (Sparks *et al.* 2002) to  $\sim 700^{\circ}\text{C}$  (Nogami *et al.* 2001), and estimates of temperature can vary by  $200^{\circ}\text{C}$  to  $300^{\circ}\text{C}$  within different parts of a single deposit (e.g. Bardot 2000; Zlotnicki *et al.* 1984; Paterson *et al.* 2010). In principle, progressive thermal demagnetization data provide a robust method to determine the

emplacement temperature of individual clasts, allowing for a detailed perspective of the thermal conditions during deposition of a PDC.

Heating of (accidental) lithic clasts incorporated within a PDC thermally resets the magnetization by partial to complete unblocking of a previous remanence, usually a thermoremanent magnetization (TRM) if the clast is of volcanic origin. Heating takes place from the outside of the lithic fragment to its core, whereas the cooling of a juvenile (magmatic) clast blocks the TRM and the fragment cools from the rim inward. As a clast cools, magnetization blocking will result in a TRM or partial TRM aligned with the Earth's magnetic field at the time of cooling. The total TRM is acquired as a single direction of magnetization if the fragment remains stationary during complete magnetization blocking from elevated temperatures. If the fragment changes its orientation during magnetization blocking, then the total TRM acquired is a composite of magnetizations of different directions. Each component of magnetization acquired at a discrete temperature interval will be unblocked if heated above about that same temperature interval, assuming that heating and cooling are both rapid (McClelland & Druitt 1989; Paterson *et al.* 2010). It is predicted that if a clast was deposited above the Curie point (maximum blocking temperature) or was never reheated in the deposit, it will have a single component of magnetization, as revealed by unidirectional decay of the remanence. In the case of no reheating, the direction of the magnetization will be random among different clasts having the same thermal history. If a reheated clast attains a temperature below the Curie point after it has been deposited, or if it is transported as it cools, then a clast can subsequently block multiple components of magnetization, as partial thermoremanent magnetizations (PTRMs). Progressive thermal demagnetization, in principle, can isolate components acquired as a result of thermal resetting and thus provide estimates of the emplacement temperature of the clasts within a deposit.

Typically, the emplacement temperature of a clast is interpreted as the maximum laboratory unblocking temperature ( $T_{ub}$ ) of the remanence that is well-grouped and that has a direction that is aligned with the geomagnetic field at the time of cooling, and thus inferred to have been acquired (blocked) after the deposit came to rest (e.g. Clement *et al.* 1993; Bardot 2000; Paterson *et al.* 2010). Alternatively, another group of researchers recommends excluding extreme values of high and low laboratory unblocking temperatures ( $T_{ub}$ ) to determine the predominant temperature of the deposit (Cioni *et al.* 2004; Zanella *et al.* 2007; Di Vito *et al.* 2009; Zanella *et al.* 2008). For this study, we refer

to “low” or “cold” emplacement temperatures as those ranging from 50 to 210°C, whereas “hot” emplacement have temperatures ranging from 500 to 600°C.

### 3. Methods

#### 3.1 Sample collection and preparation

Clasts were collected from two PDC deposits emplaced during the August 2006 Tungurahua eruption and from three valley-filling PDC deposits from the 1877 eruption at Cotopaxi (Fig. 2). We collected 18 oriented samples from nine different locations at Tungurahua (one lithic clast and one juvenile clast at each site). Another 18 oriented clasts were collected (one lithic clast and one juvenile clast) from each of nine locations at Cotopaxi. The flows, sample type and number can be found in Table 1 and the locations can be found in Fig. 2.

Juvenile clasts from these scoria-rich PDC deposits have a highly-vesicular, cauliflower-like morphology, are fragile, and are polygonally jointed. Most have a breadcrust texture and many droop over irregularities in the surface on which they were deposited (Fig. 4). Most lithic clasts have low vesicularity and a weathered or altered exterior. We cut sections from rim to core of each juvenile clast and prepared each section into 2.5 cm cubes, while maintaining their orientation, using a non-magnetic diamond saw blade. Lithic clasts were cored using a 2.5 cm diameter, water-cooled non-magnetic diamond bit with a drill press.

#### 3.2 Magnetization measurements

The monitoring of bulk susceptibility as a function of heating and cooling to temperatures above about 640°C was conducted on an AGICO CS4 instrument interfaced with an AGICO MFK1A magnetic susceptibility instrument at the University of Texas at Dallas. Heating and cooling curves were obtained while the specimen, either crushed whole rock or a magnetic separate, was immersed in argon.

Rim and core specimens from the 36 oriented clast samples were progressively thermally demagnetized in the Paleomagnetism Laboratory at the University of New Mexico. Demagnetizations were carried out in air with an average of 11 steps in a magnetically shielded furnace (ASC TD 48) up to temperatures of about 590°C. The remanence was measured for each sample after every heating step using standard procedures on a 2G Enterprises Model 760R three-axis DC SQUID-based superconducting rock magnetometer in a magnetically shielded environment constructed by

Lodestar Magnetics. Demagnetization data were evaluated on orthogonal demagnetization diagrams and equal area projections using PaleoMag v 3.1b2 (Jones 2002). The remanence unblocked at the lowest temperature steps (25°C and 90°C) was excluded from analysis to avoid possible inclusion of viscous remanent magnetization (VRM; Bardot & McClelland 2000). Because of the relatively low variation in  $T_{ub}$  values estimated in this study, we do not exclude any measured values based on deviation from the mean.

## 4. Results

### 4.1 Description of deposits

Most of the PDC-transported material from the 2006 eruption at Tungurahua volcano and the 1877 eruption at Cotopaxi volcano was deposited in large fans at slope breaks at the mouths of deep valleys (Fig. 5). The bulk of the deposits are between 1 and 10 m thick and exhibit reverse grading of the coarse particles, with large cauliflower scoria bombs sitting on top of an ash-rich matrix.

Thorough description of the 2006 Tungurahua PDC deposits can be found in Hall *et al.* (2013) and Douillet *et al.* (2013a,b). Granulometric analyses performed at 16 sites at Tungurahua reveal a fines-skewed deposit with a median grain size of 2.5 mm. A lateral facies comprises fine ash, typically <1 mm diameter, which was deposited as a veneer high on the walls of the canyons but mostly washed away within a few days of deposition. The smaller grains in the deposit are dominantly juvenile ash with lithic clasts, typically having a grain size >8 mm. At both volcanoes, lithic clasts vary widely in shape and composition, with some having more angular edges and others being well rounded. Lithic clasts range from fragments of old, altered andesitic lava to dense fresh andesite that we interpret as being derived from the conduit. Cotopaxi PDC deposits from the 1877 eruption are similar to those at Tungurahua, with meter-scale cauliflower scoria bombs resting on beds of finer-grained lapilli and ash. These deposits are described in detail in Mothes *et al.* 1998 and Garrison *et al.* 2011.

### 4.2 Rock magnetism

Low-field bulk susceptibility versus temperature curves during heating and cooling of representative samples of juvenile and lithic clasts from the Cotopaxi and Tungurahua deposits show that juvenile clasts from both deposits have Curie temperatures between about 360 and 400°C

(Figures 6 and 7). Because our samples were cut into 1 cm cubes, each measurement is an average over that volume. Rim and core samples from the same clast have similar Curie temperatures except for the lithic clast from Co-10-09, where the rim had a lower Curie temperature by  $\sim 100^{\circ}\text{C}$  (Fig. 6). Lithic clasts from both deposits are characterized by Curie temperatures between  $550$  and  $580^{\circ}\text{C}$ . In some cases (e.g. TU-10-04 Juvenile [core and rim] Fig. 7) there is a clear mixture of phases with different Curie temperatures. In most cases, the heating and cooling curves are close to identical, if not virtually reversible (e.g. CO-10-08 Juvenile [core]; TU-10-05 Juvenile [core and rim]). Many of the samples show a strong Hopkinson effect, in both heating and cooling.

#### 4.3 Juvenile clasts

With a few exceptions, juvenile clasts from Cotopaxi and Tungurahua yield a well-defined response to thermal demagnetization with NRM intensity ranging from  $0.04$ - $23 \text{ A m}^{-1}$ . The remanence in each sample was fully unblocked after treatment to between  $500$  and  $590^{\circ}\text{C}$ . Demagnetization trajectories are typically well-defined until magnetization unblocking of more than 99% of NRM has been reached, at which point essentially random directions are measured at each subsequent demagnetization step (Fig. 8). Analysis of the directional components in the samples reveals between one and three components. The low temperature component is defined as  $T_{\text{ub}} < 210^{\circ}\text{C}$  and typically has an intensity of around  $0.25$ - $2.5 \text{ A m}^{-1}$ . The medium unblocking temperature component is typically unblocked over the temperature range from  $210$  to  $500^{\circ}\text{C}$  and is directionally uniform in the juvenile clasts. The highest-temperature component is apparent at  $T_{\text{ub}} > 500^{\circ}\text{C}$ , and its direction can deviate from previously unblocked components but usually accounts for less than 1% of the NRM. Progressive thermal demagnetization data indicate that the multiple specimens measured from each clast all have three distinct directions and these can be compared with the magnetic field at the time they were cooling (Fig. 8).

The natural magnetic field in the vicinity of Tungurahua had a declination of  $-2^{\circ} 2'$  and an inclination of  $+20^{\circ} 14'$  in 2006 (Perrin et al. 1998). The magnetic field for Cotopaxi in 1900 had a declination of  $7^{\circ} 16'$  and an inclination of  $+16^{\circ} 48'$  (Fig. 9 and 10). Maximum  $T_{\text{ub}}$  for specimens of juvenile clasts is about  $590^{\circ}\text{C}$ , and the distribution of magnetizations isolated from almost all the samples from these clasts overlaps the ambient magnetic field at the time of deposition (Fig. 9). Our straightforward interpretation is that all but two of the juvenile clasts from Cotopaxi and one from Tungurahua were deposited above  $590^{\circ}\text{C}$  (Table 1).

Three exceptional juvenile clasts (Tu-10-07, Co-10-06, and Co-10-03; Table 1; Fig. 2) reveal a systematic change in direction of progressive demagnetization (Fig. 11). The lower  $T_{ub}$  components yield magnetizations that are  $> 30^\circ$  from the geomagnetic field at the time of emplacement. For specimens from the core of sample Tu-10-07, the first removed magnetization component (up to a temperature of about  $590^\circ\text{C}$ ) has a direction that differs from the geomagnetic field at the time of emplacement by  $30\text{--}60^\circ$  (Fig. 12). At progressively higher  $T_{ub}$ , the inclination remains constant, but the declination changes to about  $320^\circ$ . Specimens from the rim of this sample yield magnetizations that exhibit a progressive shift in declination from about  $320^\circ$  at low demagnetization temperatures to  $\sim 180^\circ$  at high temperatures (Fig. 12). Like the other juvenile clasts, specimens from clast samples Co-10-06 and Co-10-03 yield a single direction of magnetization over the entire  $T_{ub}$  spectra (Fig. 11). Both samples come from a lahar deposit that was thought to have been transformed from a PDC by incorporation by melt water (Pistolesi et al. 2013).

#### 4.4 Lithic clasts

Most lithic clasts exhibit similar demagnetization magnetic behavior to that of juvenile clasts and have NRM intensities that range from  $0.01\text{--}25 \text{ A m}^{-1}$ , with magnetization unblocking taking place between  $25^\circ\text{C}$  and  $575^\circ\text{C}$ . The three types of magnetization components that are identified for most juvenile clasts are also detected in the lithic samples. The first-removed, low  $T_{ub}$  magnetization components are scattered, as are the highest  $T_{ub}$  components. However, the principal magnetization component between the high and low  $T_{ub}$  is consistent in magnetization direction. Directions of the principal magnetization component isolated from lithic clasts from Tungurahua are dispersed, with declinations that vary from  $0\text{--}30^\circ$ ,  $90\text{--}120^\circ$ , and  $200\text{--}290^\circ$  and inclinations between  $0\text{--}90^\circ$  (Fig. 10). Directions of principal magnetization components at Cotopaxi mostly cluster in the NE quadrant (mean direction of  $D = 14.4$ ,  $I = +33.8$ ,  $\alpha_{95} = 16.4$ , and  $n = 20$  specimens; Fig. 10). The distribution of magnetization directions within the northeast quadrant implies a non-random population, yet the directions are dispersed, in contrast to magnetizations isolated from juvenile clasts at both high and low  $T_{ub}$  intervals (Fig. 10). The degree of oxidation of the glass within the lithic clasts does not appear to have any effect on the principle component of paleomagnetic data. Two lithic clasts at Tungurahua have high  $T_{ub}$  magnetizations that are similar in direction to that of the geomagnetic field. Sample Tu-10-01 yields magnetizations of low  $T_{ub}$  that cluster around the geomagnetic field up to about  $210^\circ\text{C}$  (Fig. 13). Such demagnetization behavior is observed in

specimens from both the core and the rim of this sample. Several other samples were collected from the same flow deposit as Tu-10-01, however, none of them show this behavior.

Specimens from sample Tu-10-02, on the other hand, exhibit a single component of magnetization, with a broad  $T_{ub}$  spectrum ranging from 90-575°C, and the magnetizations isolated in these specimens cluster around the geomagnetic field as seen in Figure 10, similar to those from the juvenile samples. Tu-10-02 is the only example of a lithic clast that appears to have been sufficiently heated in situ to completely unblock its initial remanence. This sample was collected from a PDC deposit that crossed the Chambo River, one of the farthest traveled PDCs of the 2006 eruption.

## 5. Discussion

### 5.1 Emplacement temperatures at Tungurahua and Cotopaxi

Because the remanence preserved in an assemblage of magnetic phases in volcanic rocks is blocked over a range of temperatures during cooling, paleomagnetism can be used to estimate the emplacement temperature of volcanic deposits (e.g. Aramaki & Akimoto 1957, Bardot 2000, Mandeville *et al.* 1994). The temperature at which the mean direction within a clast deviates from the geomagnetic field at the time of deposition indicates the minimum emplacement temperature. If the mean direction is defined by a single component of magnetization that is consistent with the ambient geomagnetic field direction at the time of emplacement of the deposit, then the minimum emplacement temperature is above the Curie temperature (maximum blocking temperature) for that rock.

All of the specimens prepared from juvenile clasts at Tungurahua exhibit a single component of magnetization that is isolated up to 500-590°C, which is similar to the expected geomagnetic field direction at the time of emplacement, similar to the findings of another paleomagnetic study at Tungurahua also conducted on juvenile clasts from the 2006 eruption (Roperch *et al.* 2014). We interpret these results to indicate that all the juvenile clasts were emplaced at temperatures >400°C, on the basis of the bulk susceptibility vs. temperature data, and perhaps >500° to 590°C.

In the case of lithic clasts at Tungurahua, the single magnetization component is dispersed and unaligned with the geomagnetic field at the time of eruption. Thus, these clasts remained below ~ 90°C as they were incorporated, transported, and deposited by the PDC, even within 1 cm of the rim. At Cotopaxi, seven of the nine localities include juvenile clasts that were emplaced above 590°C, whereas all of the lithic clasts were emplaced below 90°C. Two lithic clasts sampled in the Juive

Grande (Tu-10-01) and Aschupashal (Tu-10-02) valleys at Tungurahua are interpreted to have been emplaced at  $\sim 210^{\circ}\text{C}$  and  $>590^{\circ}\text{C}$ . These two lithic clasts that were heated above  $\sim 100^{\circ}\text{C}$  may have been incorporated in the conduit, which would have encased them in hotter regions of the flow for a longer time. Another possibility is that the heated lithic clasts originate from the more explosive and energetic phase of the 2006 eruption, which entrained less air. The lithic clast which had been completely reset, Tu-10-02, was collected from a deposit that originated from the only eruption that produced a PDC with enough energy and mass to dam and jump the Chambo river, suggesting it may have retained more heat during transport (Hall *et al.* 2013). These observations imply large variations of temperature ( $>500^{\circ}$  difference) in the flows and the deposits. An important finding is that for the most part the deposits must not have been hot enough to heat the outermost 1 cm of the lithic clasts.

Other paleomagnetic studies conducted on juvenile materials with high laboratory unblocking temperatures have concluded that a chemical remanent magnetization (CRM) can mask the thermoremanent magnetization (TRM), which will be apparent by a curvature in demagnetization trajectories in demagnetization diagrams (Zlotnicki *et al.* 1984; Bardot & McClelland 2000; Bardot *et al.* 1996; McClelland & Druitt 1989). Little curvature is observed in our samples; consequently, we believe that the emplacement temperatures estimated from the scoria bombs are free from CRM. The lack of juvenile material accompanying steam eruptions at Adatara, Bandai, and Zao volcanoes, Japan, led to the hypothesis that the deposits were all emplaced at less than  $100^{\circ}\text{C}$  (Fujinawa *et al.* 2008). Other relatively low emplacement temperature estimates for PDC deposits were measured with thermocouples, including deposits from Mount Etna at  $\sim 200^{\circ}\text{C}$  (Belousov *et al.* 2011), Montserrat at  $48^{\circ}\text{C}$  (Sparks *et al.* 2002), and Mount St. Helens between  $50^{\circ}\text{C}$  and  $250^{\circ}\text{C}$  (Banks & Hoblitt 1996).

Paleomagnetic studies of PDC deposits from silicic volcanic systems have also yielded relatively low estimates of emplacement temperatures: Colli Albani,  $>160^{\circ}\text{C}$  (Porreca *et al.* 2008); Ruapehu,  $<100^{\circ}\text{C}$  (Smith *et al.* 1999); Vesuvius,  $>180^{\circ}\text{C}$  (Cioni *et al.* 2004); Santorini,  $>160^{\circ}\text{C}$  (Bardot 2000); and Taupo,  $>150^{\circ}\text{C}$  (McClelland *et al.* 2004). In many of these examples, the presence of uncharred organic matter is cited as evidence indicating moderate emplacement temperatures, because temperatures must have been above 250 to  $300^{\circ}\text{C}$  to char the wood (Sawada *et al.* 2000; Scott & Glasspool 2005; Scott *et al.* 2008). Physical characteristics of low-temperature PDC deposits include unwelded, poorly sorted deposits (Fujinawa *et al.* 2008), uncharred vegetation (e.g.

McClelland *et al.* 2004; Sparks *et al.* 2002), and in some, accretionary lapilli (e.g. Porreca *et al.* 2008; Belousov *et al.* 2011; Cioni *et al.* 2004). In summary, a wide range of emplacement temperatures for PDC deposits has been documented in volcanoes around the world, and emplacement temperatures for clasts between 50 and 300°C in these deposits are not uncommon. As far as we know, however, a broad range of emplacement temperatures has not been determined for both lithic and juvenile clasts in a single deposit, as is demonstrated here.

Independent of our paleomagnetic measurements, no estimates of emplacement temperatures have been made from the 1877 deposits at Cotopaxi; the volcano is uninhabited and is mostly glaciated or in an otherwise poorly vegetated environment. Locally uncharred wood (Pollock *et al.* 2010), unmelted plastic (Hall *et al.* 2013), and undamaged vegetation were all found in the Tungurahua PDC deposits after the 2006 eruption showing not all parts of the flows were hot. On the other hand, charred wood at Tungurahua surrounding and within the 2006 PDC deposits indicates local temperatures as high as 300°C (Pollock *et al.* 2010). The major outcome of this study is that the Cotopaxi and Tungurahua clasts retain evidence of both hot and cold regions within the same PDC deposit.

## 5.2 Thermal heterogeneity of boiling-over pyroclastic density currents

Despite the large concentrations of juvenile clasts that were deposited at near-magmatic temperatures, lithic clasts in the deposits from Cotopaxi and Tungurahua show no evidence of reheating and are interpreted to have low emplacement temperatures. The matrix of the PDC deposits must have insulated the lithic clasts from the juvenile clasts, and the matrix must have cooled during transport by air entrainment. We hypothesize that air entrainment and cooling during transportation is especially important in boiling-over PDCs. This contradicts previous speculations on boiling-over eruptions, which assume that low fountaining produces little entrainment and promotes low cooling rates during flow (Freundt 1999). Limited entrainment of ambient air during the fountain phase may initially inhibit cooling of the PDC, but simulations by Clarke *et al.* (2002) and Dufek & Bergantz (2007) show a greater degree of air entrainment during flow than PDCs originating from a buoyant eruptive column.

### 5.3 Scoria-rich pyroclastic density currents

The deposits at Tungurahua and Cotopaxi do not contain significant amounts of pumice or dense blocky juvenile clasts and, therefore, cannot be classified as either an ignimbrite or a block and ash deposit (Branney and Kokelaar, 2002). Instead, they are constituted of scoria-bombs and large lithic clasts embedded in a coarse-ash and lapilli matrix and are similar to deposits observed at other arc volcanoes such as Aso and Arenal (e.g. Miyabuchi *et al.* 2006; Alvarado & Soto 2002; Cole *et al.* 2005; Mothes *et al.* 1998). We interpret the paleomagnetic data presented here to indicate that the cauliflower-textured scoria bombs are associated with thermally heterogenous gravity flows. The scoria bombs have a texture that is consistent with substantial air entrainment, namely a quenched outer rind, but an expanded interior, textures usually associated with ballistic fragments. We suggest scoria-rich PDCs are a common characteristic of thermally heterogenous boiling-over eruptions.

### 5.4 Model of thermal heterogeneity

The extent to which a lithic clast is heated after being incorporated into a hot flow of pyroclastic material consisting of gas, ash, and clasts can be readily estimated. We use the temperatures determined from the progressive thermal demagnetization of lithic clasts to model the temperature of the surrounding material at the time of deposition. We assume a spherical clast with a radius of 10 cm being heated by conduction from rim to core. The model tests the time needed to heat the clast at a particular depth to a given temperature (Fig. 14).

The temperature of a spherical lithic clast that is being heated conductively from the outside is governed by a heat conductivity equation (Carslaw & Jaeger 1959):

$$T_{(r,t)} = \frac{T_o - T_e}{2} \Omega_{(\varepsilon,\tau)} + T_e, \text{ where}$$

$$\Omega_{(\varepsilon,\tau)} \equiv \operatorname{erf} \frac{\varepsilon+1}{2\pi^{\frac{1}{2}}} - \operatorname{erf} \frac{\varepsilon-1}{2\pi^{\frac{1}{2}}} - 2 \frac{\tau^{\frac{1}{2}}}{\varepsilon\pi^{\frac{1}{2}}} \left( e^{-\frac{(\varepsilon-1)^2}{4\tau}} - e^{-\frac{(\varepsilon+1)^2}{4\tau}} \right),$$

where  $r$  is the distance from the center of the clast,  $t$  is time,  $T_o$  is clast temperature at  $t = 0$ ,  $T_e$  is the temperature of the medium,  $\varepsilon$  is the dimensionless distance from the center of the clast  $\equiv \frac{r}{a}$ ,  $\tau$  is the dimensionless Fourier number  $\equiv \frac{kt}{a^2}$ ,  $a$  is the radius of the clast, and  $k$  is the thermal diffusivity. We assume that the matrix of the deposit has a uniform temperature (i.e. a constant temperature boundary condition for the lithic clast's surroundings). This provides an extreme condition for heating

of the clasts (i.e. cooling of the matrix and removal of heat by convection of gas would result in cooler temperatures everywhere in space and time). This equation has been used to calculate cooling of a PDC deposit by entrainment of cold lithic clasts (Marti *et al.* 1991) as well as to demonstrate that the lithic clasts at Santorini were already at elevated temperatures before incorporation into the PDC, rather than being reheated by the PDC (Bardot 2000).

A clast achieves significant heating through the core when  $\tau = 1$ , which indicates a time scale between 7 and 11 hours for 90% heat exchange in a 10 cm diameter clast with porosities between 10% and 60%, and  $k$  values of 4.0 to  $2.5 \times 10^{-7} \text{ m}^2/\text{s}$  (Riehle *et al.* 1995). As the clast temperature adjusts to the volumetrically dominant matrix, the bulk deposit simultaneously cools through heat loss to the ground and atmosphere. Although cooling of the matrix will result in a diminished extent of heating of the lithic clasts, the temperature of the matrix will cool less than  $1^\circ\text{C}$  in 7 to 11 hours (Fig. 14). This can be demonstrated with the equation describing cooling of a sheet:

$$x = 0.5 \left( \operatorname{erf} \frac{z+1}{2\sqrt{\tau}} - \operatorname{erf} \frac{z-1}{2\sqrt{\tau}} \right) - 0.5 \left( \operatorname{erf} \frac{w+1}{2\sqrt{\tau}} - \operatorname{erf} \frac{w-1}{2\sqrt{\tau}} \right)$$

where  $z = 1/a$ ,  $w = 2-z$ , and  $a$  is the thickness of the sheet (Jaeger 1968).

For the few lithic clasts (Tu-10-01 and Tu-10-02) that reached temperatures sufficient to reset the previous remanence (210 to  $350^\circ\text{C}$  for Tu-10-01 and 550 to  $580^\circ\text{C}$  for Tu-10-02, as estimated by bulk susceptibility vs. temperature data seen in Fig. 7), our model indicates that the matrix temperature must be slightly higher ( $10\text{-}20^\circ\text{C}$ ) than the maximum temperature of a clast to heat a 10 cm lithic clast uniformly before the entire deposit cools.

The near-magmatic temperatures of the juvenile clasts must contribute little to the total thermal balance in the deposits, which contain cold lithic clasts embedded in a matrix of ash that also is at low temperatures. In the two deposits that do contain reheated lithic clasts (e.g. Tu-10-01 and Tu-10-02), the matrix must have been locally hot.

### 5.5 Importance of sampling lithic and juvenile clasts

Because temperatures range by over  $500^\circ\text{C}$  in Cotopaxi and Tungurahua PDC deposits over the scale of centimeters to meters, it would be misleading to assign a single temperature to a scoria-rich PDC or the deposits that it forms. The results presented here support the hypothesis that PDC deposits are exceedingly thermally heterogeneous at the time of deposition (e.g. Marti *et al.* 1991). Furthermore, the temperature differences between lithic and juvenile clasts and the matrix highlight the importance of air entrainment and cooling during flow. The paleomagnetic data reported here

indicate that the Cotopaxi and Tungurahua PDCs are a 'cold-matrix, hot-bomb' type of PDC, supporting the hypothesis that the current cooled by ingestion of large amounts of air during flow. In fact, the fine-grained material cooled to nearly ambient temperature before deposition, and few lithic fragments were heated to appreciable temperatures, even within their outermost centimeter. At the same time, juvenile clasts barely cooled and remained hot enough to deform after deposition. The proximity of cold lithic and hot juvenile clasts and the progressive thermal demagnetization results indicate local (<1 m scale) temperature variations of >500°C within the deposit. Emplacement temperatures estimated only from the paleomagnetic data from juvenile scoria bombs would have led to the interpretation of a 'hot PDC' (deposition >500°), whereas measurements of only lithic clasts would have indicated a 'cold PDC' or even a lahar. Consideration of both types of clasts permits more thorough documentation of the thermal history of pyroclastic density currents and characterization of boiling-over pyroclastic flows.

Out of 13 studies that report progressive thermal demagnetization data to estimate deposition temperatures, most have examined only lithic clasts (Bardot 2000, Cioni *et al.* 2004, Gernon *et al.* 2009, Lesti *et al.* 2011, McClelland *et al.* 2004, Paterson *et al.* 2010, Porreca *et al.* 2008). Two focus on juvenile material (Paquereau-Lebti *et al.* 2008; Saito *et al.* 2003), and one study does not specify the nature of the materials analyzed (Aramaki & Akimoto 1957). Only two studies of which we are aware since the work of Aramaki & Akimoto (1957) examined both juvenile material and lithic clasts (Mandeville *et al.* 1994; Sawada *et al.* 2000). Most clasts (pumice, obsidian, and lithic) from the 1883 Krakatau ignimbrite yielded emplacement temperatures of 475-550°C, indicating that all clasts were heated during flow or after deposition (Mandeville *et al.* 1994). These PDC deposits are large-volume siliceous ignimbrites. The wide range in inferred emplacement temperatures in the Taiheizan, Japan block-and-ash deposit (100-500°C for lithic clasts and 250-560°C for juvenile clasts) is not discussed and interpreted in detail (Sawada *et al.* 2000). The reported range in emplacement temperatures at Taiheizan may be an indication of thermal heterogeneity attributable to different extents of air entrainment over short length scales in block and ash flows.

## 5.6 Implications of boiling-over pyroclastic density currents for hazard assessment

This study demonstrates that boiling-over eruptions generated by fountaining or low column collapse from andesitic volcanoes produce density currents with low matrix temperatures and hot (magmatic temperature) juvenile clasts. By definition, boiling-over eruptions do not produce large-

scale buoyant plumes via buoyancy reversals, and the flows may begin with relatively high densities, because they do not entrain air during plume ascent or plunging from high altitude. They must engulf large volumes of air as they descend, however, which can aid transport of clasts (Dufek *et al.* 2009). Hazard mitigation requires accurate knowledge of the temperature of pyroclastic flows (e.g. Zanella *et al.* 2007). The presence of scoria bombs and unheated lithic clasts signify that thermal damage may not be widespread, but damage and injury from abrasion, force of collision, and suffocation remain dangerous. Likewise, the scoria clasts, which constitute a significant fraction of the deposits, are close to magmatic temperatures and present a thermal hazard.

## 6. Conclusions

Paleomagnetic estimates of emplacement temperatures of PDC deposits from the 1877 eruption at Cotopaxi and 2006 eruption at Tungurahua reveal a thermally heterogeneous mixture of lithic and juvenile clasts at the time of deposition. Cool lithic clasts were emplaced less than a meter away from hot juvenile clasts and are interpreted to imply a cool and insulating ashy matrix due to the extent of air entrainment during flow. Most lithic clasts from Tungurahua were never heated above  $\sim 90^{\circ}\text{C}$ , even in their outer rims, indicating they were deposited from currents that were well below magmatic temperatures at the time of emplacement. Two sample sites have lithic clasts that record elevated emplacement temperatures ( $>210^{\circ}\text{C}$  and  $>540^{\circ}\text{C}$ ), indicating deposition of hot material for a limited time or in isolated locations. Most Cotopaxi juvenile clasts, which have maximum blocking temperatures below about  $400^{\circ}\text{C}$  on the basis of bulk susceptibility vs. temperature measurements (Fig. 6), have emplacement temperatures that certainly are less than  $560$  to  $590^{\circ}\text{C}$ , and perhaps below  $400^{\circ}\text{C}$ , but lithic clasts were deposited cold, similar to most of the material at Tungurahua. Two Cotopaxi deposits contain juvenile and lithic clasts that both record cold ( $<90^{\circ}\text{C}$ ) emplacement temperatures and are interpreted as originating from hot PDC deposits that were then remobilized after cooling.

Future paleomagnetic studies of pyroclastic deposits should obtain data from both juvenile and lithic clasts in order to distinguish between cold and hot PDCs. Cauliflower-like scoria bombs are associated with thermally heterogeneous deposits at Cotopaxi and Tungurahua, suggesting that scoria-rich PDC deposits are good indicators of a boiling-over eruptive style that rapidly cools during flow.

## 7. Acknowledgements

This work was funded by NSF grant EAR-0838153 to D. Geist and 0838171 to K. Harpp. Numerous folks helped collect field observations and samples while in Ecuador including Madison Myers, Mary Benage, Nick Pollock, and Jesse Meyers. Additional financial support during the development of this study was provided by the University of Idaho. The authors also thank Lucia Gurioli, C. Mac Niocaill and Massimilian Porreca for helpful reviews and Michael Ort for editorial handling.

## References

Alvarado G., Soto G. (2002) Pyroclastic flow generated by crater-wall collapse and outpouring of the lava pool of Arenal Volcano, Costa Rica. *Bulletin of Volcanology* **63**:557-568.

Andrews G. D., Branney M. J. (2011) Emplacement and rheomorphic deformation of a large, lava-like rhyolitic ignimbrite: Grey's Landing, southern Idaho. *Geological Society of America Bulletin* **123**:725-743.

Aramaki S., Akimoto S. (1957) Temperature estimation of pyroclastic deposits by natural remanent magnetism. *American Journal of Science* **255**:619-627.

Banks N. G., Hoblitt R. P. (1996) *Direct Temperature Measurements of Deposits, Mount St. Helens, Washington, 1980-1981*. US Government Printing Office.

Bardot L. (2000) Emplacement temperature determinations of proximal pyroclastic deposits on Santorini, Greece, and their implications. *Bulletin of Volcanology* **61**:450-467.

Bardot L., McClelland E. (2000) The reliability of emplacement temperature estimates using palaeomagnetic methods: a case study from Santorini, Greece. *Geophysical Journal International* **143**:39-51.

Bardot L., Thomas R., McClelland E. (1996) Emplacement temperatures of pyroclastic deposits on Santorini deduced from palaeomagnetic measurements: constraints on eruption mechanisms. *Geological Society, London, Special Publications* **105**:345-357.

Belousov A., Behncke B., Belousova M. (2011) Generation of pyroclastic flows by explosive interaction of lava flows with ice/water-saturated substrate. *Journal of Volcanology and Geothermal Research* **202**:60-72.

- Branney M. J., Kokelaar P. (2002) *Pyroclastic density currents and the sedimentation of ignimbrites* Geological Society of London Memoirs **27**.
- Carrasco-Nunez G., Rose W. I. (1995) Eruption of a major Holocene pyroclastic flow at Citlaltepétl volcano (Pico de Orizaba), Mexico, 8.5-9.0 ka. *Journal of Volcanology and Geothermal Research* **69**:197-215.
- Carslaw H. S., Jaeger J.C. (1959) *Conduction of Heat in Solids 2nd Ed.* Oxford University Press.
- Cas R.A., Wright H.M., Folkes C.B., Lesti C., Porreca M., Giordano G., Viramonte J.G. (2011) The flow dynamics of an extremely large volume pyroclastic flow, the 2.08-Ma Cerro Galán Ignimbrite, NW Argentina, and comparison with other flow types. *Bulletin of volcanology*: **73**:1583-1609.
- Cioni R., Gurioli L., Lanza R., Zanella E. (2004) Temperatures of the A.D. 79 pyroclastic density current deposits (Vesuvius, Italy). *Journal of Geophysical Research* **109**:B02207, doi:10.1029/2002JB002251.
- Clarke A. B., Voight B., Neri A., Macedonio G. (2002) Transient dynamics of vulcanian explosions and column collapse. *Nature* **415**:897-901.
- Clement B. M., Connor C. B., Graper G. (1993) Paleomagnetic estimate of the emplacement temperature of the long-runout Nevado de Colima volcanic debris avalanche deposit, Mexico. *Earth and Planetary Science Letters* **120**:499-510.
- Cole P., Fernandez E., Duarte E., Duncan A. (2005) Explosive activity and generation mechanisms of pyroclastic flows at Arenal volcano, Costa Rica between 1987 and 2001. *Bulletin of Volcanology* **67**:695-716.
- Di Vito M. A., Zanella E., Gurioli L., Lanza R., Sulpizio R., Bishop J., Laforgia E. (2009) The Afragola settlement near Vesuvius, Italy: The destruction and abandonment of a Bronze Age village revealed by archaeology, volcanology and rock-magnetism. *Earth and Planetary Science Letters* **277**:408-421.
- Douillet G A., Pacheco D.A., Kueppers U., Letort J., Tsang-Hin-Sun È., Bustillos J., Hall M.L., Ramón P., Dingwell D. B. (2013a) Dune bedforms produced by dilute pyroclastic density currents from the August 2006 eruption of Tungurahua volcano, Ecuador. *Bulletin of Volcanology* **75**:1-20.
- Douillet G.A., Tsang-Hin-Sun E., Kueppers U., Letort J., Pacheco D.A., Goldstein F., Von Aulock F., et al. (2013b) Sedimentology and geomorphology of the deposits from the August 2006 pyroclastic density currents at Tungurahua volcano, Ecuador. *Bulletin of Volcanology* **75**:1-21.

Dufek J., Bergantz G. W., (2007) Dynamics and deposits generated by the Kos Plateau Tuff eruption; controls of basal particle loss on pyroclastic flow transport. *Geochemistry, Geophysics, Geosystems* **8**:Q12007.

Dufek J., Wexler J., Manga M. (2009) Transport capacity of pyroclastic density currents: Experiments and models of substrate-flow interaction. *Journal of Geophysical Research* **114**:B11203.

Freundt A. (1999) Formation of high-grade ignimbrites; II, A pyroclastic suspension current model with implications also for low-grade ignimbrites. *Bulletin of Volcanology* **60**:545-567.

Fujinawa A., Ban M., Ohba T., Kontani K., Miura K. (2008) Characterization of low-temperature pyroclastic surges that occurred in the northeastern Japan arc during the late 19th century. *Journal of Volcanology and Geothermal Research* **178**:113-130.

Fulop A. (2002) Transport and emplacement of ignimbrites and resedimented volcanoclastics from Gutai Mts., Eastern Carpathians, Romania. *Studia Universitatis Babeş-Bolyai. Geologia* **49**:65-73.

Garrison J. M., Davidson J. P., Hall M., Mothes P. (2011) Geochemistry and petrology of the most recent deposits from Cotopaxi Volcano, Northern Volcanic Zone, Ecuador. *Journal of Petrology* **52**:1641-1678.

Gernon T.M., Fontana G., Field M., Sparks R.S.J., Brown R.J., Mac Niocaill C. (2009) Pyroclastic flow deposits from a kimberlite eruption: the Orapa South Crater, Botswana. *Lithos* **112**:566-578.

Hall M., Mothes P. (2008) The rhyolitic–andesitic eruptive history of Cotopaxi volcano, Ecuador *Bulletin of Volcanology* **70**:675-702.

Hall L.M., Steele A. L., Mothes P. A., Ruiz M. C. (2013) Pyroclastic density currents (PDC) of the 16-17 august 2006 eruptions of Tungurahua volcano, Ecuador: geophysical registry and characteristics. *Journal of Volcanology and Geothermal Research* **265**:78-93.

Hoblitt R. P. (1986) Observations of the eruptions of July 22 and August 7, 1980, at Mount St. Helens, Washington. *U. S. Geological Survey Professional Paper* **1044-9612**:44.

Jaeger J.C. (1968) *Cooling and Solidification of Igenous Rocks*. Interscience New York.

Jones C. H. (2002) User-driven Integrated Software Lives: “PaleoMag” Paleomagnetism Analysis on the Macintosh *Computers and Geosciences* **28**:1145-1151.

Kelfoun K., Samaniego P., Palacios P., Barba D. (2009) Testing the suitability of frictional behaviour for pyroclastic flow simulation by comparison with a well-constrained eruption at Tungurahua volcano (Ecuador). *Bulletin of Volcanology* **71**:1057-1075.

Lesti C., Porreca M., Giordano G., Mattei M., Cas R., Wright H., Folkes C. B., Viramonte J. (2011) High-temperature emplacement of the Cerro Galán and Toconquis Group ignimbrites (Puna plateau, NW Argentina) determined by TRM analyses. *Bulletin of volcanology* **73**:1535-1565.

Mandeville C. W., Carey S, Sigurdsson H, King J. (1994) Paleomagnetic evidence for high-temperature emplacement of the 1883 subaqueous pyroclastic flows from Krakatau Volcano, Indonesia. *Journal of Geophysical Research* **99**:9487-9504.

Marti J., Diez-Gil J. L., Ortiz R. (1991) Conduction model for the thermal influence of lithic clasts in mixtures of hot gases and ejecta. *Journal of Geophysical Research* **96**: 21885.

McArthur A. N., Cas R. A. F., Orton G. J. (1998) Distribution and significance of crystalline, perlitic and vesicular textures in the Ordovician Garth Tuff (Wales). *Bulletin of Volcanology* **60**:260-285.

McClelland E. A., Druitt T. H. (1989) Palaeomagnetic estimates of emplacement temperatures of pyroclastic deposits on Santorini, Greece. *Bulletin of Volcanology* **51**:16-27.

McClelland E. A., Wilson C. J. N., Bardot L. (2004) Palaeotemperature determinations for the 1.8-ka Taupo ignimbrite, New Zealand, and implications for the emplacement history of a high-velocity pyroclastic flow. *Bulletin of Volcanology* **66**:492-513.

Miyabuchi Y., Watanabe K., Egawa Y. (2006) Bomb-rich basaltic pyroclastic flow deposit from Nakadake, Aso Volcano, southwestern Japan. *Journal of Volcanology and Geothermal Research* **155**:90-103.

Mothes P. A., Minard L. H., Janda R. J. (1998) The enormous Chillos Valley Lahar: an ash-flow-generated debris flow from Cotopaxi Volcano, Ecuador. *Bulletin of Volcanology* **59**:233-244.

Myers M. (2012) Melt Inclusions of Tungurahua *Masters Thesis*, University of Idaho.

Nogami K., Hirabayashi J., Ohba T., Ohsaka T., Yamamoto M., Akagi S., Ozawa T., Yoshida M. (2001) Temporal variations in the constituents of volcanic ash and adherent water-soluble components in the Unzen Fugendake eruption during 1990-1991. *Earth Planets and Space* **53**:723-730.

Paquereau-Lebti P., Fornari M., Roperch P., Thouret J. C., Macedo O. (2008) Paleomagnetism, magnetic fabric, and 40 Ar/39 Ar dating of Pliocene and Quaternary ignimbrites in the Arequipa area, southern Peru. *Bulletin of volcanology* **70**:977-997.

Paterson G. A., Roberts A. P., Mac Niocaill C., Muxworthy A. R., Gurioli L., Viramonté J. G., Navarro C., Weider S. (2010) Paleomagnetic determination of emplacement temperatures of pyroclastic deposits: an under-utilized tool. *Bulletin of volcanology* **72**:309-330.

Perrin M., Schnepf E., Shcherbakov V. (1998) Update of the paleointensity database. *EOS* **79**:198.

Pistolesi M., Rosi M., Cioni R., Cashman K. V., Rossotti A., Aguilera E. (2011) Physical volcanology of the post-twelfth-century activity at Cotopaxi volcano, Ecuador: Behavior of an andesitic central volcano. *Geological Society of America Bulletin* **123**:1193-1215.

Pistolesi M., Cioni R., Rosi M., Cashman K. V., Rossotti A., Aguilera E. (2013) Evidence for lahar-triggering mechanisms in complex stratigraphic sequences: the post-twelfth century eruptive activity of Cotopaxi Volcano, Ecuador. *Bulletin of volcanology* **75**: 1-18.

Pollock N., Harpp K. S., Geist D., Dufek J., Mothes P. A. (2010) Vegetation damage as a proxy for physical characteristics of PDCs. In *AGU Fall Meeting Abstracts* **1**:2337.

Porreca M., Mattei M., MacNiocaill C., Giordano G., McClelland E., Funicello R. (2008) Paleomagnetic evidence for low-temperature emplacement of the phreatomagmatic Peperino Albano ignimbrite (Colli Albani volcano, Central Italy). *Bulletin of Volcanology* **70**:877-893.

Riehle J. R., Miller T. F., Bailey R. A. (1995) Cooling, degassing and compaction of rhyolitic ash flow tuffs: a computational model. *Bulletin of Volcanology* **57**:319-336.

Roperch P., Chauvin A., Le Pennec J. L., Lara L. E. (2014) Paleomagnetic study of juvenile basaltic-andesite clasts from Andean pyroclastic density current deposits. *Physics of the Earth and Planetary Interiors* **227**: 20-29.

Saito T., Ishikawa N., Kamata H. (2003) Identification of magnetic minerals carrying NRM in pyroclastic-flow deposits. *Journal of Volcanology and Geothermal Research* **126**:127-142.

Samaniego P., Le Pennec J., Robin C., Hidalgo S. (2011) Petrological analysis of the pre-eruptive magmatic process prior to the 2006 explosive eruptions at Tungurahua Volcano (Ecuador). *Journal of Volcanology and Geothermal Research* **199**:69-84.

Sawada Y., Sampei Y., Hyodo M., Yagami T., Fukue M. (2000) Estimation of emplacement temperatures of pyroclastic flows using H/C ratios of carbonized wood. *Journal of Volcanology and Geothermal Research* **104**:1-20.

Scott A. C., Glasspool I. J. (2005) Charcoal reflectance as a proxy for the emplacement temperature of pyroclastic flow deposits. *Geology* **33**:589-592.

Scott A. C., Sparks R. S. J., Bull I. D., Knicker H., Evershed R. P. (2008) Temperature proxy data and their significance for the understanding of pyroclastic density currents. *Geology* **36**:143-146.

Shea T., Gurioli L., Houghton B. F., Cioni R., Cashman K. V. (2011) Column collapse and generation of pyroclastic density currents during the AD 79 eruption of Vesuvius: The role of pyroclast density. *Geology* **39**:695-698 doi:10.1130/G32092.1.

Smith G. A., Grubensky M. J., Geissman J. W. (1999) Nature and origin of cone-forming volcanic breccias in the Te Herenga Formation, Ruapehu, New Zealand. *Bulletin of Volcanology* **61**:64-82.

Soler M. M., Caffè P. J., Coira B. L., Onoe A. T., Kay S. M. (2007) Geology of the Vilama caldera: A new interpretation of a large-scale explosive event in the Central Andean plateau during the Upper Miocene. *Journal of Volcanology and Geothermal Research* **164**:27-53.

Sparks R. S. J., Barclay J., Calder E. S., Herd R. A., Komorowski J. C., Luckett R., Norton G. E., Ritchie L. J., Voight B., Woods A. W. (2002) Generation of a debris avalanche and violent pyroclastic density current on 26 December (Boxing Day) 1997 at Soufriere Hills Volcano, Montserrat. *Geological Society, London, Memoirs* **21**:409-434.

Steffke A. M., Fee D., Garces M., Harris A. (2010) Eruption chronologies, plume heights and eruption styles at Tungurahua Volcano: Integrating remote sensing techniques and infrasound. *Journal of Volcanology and Geothermal Research* **193**:143-160.

Suzuki Y. J., Koyaguchi T., Ogawa M., Hachisu I. (2005) A numerical study of turbulent mixing in eruption clouds using a three-dimensional fluid dynamics model. *Journal of Geophysical Research* **110**: B08201. doi:10.1029/2004JB003460.

Taylor G A. (1958) The 1951 eruption of Mount Lamington, Papua. *Bulletin - Australia, Bureau of Mineral Resources, Geology and Geophysics* **38**:117-117.

Wolf T. (1878) Memoria Sobre el Cotopaxi y su Ultima Erupción Acaecida el 26 de Junio de 1877. *Guayaquil, Imprenta de El Comercio* :48.

Zanella E., Gurioli L., Pareschi M. T., Lanza R. (2007) Influences of urban fabric on pyroclastic density currents at Pompeii (Italy): 2. Temperature of the deposits and hazard implications. *Journal of Geophysical Research* **112**:B05214.

Zanella E., Gurioli L., Lanza R., Sulpizio R., Bontempi, M. (2008) Deposition temperature of the AD 472 Pollena pyroclastic density current deposits, Somma-Vesuvius, Italy. *Bulletin of volcanology* **70**:1237-1248.

Zijderveld J.D.A. (1967) AC demagnetization of rocks: analysis of results. *Methods in paleomagnetism*: 254-286.

Zlotnicki J., Pozzi J. P., Boudon G., Moreau M. G. (1984) A new method for the determination of the setting temperature of pyroclastic deposits (example of guadeloupe: french west indies). *Journal of Volcanology and Geothermal Research* **21**:297-312.

Table 1. Estimated minimum emplacement temperatures. A single sample number consists of one lithic clast and one juvenile clast. Each clast was sectioned from rim to core into 2-4 cubes that were progressively demagnetized. The emplacement temperatures were estimated by inspection of progressive demagnetization during progressive heating steps.

	Sample Number	Clast Type	n	Emplacement Temperature (°C)	Flow Type
Tungurahua	Tu-10-01	Lithic	2	210	Warm PDC
		Juvenile	3	500	
	Tu-10-02	Lithic	2	540	Hot PDC
		Juvenile	3	530	
	Tu-10-03	Lithic	2	< 90	Cold PDC
		Juvenile	4	575	
	Tu-10-04	Lithic	2	< 90	Cold PDC
		Juvenile	2	560	
	Tu-10-05	Lithic	2	< 90	Cold PDC
		Juvenile	3	560	
Tu-10-06	Lithic	1	< 90	Cold PDC	
	Juvenile	3	560		
Tu-10-07	Lithic	2	< 90	Cold PDC	
	Juvenile	2	drifts		
Tu-10-08	Lithic	2	< 90	Cold PDC	
	Juvenile	3	> 590		
Tu-10-10	Lithic	2	< 90	Cold PDC	
	Juvenile	2	560		
Cotopaxi	Co-10-01	Lithic	2	< 90	Cold PDC
		Juvenile	3	590	
	Co-10-02	Lithic	2	< 90	Cold PDC
		Juvenile	2	590	
	Co-10-03	Lithic	3	< 90	Lahar
		Juvenile	2	< 90	
	Co-10-04	Lithic	1	< 90	Cold PDC
		Juvenile	3	590	
	Co-10-05	Lithic	3	< 90	Cold PDC
		Juvenile	3	590	
	Co-10-06	Lithic	2	< 90	Cold PDC
		Juvenile	3	575	
	Co-10-07	Lithic	3	< 90	Cold PDC
		Juvenile	2	560	
	Co-10-08	Lithic	2	< 90	Lahar
		Juvenile	2	< 90	
	Co-10-09	Lithic	2	< 90	Cold PDC
		Juvenile	2	590	

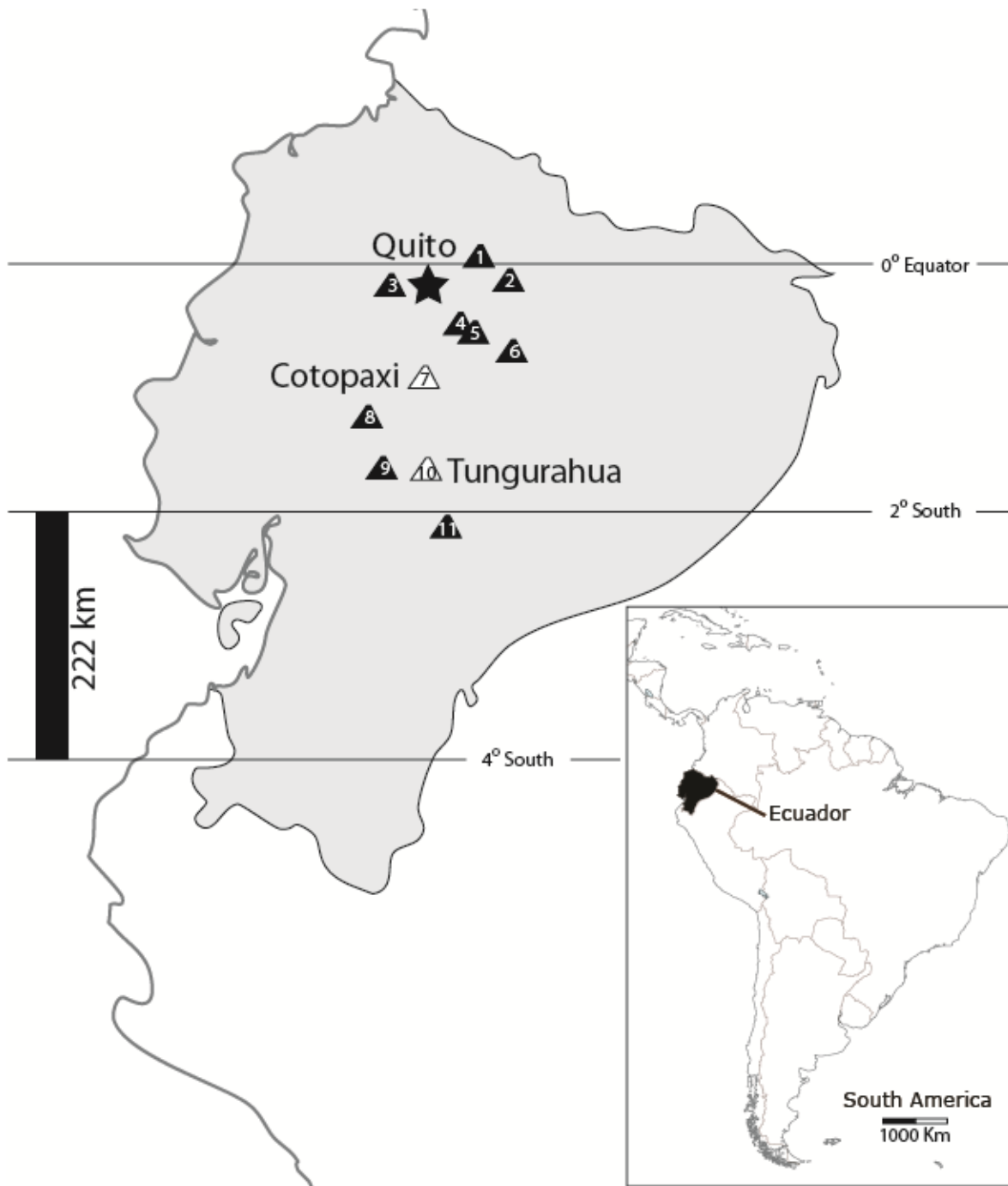


Figure 1. Location map of Tungurahua and Cotopaxi in Ecuador. The capital city of Quito is indicated by a star. Volcanoes represented by triangles from north to south are 1. Cayambe, 2. Reventador, 3. Guagua Pichincha, 4. Chacana, 5. Antisana, 6. Sumaco, 7. Cotopaxi, 8. Quilotoa, 9. Chimborazo, 10. Tungurahua, and 11. Sangay.

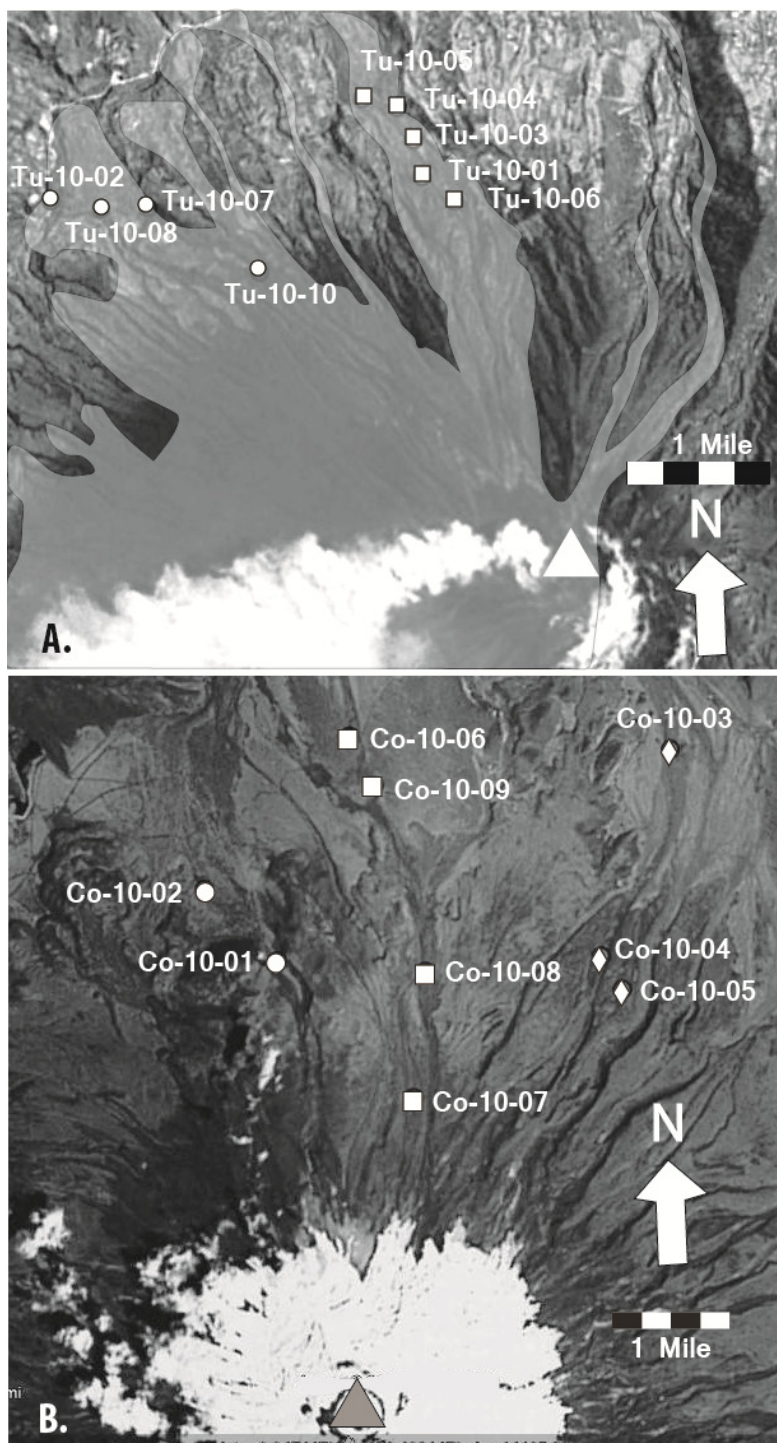


Figure 2. Map showing the extent of pyroclastic flows and sample locations. A) Tungurahua and B) Cotopaxi. Matching symbols represent samples collected from a single flow. The city of Baños is just off map A to the north.



Figure 3. Photo of Tungurahua emitting a boiling-over pyroclastic density current. Dec. 4<sup>th</sup>, 2010.

Image retrieved from

<http://i2.cdn.turner.com/cnn/2011/images/04/26/t1larg.tungurahua.volcano.afp.gi.jpg> accessed on 03-03-2014.

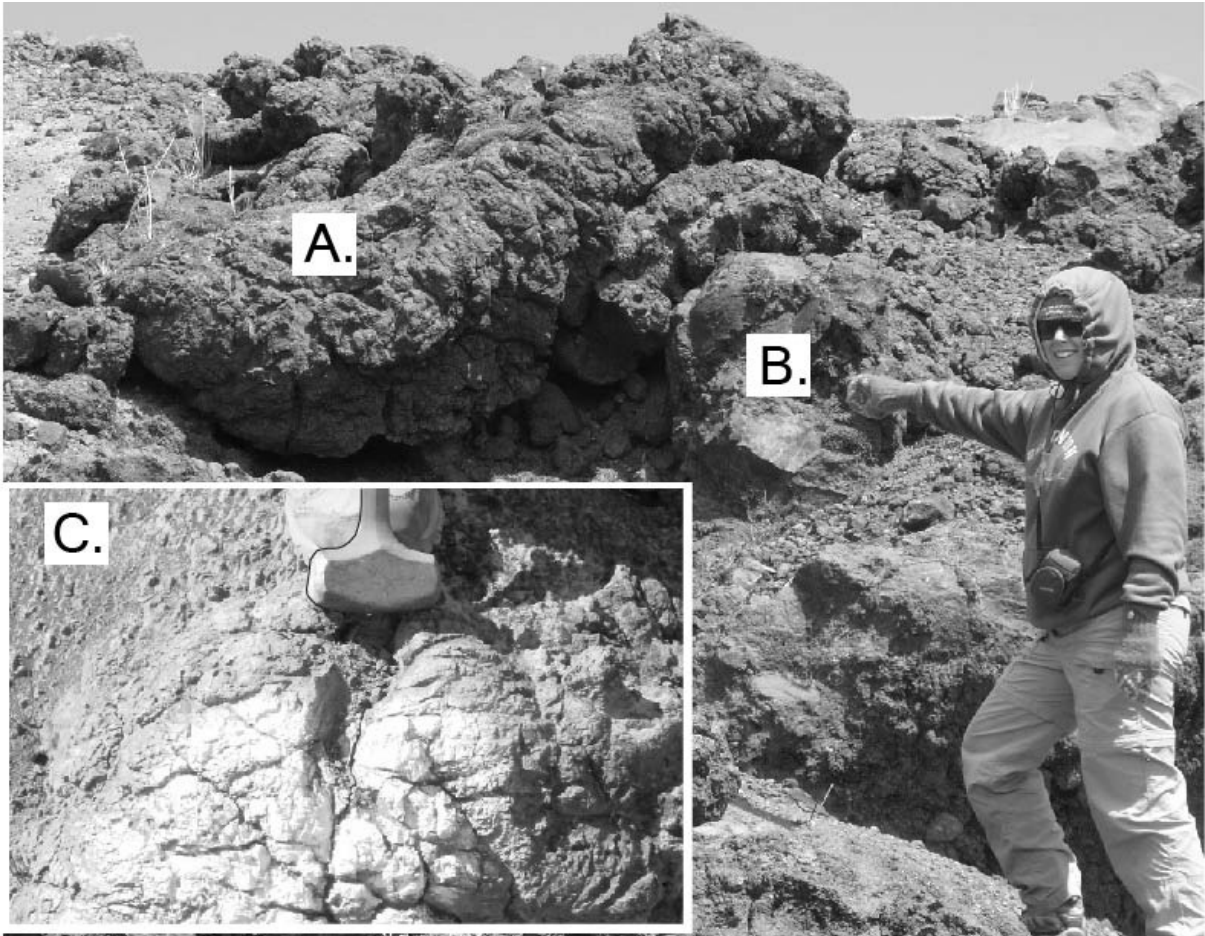


Figure 4. Field photographs showing juvenile bombs at both Cotopaxi and Tungurahua sagging under their own weight (A), drooping over other objects (B) and a cauliflower texture (C) that forms from the expansion of the hot inner part of the bomb while the cool outer crust cracks. These features all indicate a hot emplacement temperature for the bombs.



Figure 5. Pyroclastic flows are largely channelized in steep-sided quebradas (gullies) at both Tungurahua and Cotopaxi. Many of the preserved deposits are found at the base of the quebradas or where the PDCs jumped the steep walls. Cauliflower bombs can be seen dispersed along the bottom of the drainage below Cotopaxi.

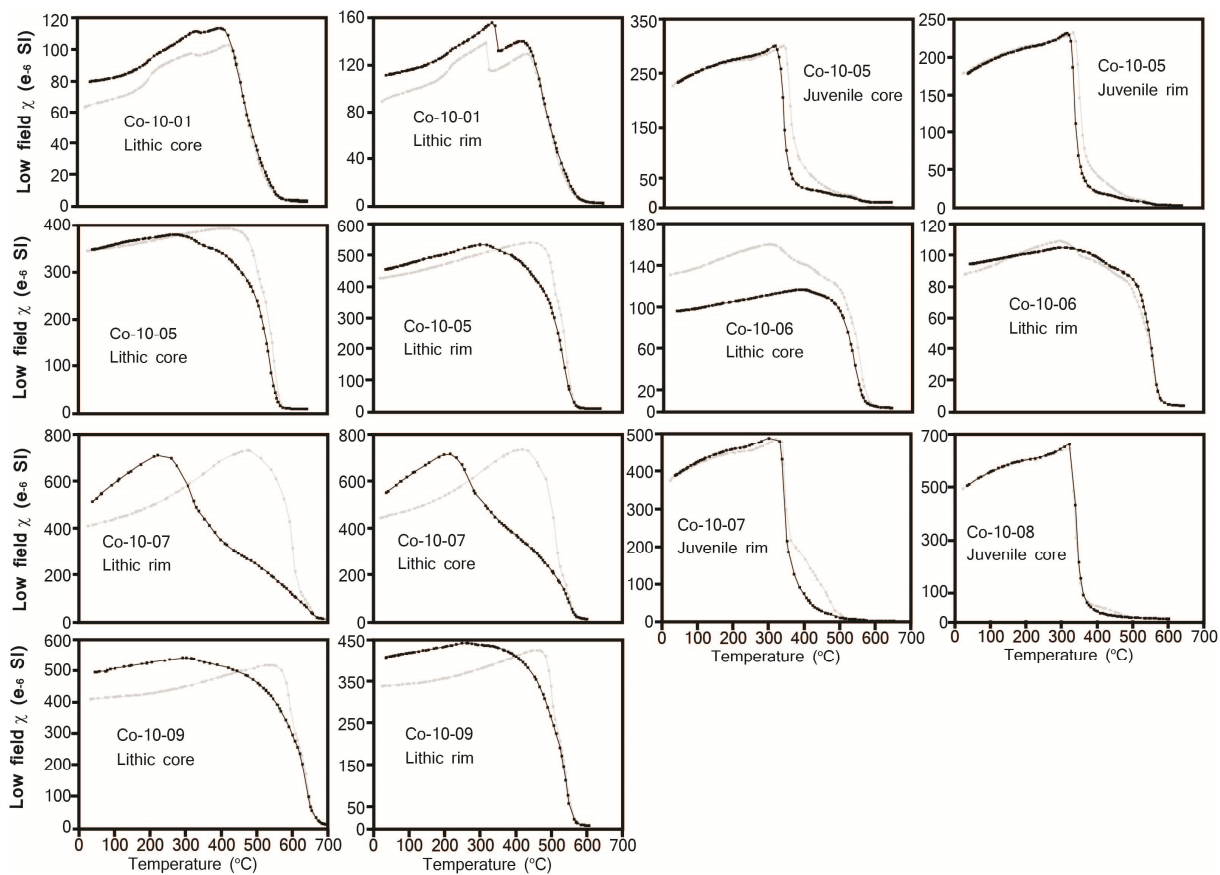


Figure 6. Plots of bulk, low field susceptibility from Cotopaxi as a function of temperature for powders of specimens from both juvenile and lithic clasts. Heating curves (grey line) and cooling curves (black line) obtained with specimen in an inert (Ar gas) atmosphere.

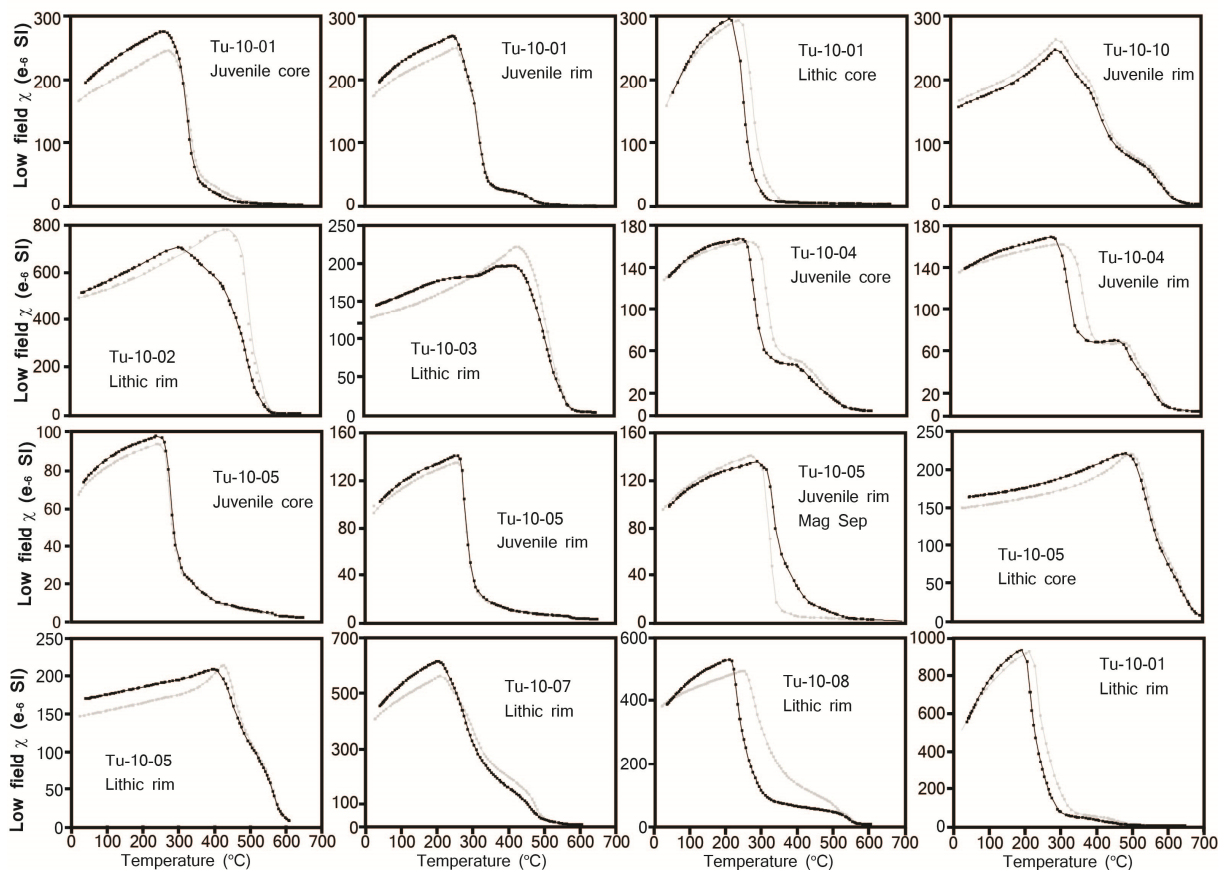


Figure 7. Plots of bulk, low field susceptibility from Tungurahua as a function of temperature for powders of specimens from both juvenile and lithic clasts from the Tungurahua deposits. Heating curves (grey line) and cooling curves (black line) obtained with specimen in an inert (Ar gas) atmosphere.

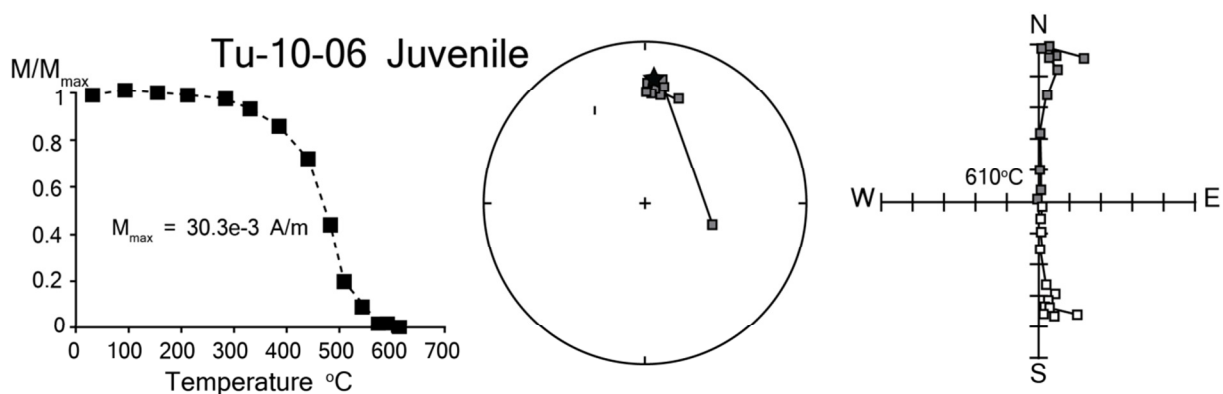


Figure 8. Orthogonal demagnetization diagram of typical juvenile clast (Zijderveld, 1967) showing response to progressive thermal demagnetization. Solid (open) symbols refer to projections on the horizontal (vertical) plane. Laboratory unblocking temperatures are distributed over the interval 90-610°C. At a laboratory unblocking temperature of 610°, the remanence remaining is a small fraction of the NRM and can be seen diverging from the rest of the temperature steps in the equal area plot in the center. The star indicates the present-day geomagnetic field direction. Gray squares are lower hemisphere projections, and open squares are upper hemisphere projections. The ellipses are the  $\alpha_{95}$  confidence interval about the estimated mean direction.

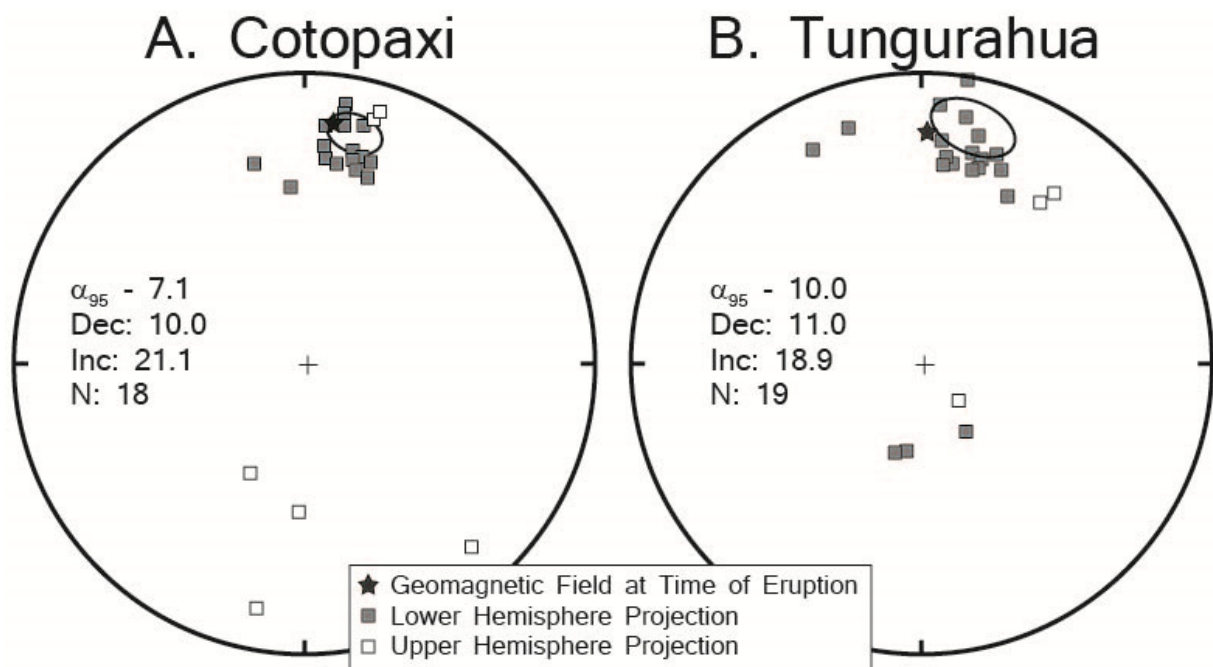


Figure 9. Equal area projection showing that juvenile clasts have paleomagnetic directions that closely match NRM even at high temperatures. Symbols on the equal area projection are the same as figure 8.

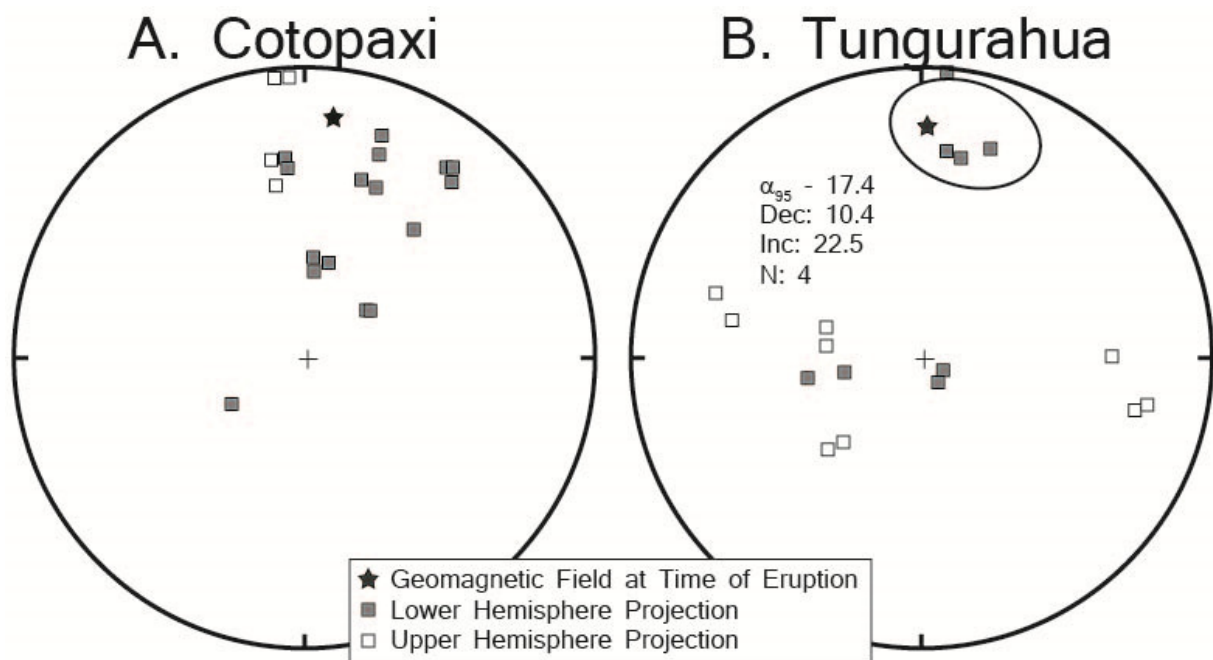


Figure 10. Equal area projections of lithic clasts. Magnetizations isolated in progressive thermal demagnetization of lithic clasts show greater scatter than juvenile clasts and do not align with the modern geomagnetic field. Most of these clasts are therefore interpreted to have been emplaced cold. Symbols are the same as figure 8.

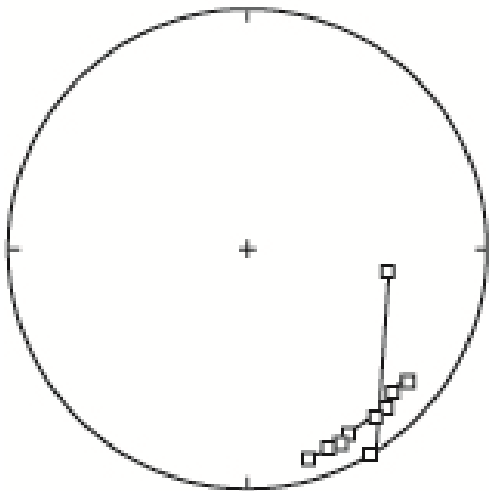
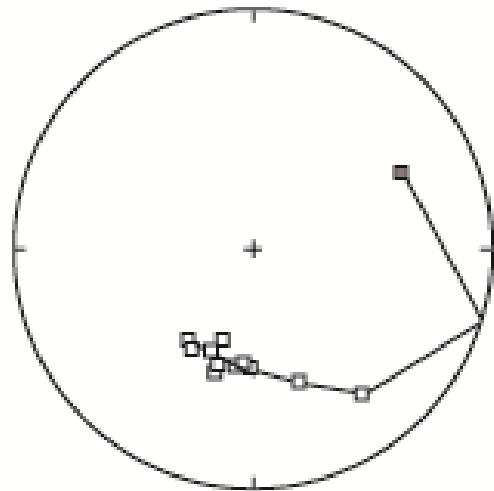
**Co-10-06 Juvenile****Co-10-03 Juvenile**

Figure 11. Orthogonal demagnetization diagrams showing two juvenile samples from Cotopaxi that do not align with NRM, indicating they were deposited after cooling, in what is interpreted as a lahar runout from a PDC deposit. Symbols are the same as figure 8.

## Tu-10-07 Juvenile

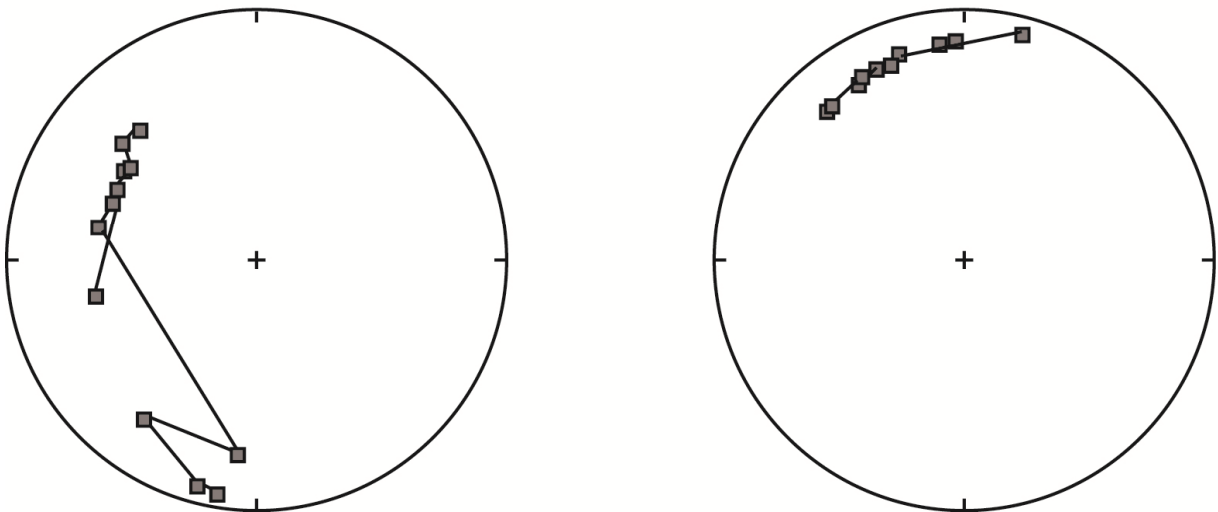


Figure 12. Orthogonal demagnetization diagram showing the response by a juvenile sample from Tu-10-07 at Tungurahua. The demagnetization data define a trajectory that suggests the single clast rotated in a single axis perpendicular to the slope as it cooled. This could be a manifestation of slow creep or slump in the deposit as the clast cooled. Symbols are the same as figure 8.

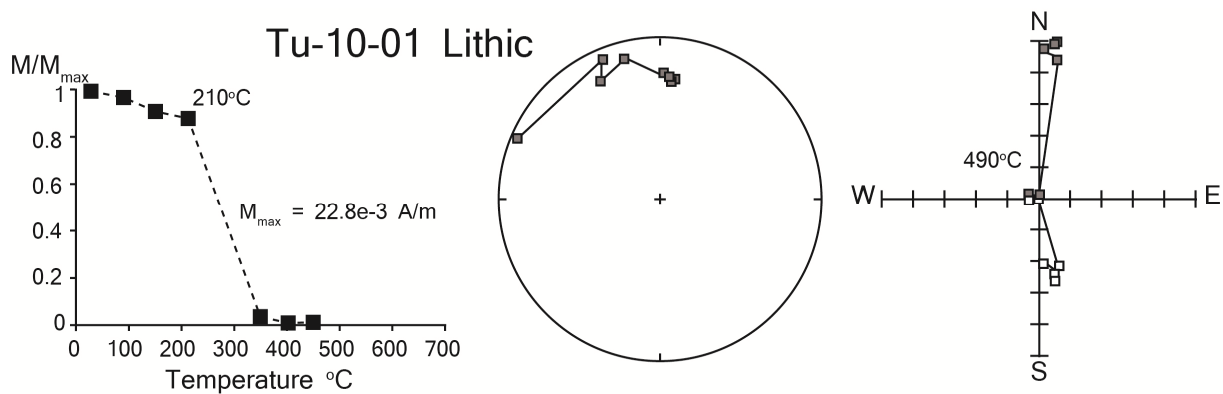


Figure 13. Orthogonal demagnetization illustrating that the abrupt change in declination at 210°C in a lithic clast from Tungurahua is characteristic of a clast that has been reset up to 210°C resulting in a cool emplacement temperature. Symbols are the same as figure 8.

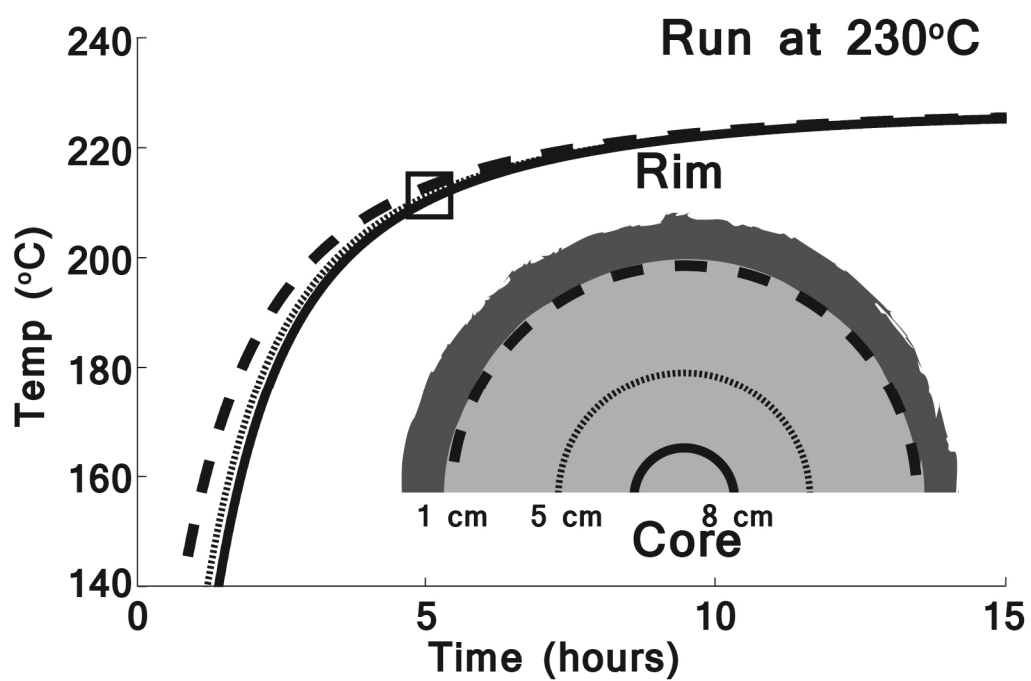


Figure 14. Example of a thermal model to constrain the temperature at different depths in a lithic clast deposited in a matrix with an initial temperature of 230°C. The three depths in this simulation are illustrated by different dotted, dashed, and solid lines on the graph.

## Chapter 4. The use of spatter deposits to constrain eruption conditions

### Abstract:

Spatter is a basaltic eruptive product that requires a narrow range of thermal conditions to form: hot enough to deform or agglutinate, but not so hot that clasts are remobilized as a clastogenic lava. High-temperature experiments conducted on basaltic scoria from Devil's Garden, Oregon have revealed the cooling and accumulation rates of several spatter features from this area. High-temperature oxidation and the presence of a thick glaze suggest slower cooling than the surface of lava flows, but the steep sides of spatter vents indicate cooling rates faster than the core of lava. Experiments show the eruption temperature of Devil's Garden basalt is  $\sim 1130^{\circ}\text{C}$ , which is far above the glass transition temperature of  $500\text{-}739^{\circ}\text{C}$ , depending on cooling rate and water content. The strength of the weld formed between clasts is shown to depend on cooling rate. Natural samples are compared to the experimental samples by measuring tensile strength. Natural weld strength yields estimates of cooling rates that range between  $2.5$  and  $48.4^{\circ}\text{C}/\text{min}$ , with the majority of the samples grouping between  $6.8\text{-}14.3^{\circ}\text{C}/\text{min}$ . These cooling rates and thermal models yield spatter accumulation rates of  $0.5\text{-}1.8\text{ m/h}$  in the Devil's Garden spatter deposits. We provide a general model for cooling and accumulation rates for spatter cones, ramparts, and hornitos, which allow estimation of the factors that control basaltic eruptive products.

### 1. Introduction

#### 1.1 Importance of understanding basaltic eruptions

Volcanic eruptions damage property, destroy life, and cause permanent changes to the landscape. The physical processes of eruptions control their impact. Consequently, these details are important to understand if accurate predictions of hazards are to be made (Sparks & Aspinall 2004). For basaltic eruptions, aerial emplacement of spatter constitutes one of the greatest hazards in the near-vent environment. One example is a spatter deposit at Izu volcano, which formed a weak layer below some fairly stable lava flows (Sumner 1998). This weak layer collapsed under the weight of the rock above and created a catastrophic cone collapse event.

In addition to predicting hazards, knowing the accumulation rates of spatter can provide information about the flux of magma, which is one of the most important characteristics of individual

eruptions. Currently, accumulations rates for unwitnessed eruptions are virtually impossible to quantify.

## 1.2 Spatter: A poorly quantified yet distinct field indicator

Spatter is defined as an accumulation of fluid pyroclasts that agglutinate on landing (Sumner et al. 2005). Agglutination occurs when temperatures are higher than the glass transition, which vary between 500°C and 739°C for basalt, depending on cooling rate (Giordano et al. 2005). Above this temperature, glass deforms and anneals, which can result in clasts interfusing. Thus, spatter provides the opportunity to quantify the conditions that are characteristic of basaltic eruptions, specifically accumulation and cooling rates (Sumner et al. 2005). Currently, only a qualitative relationship between spatter production, cooling rate, and accumulation rate is understood.

In the continuum between fluid lava flows and solidified bombs and cinder, spatter clasts are categorized qualitatively in a 1-5 scale (Sumner et al. 2005). Type 1 clasts are cold and brittle by the time they land (normal scoria). Type 2 clasts have brittle rims, but are still fluid on the inside. Type 3 clasts are fluid and agglutinate. Type 4 clasts are so fluid that they splash upon impact and coalesce to form a clastogenic flow. Type 5 clasts have a brittle core, yet a fluid rim, and are produced by the recycling of scoria in a fountain. We focus on accumulation and cooling rates that will produce agglutinated spatter deposits (Type 3 clasts) by combining field studies, experiments, and thermal models of spatter features at Devil's Garden, OR. This study aims to quantify the relationship between spatter production, cooling rate, and accumulation rate. As spatter is formed in a fairly narrow range of conditions, these methods are potentially applicable to eruption rates of more influential basaltic eruptions such as flood basalts and extraterrestrial volcanoes (Hauber et al. 2009, Fagents & Wilson 1994, Fagents 1996).

## 2. Field characteristics of spatter

### 2.1 Location Description

Devil's Garden is a basaltic lava flow field located ~40 km southeast of Bend, OR (Fig. 1; Keith et al. 1988, Chitwood 1994). The lava flow field of Devil's Garden is part of the High Lava Plains, a volcanic province thought by some to be linked to the Yellowstone hotspot (Jordan et al. 2004). The basaltic eruptive centers are oriented N-S, however, suggesting Basin and Range control (Christiansen et al. 2002). Devil's Garden is younger than the Holocene volcanic rocks on which it sits

(<15,000 years) but older than the eruption of Mt. Mazama ~7000 years ago (Sarna-Wojcicki et al. 1983). Chemical analyses of two samples, USGS sample name C159387 and C159389, are in Table 1 (Unpublished, <http://mrddata.usgs.gov/ngdb/rock/>).

## 2.2 Spatter Deposits at Devil's Garden

Three vents erupted spatter deposits within the Devil's Garden volcanic field. The main vent is located at the northeastern corner of the flow field, which is the source of ~ 1.2 km<sup>3</sup> of basalt. The vent complex comprises an elongated scoria cone that stretches north-south and is ~10 meters high. The outer flanks of the cone are made up of lapilli-sized scoria while the inner walls exposed numerous layers of 5-10 cm thick lava flows. They are thin and laterally continuous over a few meters, with spongy interiors, and are predominantly fused where they are in contact with one another. Most of the spatter at the main vent is located on the northwest corner of the cone. At this location, isolated clasts between 5 and 15 cm in diameter have porous cores and quenched rims. Twisted lobes, impressions of other clasts on the underside of blobs, fusiform shapes, and droopy forms indicate both pre- and post-depositional plastic strain. This spatter pile is between 1-2 meters thick and extends for about 3 meters along the top of the scoria cone. Most of these clasts preserve evidence of having been fluid when deposited, but they are not well agglutinated. According to the scheme of Sumner et al. (2005), most clasts are Type 2.

Another impressive spatter deposit at Devil's Garden is a vent complex 1.7 km south of the main vent called the Blowouts. Two cylindrical ramparts rise ~20 meters and share a border forming a figure '8' (Fig. 2). The southern structure is smaller and has a narrow breach ~10 meters wide to the north. The larger northern rampart has a breached western rim, and lava flows can be traced from a drained lava pond that sat in the southern vent. The interior walls of the blowouts are almost entirely made of spatter. A thin layer of scoria coats the outer flanks but is very sparse on the inside of the walls.

Spatter bombs are elongate and range in size from 5-50 cm along their longest axis, between 3-10 cm thick, and are Type 2-3 clasts (Fig. 3). Clasts have glassy rinds with small undeformed vesicles penetrating the glass. The cores of these bombs are highly vesicular and many vesicles are irregular from having coalesced with surrounding vesicles. Most deposits consist of contorted and spinose bombs, some of which are difficult to distinguish from surrounding bombs without exposing their interiors and identifying rinds. The porosity between clasts is small, likely from the high fluidity of the

clasts during after deposition. The spaces between bombs are irregular and aligned randomly, indicating no strong horizontal deviatoric stress.

The third location of spatter is a 150m long region of fissures that build up small spatter ramparts and hornitos between the main vent and the Blowouts. I collected samples from a textbook hornito on the west side of the road dubbed the Devil's Hot Tub. The hornito is ~3 m across and 1.5 m tall, with nearly vertical walls. Clasts are less contorted than those at the Blowouts or the main vent, likely due to the shorter flight path from the vent to deposition, but they are categorized as Type 3 clasts. The inside of the hornito is coated in drips (lava-cicles) that froze in place (Fig. 4).

### 2.3 Morphology of spatter deposits

One of the products of a spatter-producing eruption is an unusually steep-sided vent. Wood (1980) reported that the slopes of most scoria cones are consistently  $30^\circ$ , close to the angle of repose for scoria. Measurements of scoria cones and spatter features at El Malpais, Sunset Craters, Mono craters, Devil's Garden, and Craters of the Moon illustrate the difference between scoria and spatter constructs (Table 2). The scoria cones have height/width of 0.35-0.68 ( $20.8-34.4^\circ$ ), whereas spatter vents have height/width of 0.50-0.92 ( $26.5-42.6^\circ$ ; Fig. 5). The spatter vents have heights between 8 and 23 meters, and the scoria cones vary from 7 to 233 meters high. Features that are constructed by scoria and spatter (such as the main vent at Devil's Garden) have dimensions between the two populations. These systematic relationships suggest the slope and height of mafic vents can be used to characterize their constituent deposits.

### 2.4 Glaze on spatter

The rinds of surfaces close to the vent have a matte luster that distinctly lack the colorful and newly-cracked appearance of fresh basaltic glass (Fig. 6). These rinds are equivalent to the coatings on the inside of lava tubes, a feature called glaze (e.g. Gadanyi 2008. Allred & Allred 1998, Larson 1993). Many glazed rinds exhibit oxidation that is visible as a reddening of the glass. Some of the glaze is a muddy gray-green color or a dull black. The glazed rind on spatter clasts (as well as in lava tubes) is smoother with fewer vesicles or broken edges than the glassy crust of bombs, lava, and cinder. The luster is dull but reflective, and with magnification, the glaze appears as a layer of colored glass ~0.01-0.25 mm thick with a layer of more concentrated fe-oxides between the glass and the interior of the bomb (Fig. 7a). The oxide crystals are euhedral and 0.005 mm in size. Scanning

Electron Microscope (SEM) imaging shows that the surface of glaze has fewer and smaller vesicles than glassy rims on spatter bombs (Fig. 7b).

## 2.5 Textural descriptions of natural samples

Material 5mm from the glazed rim of spatter clasts at Devil's Garden were point counted and have crystallinities between 20-40% (Table 3). The crystals are plagioclase (10-20%), pyroxene (2-10%), and olivine (0-7%). There is a widely variable amount of Fe-oxide microlites in the different samples (1-13%). Olivine and pyroxene are strongly oxidized (black opaque replacement) in spatter samples H-12-02A, BO-12-01, and BO-12-02. Plagioclase crystals are euhedral and 0.4-0.9 mm long. The groundmass of the near-rims and cores in these spatter deposits contains little glass and numerous microlites of Fe-oxide and plagioclase.

## 3. Thermal experiments

### 3.1 Temperature range of spatter deposits

The liquidus temperature of erupting basalt can be used to constrain the maximum temperature of spatter. Similarly, the glass transition temperature signals the minimum temperature of agglutination. The glass transition temperature of basalt is between 500-739°C, depending on the cooling rate and water content (Giordano et al. 2005). Spatter deposits, therefore, must be deposited above this temperature. Several studies have documented the temperature of products of active basaltic eruptions. At Erta'Ale volcano, researchers applied corrections to thermal imaging and measured temperatures of fountaining spatter between 1140 and 1012°C with an average of 1084°C (Davies et al. 2011). Thermocouple measurements of fountaining lava at Surtsey yielded temperatures of 1100-1140°C (Einarsson 1966, Sigurgeirsson 1966). Estimates of eruption temperature at Devil's Garden are shown in Table 1.

### 3.2 Cooling rates of spatter

Slower cooling rates resulting in a lower glass transition temperature with cooling rates of 1-10°C/min producing glass transition temperatures of 500-739°C (Giordano et al. 2005). One method to estimate cooling rates in volcanic glasses is relaxational geospeedometry, which identifies the glass transition temperature by a sharp increase in heat capacity during heating. Cooling rate can then be calculated, as the transition temperature is defined as the point when the cooling rate

exceeds the rate at which the glass can deform. One study using this method found phonolite bombs from Tenerife with cooling rates as high as  $600^{\circ}\text{C}/\text{min}$  on the rim of bombs and as low as  $0.002^{\circ}\text{C}/\text{min}$  at their core (Wilding et al. 1996). Glassy rims on pillow basalts also cool very quickly at rates between  $6\text{-}4332^{\circ}\text{C}/\text{min}$  (e.g. Nichols et al. 2009, Bowles et al. 2005). Basaltic lava flows, analyzed by the same technique as well as measured directly by thermal infrared thermometers, exhibit cooling rates from  $8\text{-}140^{\circ}\text{C}/\text{min}$  for lava exposed to the atmosphere to as low as  $0.2\text{-}0.8^{\circ}\text{C}/\text{min}$  for lava transported in insulated channels (Gottsmann et al. 2004, Cashman et al. 1999). Spatter-fed phonolitic obsidian flows exhibit slower cooling rates between  $0.039$  and  $0.0028^{\circ}\text{C}/\text{min}$  (Gottsmann & Dingwell 2001). Cooling rates for basaltic spatter are expected to fall between the slow rates of obsidian and fast rates of the surface of lava flows.

### 3.3 Experimental methodology

To produce spatter with known cooling rates, we ran experiments on natural basalt clasts collected from Devil's Garden. Spatter scoria bombs  $\sim 25$  cm in diameter were collected and cut into  $\sim 2.5$  cm<sup>3</sup> cubes. Cut cubes were placed on a graphite plate and inserted into a preheated tube furnace. Two cubes of sample were placed on top of each other and placed in the furnace (Fig. 8). Samples were held at temperatures ranging from  $1000^{\circ}\text{C}$  to  $1140^{\circ}\text{C}$  for 20-120 minutes. After extraction from the tube furnace and a short (10-20 second) exposure to ambient temperatures during transfer, the scoria cubes were cooled in a muffle furnace programmed with specific cooling rates ranging from  $1\text{-}10^{\circ}\text{C}/\text{min}$  between the temperatures of  $1100$  and  $300^{\circ}\text{C}$ . After the sample was cooled to  $300^{\circ}\text{C}$ , the experiments were quenched by shutting off power to the muffle furnace.

### 3.4 Eruption temperature

Thirty-seven heating experiments were performed on lava cubes to assess their deformation under their own weight as a function of temperature. No deformation is observed below  $1120^{\circ}\text{C}$ . The lava became ductile at  $1125^{\circ}\text{C}$  and was highly fluid at  $1140^{\circ}\text{C}$ . Therefore, the simulation experiments were all initiated at  $1130^{\circ}\text{C}$ , which provided the ideal experimental condition to induce welding on a small scale over a short period of time.

### 3.5 Tensile strength measurements

Experiments which exhibited a weld plane between the two cubes were subject to tension tests to determine the strength of the weld. Hooks were epoxied with Devcon 3500 psi epoxy on to the ends of the cubes and allowed to cure overnight. A spring scale with a 22.7 kg capacity and a 0.2 kg sensitivity measured the force required to reach the failure point. The sample apparatus was placed under increasing tension until failure of the weld occurred. If failure did not occur at the weld, the experiment was discarded. Each trial was filmed to accurately capture the force exerted on each sample accurately. The freshly broken surfaces of the cubes were photographed and the surface area that had been in contact between the two cubes was measured.

### 3.6 Weld strength

Welding experiments included 12 pairs of cubes cooled at rates between 1 and  $10^{\circ}/\text{min}$  from 1130 to  $300^{\circ}\text{C}$  (Table 4). The tensile strength of the experimental welds is between 1.5 and  $15.3 \text{ N/mm}^2$ . Natural welded spatter clasts collected from Devil's Garden were measured to be between  $0.6\text{-}6.9 \text{ N/mm}^2$  (Table 4). Weld strength increases significantly with decreasing cooling rate (Fig. 9). We estimate the measurement uncertainty for the strength of the weld based on  $n = 5$  runs at a single cooling rate to be  $3.3 \text{ N/mm}^2 (1\sigma)$ . Three other sets of replicates were well within this range.

### 3.7 Cooling rate of deposit

On the basis of their weld strengths, four of the six natural samples have estimated cooling rates between  $6.8$  and  $14.3^{\circ}\text{C}/\text{min}$  (Fig. 9). The only other estimate of cooling rates of spatter deposits that we are aware of comes from phonolitic obsidian spatter, which is chemically and physically very different from basalt. Gottsmann & Dingwell (2001) used glass transition to estimate cooling rates of  $0.039$  and  $0.0028^{\circ}\text{C}/\text{min}$  for this obsidian, which are much lower than Devil's Garden basaltic spatter. We note that those cooling rates are unusually low, and may be due to the physical setting of the flows and the compositions of those magmas. The interior of basaltic lava flows also cool much more slowly than spatter deposits, supporting the hypothesis that spatter requires an intermediate cooling rate between fast cooling, which results in scoria, and slow cooling, which results in lava.

### 3.8 Failed experiments

Experiments were only included in this work if they did not fail at any point in the process. Several experiments are excluded from the analysis because they were dropped, melted completely, or there were difficulties maintaining the temperature during the entire duration of the experiment. In several excluded samples, epoxy dripped between the two cubes.

### 4. Accumulation rates in basaltic eruptions

In addition to cooling rate, accumulation rate is thought to be an important factor in the construction of spatter deposits (Sumner et al. 2005, Thomas & Sparks 1992). The stacking of hot clasts slows cooling of the deposit beneath. Accumulation rate measurements for spatter-producing eruptions are sparse. One rate from a spatter vent that transformed into a clastogenic flow was 10.2 m/h, indicating this might be near the transition between the clastogenic and spatter regimes (Sumner 1998). Scoria is produced instead of spatter due to an increase in cooling rate, however, accumulation rates of scoria cones have been reported and are included here. A compiled list of scoria cone observations give accumulation rates that vary from ~1-5 m/h (Riedel et al. 2003). These rates are quite large despite most scoria remaining unfused after deposition. Spatter accumulation rates should be less than clastogenic accumulation rates of 10.2 m/h.

#### 4.1 Cooling model of repeated deposition of spatter clasts

To calculate accumulation rate, implicit, finite-difference cooling model of Gerya (2010) was modified to simulate a vesiculated basaltic spatter clast deposited on cool ground. Cooling occurs from the top by natural convection with air and through the bottom by conduction into the ground. The model is one-dimensional, so heat transfer through the sides of the clast is neglected. The model periodically deposits a new clast on top of the growing pile. The thickness of clasts in the model is 5 cm, which was chosen to represent the thickness of a typical clast at Devil's Garden. These assumptions allow us to use the equation:

$$\frac{\delta^2 T}{\delta x^2} - \frac{1}{k} \frac{\delta T}{\delta t} = 0$$

where T is temperature, x is position, K is thermal diffusivity, and t is time. Additional values used for constants in the model are presented in Table 5. The equation was solved using a finite element method and starting with initial conditions  $T(t=0, x) = 20^\circ\text{C}$  for when x was less than the bottom of the

clast pile and greater than the top of the clast pile and  $T(t=0, x) = 1130^{\circ}\text{C}$  for the clast pile. Hot clasts are then added to the top of the pile after a designated time interval to study the effects of such a thermal perturbation on the deposit as a whole.

Modeled cooling rates of the bulk deposit between the temperatures of 1130 and 630°C range from 1.6 °C/min for 10 cm clasts being deposited every 100 seconds to 51 °C/min for 3 cm clasts deposited every 100 seconds (Fig. 10; Table 6). As expected, cooling rates correlate with accumulation rate, but the thickness of individual clasts has a stronger control on cooling rate than accumulation rate.

#### 4.2 Accumulation rate of Devil's Garden spatter deposits

Our thermal model allows us to calculate the accumulation rate for Devil's Garden based on the experimental cooling rate simulations, estimates of the initial temperature, and measurement of the size of the clasts in the field. This yields accumulation rates for spatter clasts (5 cm in thickness) of 0.5 to 1.8 m/h and cooling rates between 6.8 and 14.3 °C/sec (Fig. 11). The two outliers in the natural samples of 2.5 and 48.4 °C/min require different clast conditions. A cooling rate of 2.5 °C/min corresponds to 10 cm clasts accumulating at a rate of 0.2 m/h. To achieve a cooling rate of 48.4 °C/min, the model required an accumulation rate of 2.2 m/h of 3 cm clasts, suggesting the cooling rates will vary within a deposit depending on the size of the clasts since cooling time is proportional to the ratio of surface area to volume (rims cool quickly, cores cool slowly). Given that the majority of clasts measured at Devil's Garden are 5 cm thick, eruption conditions with accumulation rates of 0.5-1.8 m/h and cooling rates of 6.8-14.3 °C/min will produce spatter. Our model shows that it is necessary to accumulate several clasts quickly, and then allow them to cool as a unit to achieve cooling rates consistent with the spatter deposits, as determined by the strengths of their welds. Consequently, these rates are likely a maximum estimate of accumulation as the periodicity of spatter-producing eruptions results in bursts of deposition followed by less vigorous activity.

#### 4.3 Constraints on eruption of spatter

Accumulation rate and its influence on cooling rate of the deposit are thought to be the principal control on the deposition of a spatter deposit as opposed to scoria, lava, or clastogenic flow (Fig. 12; Sumner et al. 2005, Head & Wilson 1989). This study provides the first constraint on accumulation and cooling rates that will produce fluid, agglutinated clasts (Type 3, as defined by

Sumner et al. (2005)). Type 3 basaltic clasts likely require 0.5-1.8 m/h of 5 cm clasts, as well as cooling rates of 6.8-14.3 °C/min, although local differences in these figures can be three times these values. Consistently higher accumulation rates, however, would probably result in rheomorphism and clastogenic lava, whereas slower rates would produce unwelded bomb and scoria deposits. Heat loss to the atmosphere during transport can also affect these rates but is not thought to affect the Devil's Garden deposits much because the spatter cones and ramparts are within 10-50 m of the vent (e.g., Capaccioni & Cuccoli 2005). That the vast majority of the clasts are deformed indicate temperatures upon landing >1130°.

## 5. Conclusion

Basaltic spatter deposits consist of partly agglutinated clasts that can still be recognized in the deposit as individual clasts. They are deformed, indicating deposition in a semi-molten state, but they were not so hot that they remobilized as lava. We have been able to simulate the agglutination of spatter clasts experimentally by varying the cooling rate of hot basalt. Comparisons of the weld strength between natural and experimental samples allows for a calculated cooling rate of 6.8 to 14.3 °C/min (with two outliers of 2.5 and 48.4 °C/min) for a spatter rampart at Devil's Garden. A 1-D, finite difference model was created to solve the heat equation for a thickening spatter deposit numerically. Eruptive conditions that result in the cooling rates we estimated for Devil's Garden were modeled and resulted in maximum accumulation rates for 5 cm clasts between 0.5 and 1.8 m/h. Constrained accumulation and cooling conditions will allow for new interpretations of eruption rates of the numerous basaltic eruptions that produce spatter. Additionally, eruptions deposit spatter at accumulation rates above 10 m/h could be identified as a collapsing hazard and should be managed accordingly.

## References

- Allred, K., & Allred, C. (1998). Tubular lava stalactites and other related segregations. *Journal of Caves and Karst Studies*, 60, 131-140.
- Bowles, J., Gee, J. S., Kent, D. V., Bergmanis, E., & Sinton, J. (2005). Cooling rate effects on paleointensity estimates in submarine basaltic glass and implications for dating young flows. *Geochemistry, Geophysics, Geosystems*, 6(7).
- Capaccioni, B., & Cuccoli, F. (2005). Spatter and welded air fall deposits generated by fire-fountaining eruptions: Cooling of pyroclasts during transport and deposition. *Journal of Volcanology and Geothermal Research*, 145(3-4), 263-280.
- Cashman, K. V., Thornber, C., & Kauahikaua, J. P. (1999). Cooling and crystallization of lava in open channels, and the transition of Pahoehoe Lava to 'A'a. *Bulletin of Volcanology*, 61(5), 306-323.
- Chitwood L A, 1994. Inflated basaltic lava--examples of processes and landforms from central and southeast Oregon. *Oregon Geol*, 56: 11-21.
- Christiansen, R. L., Foulger, G. R., & Evans, J. R. (2002). Upper-mantle origin of the Yellowstone hotspot. *Geological Society of America Bulletin*, 114(10), 1245-1256.
- Davies, A. G., Keszthelyi, L., & McEwen, A. S. (2011). Estimating eruption temperature from thermal emission spectra of lava fountain activity in the Erta'Ale (Ethiopia) volcano lava lake: Implications for observing Io's volcanoes. *Geophysical Research Letters*, 38(21).
- Einarsson, T. (1966). Studies of temperature, viscosity, density and some types of materials produced in the Surtsey eruption. *Surtsey Res. Prog. Report*, 2, 163-179.
- Erickson, M.S., Hopkins, R.T., Fey, D.L., & King, H.D. (1989). Analytical results and sample locality map of rock samples from the Devil's Garden Lava Bed (OR-1-2), Squaw Ridge Lava Bed (OR-1-3), and Four Craters Lava Bed (OR-1-22) Wilderness Study Areas, Lake County, Oregon. USGS Open-File Report, 89-307, 1-10.
- Fagents, S. A. (1996). Emplacement Mechanisms of Volcanic Materials on Mars. In *Lunar and Planetary Institute Science Conference Abstracts*, 27, 349.
- Fagents, S. A., & Wilson, L. (1994). Theoretical Analysis of the Explosive Emplacement of Basaltic Magma in Lava Fountain Eruptions: Implications for Pyroclast Dispersal on Earth, Venus and Mars. In *Lunar and Planetary Institute Science Conference Abstracts*, 25, 361.
- Gadanyi, P. (2008), Formation and locations of lava stalactites and lava stalagmites in the Vildgermir

- lava tube (Iceland). *Carpathian Journal of Earth and Environmental Sciences*, 3(1), 65-73.
- Gerya, T. (2010). *Introduction to numerical geodynamic modelling*. Cambridge University Press.
- Giordano, D., Nichols, A., & Dingwell, D. (2005). Glass transition temperatures of natural hydrous melts: a relationship with shear viscosity and implications for the welding process. *Journal of Volcanology and Geothermal Research*, 142(1-2), 105-118.
- Gottsmann, J., & Dingwell, D. (2001). Cooling dynamics of spatter-fed phonolite obsidian flows on Tenerife, Canary Islands. *Journal of volcanology and geothermal research*, 105(4), 323-342.
- Gottsmann, J., Harris, A. J., & Dingwell, D. B. (2004). Thermal history of Hawaiian pahoehoe lava crusts at the glass transition: implications for flow rheology and emplacement. *Earth and Planetary Science Letters*, 228(3), 343-353.
- Harris, A. J., Carniel, R., & Jones, J. (2005). Identification of variable convective regimes at Erta Ale lava lake. *Journal of Volcanology and Geothermal Research*, 142(3), 207-223.
- Hauber, E., Bleacher, J., Gwinner, K., Williams, D., & Greeley, R. (2009). The topography and morphology of low shields and associated landforms of plains volcanism in the Tharsis region of Mars. *Journal of Volcanology and Geothermal Research*, 185(1), 69-95.
- Head, J. W., & Wilson, L. (1989). Basaltic pyroclastic eruptions: Influence of gas-release patterns and volume fluxes on fountain structure, and the formation of cinder cones, spatter cones, rootless flows, lava ponds and lava flows. *Journal of Volcanology and Geothermal Research*, 37(3-4), 261-271.
- Jordan, B. T., Grunder, A. L., Duncan, R. A., & Deino, A. L. (2004). Geochronology of age-progressive volcanism of the Oregon High Lava Plains: Implications for the plume interpretation of Yellowstone. *Journal of Geophysical Research: Solid Earth (1978–2012)*, 109(B10).
- Keith, W. J., King, H. D., Gettings, M. E., & Johnson, F. L. (1988). Mineral resources of the Devil's Garden Lava Bed, Squaw Ridge Lava Bed, and Four Craters Lava Bed Wilderness Study Areas, Lake County, Oregon. *U.S. Geological Survey Bulletin*, A1-A14.
- Keszthelyi, L. (1995). Measurements of the cooling at the base of pahoehoe flows. *Geophysical research letters*, 22(16), 2195-2198.
- Larson, C. V. (1993). *An illustrated glossary of lava tube features*. Larson, Charlie & Jo.
- Newhall, C. G., & Self, S. (1982). The Volcanic Explosivity Index (VEI) an estimate of explosive magnitude for historical volcanism. *Journal of Geophysical Research: Oceans (1978--2012)*, 87(C2), 1231-1238.

- Nichols, A., Potuzak, M., & Dingwell, D. (2009). Cooling rates of basaltic hyaloclastites and pillow lava glasses from the HSDP2 drill core. *Geochimica et Cosmochimica Acta*, 73(4), 1052-1066.
- Riedel, C., Ernst, G., & Riley, M. (2003). Controls on the growth and geometry of pyroclastic constructs. *Journal of Volcanology and Geothermal Research*, 127(1), 121-152.
- Robertson, E. C. (1988). *Thermal properties of rocks*. US Department of the Interior, Geological Survey.
- Robertson, E. C., & Peck, D. L. (1974). Thermal conductivity of vesicular basalt from Hawaii. *Journal of Geophysical Research*, 79(32), 4875-4888.
- Sarna-Wojcicki, A. M., Champion, D. E., & Davis, J. O. (1983). Holocene volcanism in the conterminous United States and the role of silicic volcanic ash layers in correlation of latest-Pleistocene and Holocene deposits. *Late Quaternary environments of the United States*, 2, 52-77.
- Sigurgeirsson, T. (1966). Geophysical measurements in Surtsey carried out during the year of 1965. *Surtsey Res. Progr. Rep*, 2, 181-185.
- Sparks, R. S. J., & Aspinall, W. P. (2004). Volcanic activity: frontiers and challenges in forecasting, prediction and risk assessment. *Geophysical Monograph Series*, 150, 359-373.
- Sumner, J. M. (1998). Formation of clastogenic lava flows during fissure eruption and scoria cone collapse: the 1986 eruption of Izu-Oshima Volcano, eastern Japan. *Bulletin of Volcanology*, 60, 195-212.
- Sumner, J., Blake, S., Matela, R., & Wolff, J. (2005). Spatter. *Journal of Volcanology and Geothermal Research*, 142(1-2), 49-65.
- Thomas, R. M. E., & Sparks, R. S. J. (1992). Cooling of tephra during fallout from eruption columns. *Bulletin of Volcanology*, 54(7), 542-553.
- Walker, G. P. (1973). Explosive volcanic eruptions—a new classification scheme. *Geologische Rundschau*, 62(2), 431-446.
- Wilding, M., Webb, S., Dingwell, D., Ablay, G., & Marti, J. (1996). Cooling rate variation in natural volcanic glasses from Tenerife, Canary Islands. *Contributions to mineralogy and petrology*, 125(2-3), 151-160.
- Wood, C. A. (1980). Morphometric analysis of cinder cone degradation. *Journal of Volcanology and Geothermal Research*, 8(2), 137-160.

Table 1. Chemical analyses of Devil's Garden lava. From USGS database.

wt. %	Sample	
	C159387	C159389
SiO <sub>2</sub>	47.7	49.3
TiO <sub>2</sub>	1.61	1.48
Al <sub>2</sub> O <sub>3</sub>	16.6	16.7
Fe <sub>2</sub> O <sub>3</sub>	10.7	10.5
MgO	9.19	8.83
CaO	9.78	9.43
Na <sub>2</sub> O	2.97	2.95
K <sub>2</sub> O	0.58	0.6
P <sub>2</sub> O <sub>5</sub>	0.41	0.42

Table 2. Height and width comparisons between spatter vents and scoria cones.

Location	Cone Type	Slope	Cone Height (m)
El Malpais	Cinder	0.68	61
	Cinder	0.55	79
	Cinder	0.62	27
	Cinder	0.50	42
	Cinder	0.59	98
	Cinder	0.59	58
Sunset Crater	Cinder	0.54	98
	Cinder	0.43	69
	Cinder	0.35	172
	Cinder	0.39	233
	Cinder	0.53	137
Mono Craters	Cinder	0.54	156
	Cinder	0.52	142
	Cinder	0.47	33
	Cinder	0.46	41
	Cinder	0.55	118
	Cinder	0.42	134
	Cinder	0.39	63
	Cinder	0.14	23
Devil's Garden	Spatter	0.84	13
	Spatter	0.74	11
	Spatter	0.50	12
	Spatter	0.60	17
	Spatter	0.82	23
	Spatter	0.92	15
	Spatter	0.70	12
	Spatter	0.64	18
	Spatter	0.63	8
	Combination	0.52	9
	Combination	0.75	15
	Combination	0.86	9

Table 3. Modal mineralogy of spatter clasts from Devil's Garden.

Sample	Groundmass	Feldspar		Pyroxene		Olivine		Oxide
		Mode	Size (mm)	Mode	Size (mm)	Mode	Size (mm)	Mode
H-12-01A	65	10	0.6	10	0.4	7	0.4	8
H-12-01B	65	15	0.9	10	0.3	5	0.7	5
H-12-01C	65	10	0.4	10	0.3	5	0.4	10
H-12-02A	70	15	0.5	4	0.4	1	0.7	10
H-12-02B	70	15	0.5	4	0.5	1	0.3	10
H-12-02C	70	15	0.5	4	0.3	1	0.3	10
BO-12-01	60	20	0.5	10	0.4	4	0.4	6
BO-12-02	80	10	0.5	5	0.3	4	0.4	1
BO-12-03A	69	16	0.7	8	0.4	2	0.4	5
BO-12-03B	80	10	0.7	5	0.5	4	0.6	1
BO-12-03C	80	10	0.6	5	0.4	4	1	1

Table 4. Experimental and natural cooling rates of spatter.

Sample Name	Sample Type	Failure Point (N)	Contact Surface Area (mm <sup>2</sup> )	N/mm <sup>2</sup>	Cooling Rate (°C/min)
H2F-10B	Experiment	31.1	2.0	15.5	<sup>a</sup> 1
H5A-1A	Experiment	22.2	1.5	14.9	<sup>a</sup> 1
H2F-8	Experiment	66.7	15.1	4.4	<sup>a</sup> 2
H2F-9	Experiment	40.0	9.9	4.0	<sup>a</sup> 2
H5A-3A	Experiment	31.1	2.8	11.3	<sup>a</sup> 2
H1A4	Experiment	4.4	0.4	10.3	<sup>a</sup> 2
H1A3	Experiment	6.7	0.7	9.0	<sup>a</sup> 2
H5A-4A	Experiment	40.0	3.8	10.6	<sup>a</sup> 3
H1A2	Experiment	20.0	1.8	11.3	<sup>a</sup> 3
H2D-25	Experiment	8.9	2.9	3.1	<sup>a</sup> 5
H2E-1	Experiment	149.0	55.0	2.7	<sup>a</sup> 10
H2E-3	Experiment	16.0	11.0	1.5	<sup>a</sup> 10
H2-N2	Natural	40.0	5.8	6.9	<sup>b</sup> 2.5
H1-N4	Natural	62.3	20.8	3.0	<sup>b</sup> 6.8
H1-N5	Natural	26.7	9.3	2.9	<sup>b</sup> 7.2
H5-N6	Natural	57.8	25.0	2.3	<sup>b</sup> 9.2
H2-N1	Natural	37.8	23.7	1.6	<sup>b</sup> 14.3
H1-N1	Natural	24.5	43.0	0.6	<sup>b</sup> 48.4

<sup>a</sup> Monitored by thermocouple

<sup>b</sup> Calculated from experiments

Table 5. Thermal constants used in model.

Symbol	Parameter	Value	Units	Source
k	Thermal Conductivity	1	$\text{W m}^{-1} \text{K}^{-1}$	Robertson & Peck 1974
cp	Specific Heat	1490	$\text{J kg}^{-1} \text{K}^{-1}$	Robertson 1988
rho	Density	1300	$\text{kg m}^3$	This study
h	Heat Transfer Coefficient	8	$\text{J m}^{-3}$	Harris et al. 2005

Table 6. Cooling rates for modeled accumulation rates.

$d_{clasts}$	$d_{clast}$ (m)	$d_{deposit}$ (m)	$t_{clast}$ (sec)	$t_{next}$ (sec)	Cooling Rate (°C/min)	Accumulation (m/h)
1	0.05	0.05	-	-	<b>125.0</b>	-
1	0.1	0.1	-	-	<b>31.0</b>	-
2	0.03	0.06	25	-	<b>45.9</b>	<b>4.3</b>
2	0.03	0.06	50	-	<b>48.1</b>	<b>2.2</b>
2	0.03	0.06	100	-	<b>51.8</b>	<b>1.1</b>
2	0.05	0.1	100	-	<b>14.3</b>	<b>1.8</b>
2	0.05	0.1	250	-	<b>15.2</b>	<b>0.7</b>
2	0.1	0.2	100	-	<b>3.4</b>	<b>3.6</b>
2	0.1	0.2	250	-	<b>3.5</b>	<b>1.4</b>
2	0.1	0.2	500	-	<b>3.8</b>	<b>0.7</b>
2	0.1	0.2	750	-	<b>3.7</b>	<b>0.5</b>
2	0.1	0.2	1000	-	<b>3.8</b>	<b>0.4</b>
2	0.1	0.2	1000	-	<b>3.8</b>	<b>0.4</b>
2	0.1	0.2	2000	-	<b>4.1</b>	<b>0.2</b>
3	0.03	0.09	5	5	<b>18.9</b>	<b>21.6</b>
3	0.03	0.09	10	10	<b>19.5</b>	<b>10.8</b>
3	0.03	0.09	16	16	<b>19.9</b>	<b>6.8</b>
3	0.03	0.09	25	25	<b>20.6</b>	<b>4.3</b>
3	0.03	0.09	50	50	<b>22.8</b>	<b>2.2</b>
3	0.05	0.15	50	50	<b>6.4</b>	<b>3.6</b>
3	0.05	0.15	100	100	<b>6.7</b>	<b>1.8</b>
3	0.05	0.15	250	250	<b>7.9</b>	<b>0.7</b>
3	0.05	0.15	500	500	<b>11.0</b>	<b>0.4</b>
3	0.1	0.3	100	250	<b>1.5</b>	<b>1.8</b>
3	0.1	0.3	100	100	<b>1.5</b>	<b>3.6</b>
3	0.1	0.3	250	250	<b>1.6</b>	<b>1.4</b>
3	0.1	0.3	250	100	<b>1.6</b>	<b>2.4</b>
3	0.1	0.3	500	500	<b>1.7</b>	<b>0.7</b>
3	0.1	0.3	500	100	<b>1.6</b>	<b>1.5</b>
3	0.1	0.3	750	750	<b>1.8</b>	<b>0.5</b>
3	0.1	0.3	750	100	<b>1.7</b>	<b>1.1</b>
3	0.1	0.3	1000	3000	<b>2.5</b>	<b>0.2</b>
3	0.1	0.3	1000	1000	<b>1.9</b>	<b>0.4</b>
3	0.1	0.3	1000	100	<b>1.8</b>	<b>0.9</b>
3	0.1	0.3	3000	3000	<b>4.3</b>	<b>0.1</b>
4	0.03	0.12	25	25	<b>12.7</b>	<b>4.3</b>
4	0.04	0.16	25	25	<b>7.3</b>	<b>5.8</b>
4	0.04	0.16	100	350	<b>12.4</b>	<b>0.5</b>
4	0.05	0.2	25	25	<b>3.1</b>	<b>7.2</b>
4	0.05	0.2	37	37	<b>3.3</b>	<b>4.9</b>
4	0.05	0.2	50	100	<b>4.1</b>	<b>2.1</b>
4	0.05	0.2	50	100	<b>4.6</b>	<b>2.1</b>
4	0.05	0.2	50	50	<b>4.5</b>	<b>3.6</b>
4	0.05	0.2	100	350	<b>5.4</b>	<b>0.6</b>
4	0.05	0.2	100	100	<b>4.7</b>	<b>1.8</b>
4	0.05	0.2	250	250	<b>5.4</b>	<b>0.7</b>
4	0.05	0.2	350	350	<b>6.1</b>	<b>0.5</b>
4	0.05	0.2	400	400	<b>6.7</b>	<b>0.5</b>
4	0.05	0.2	500	500	<b>10.5</b>	<b>0.4</b>
5	0.03	0.15	50	50	<b>13.3</b>	<b>2.2</b>

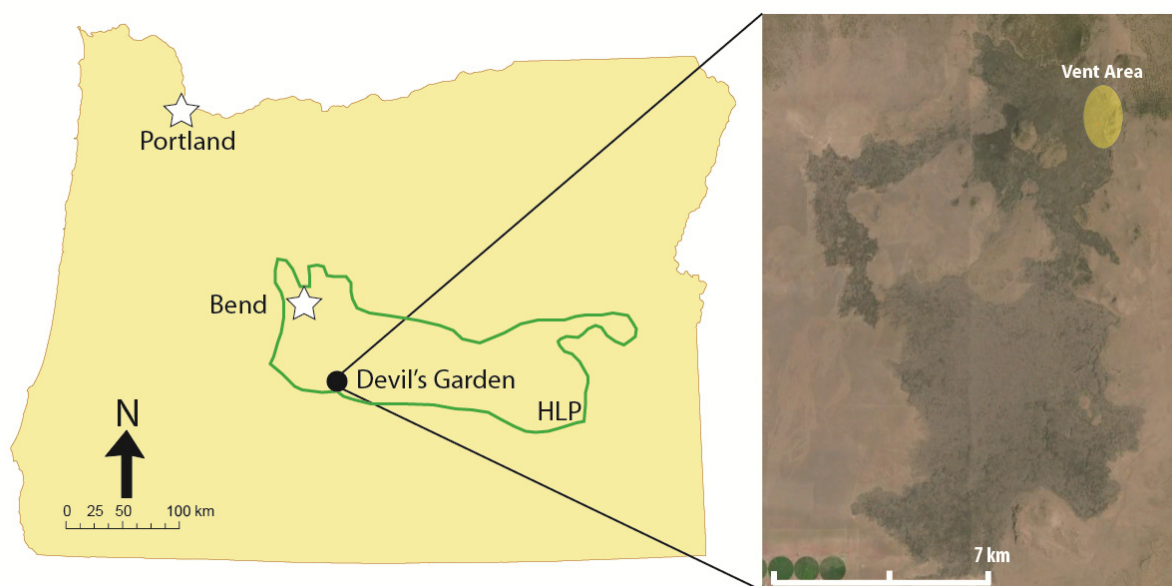


Figure 1. Location map of Devil's Garden Volcanic Field. The lava field is located about 80 km SE of Bend, OR. The green outlines the High Lava Plains (HPL). In the blow-up on the right, the region shaded yellow is where the three spatter localities are found.

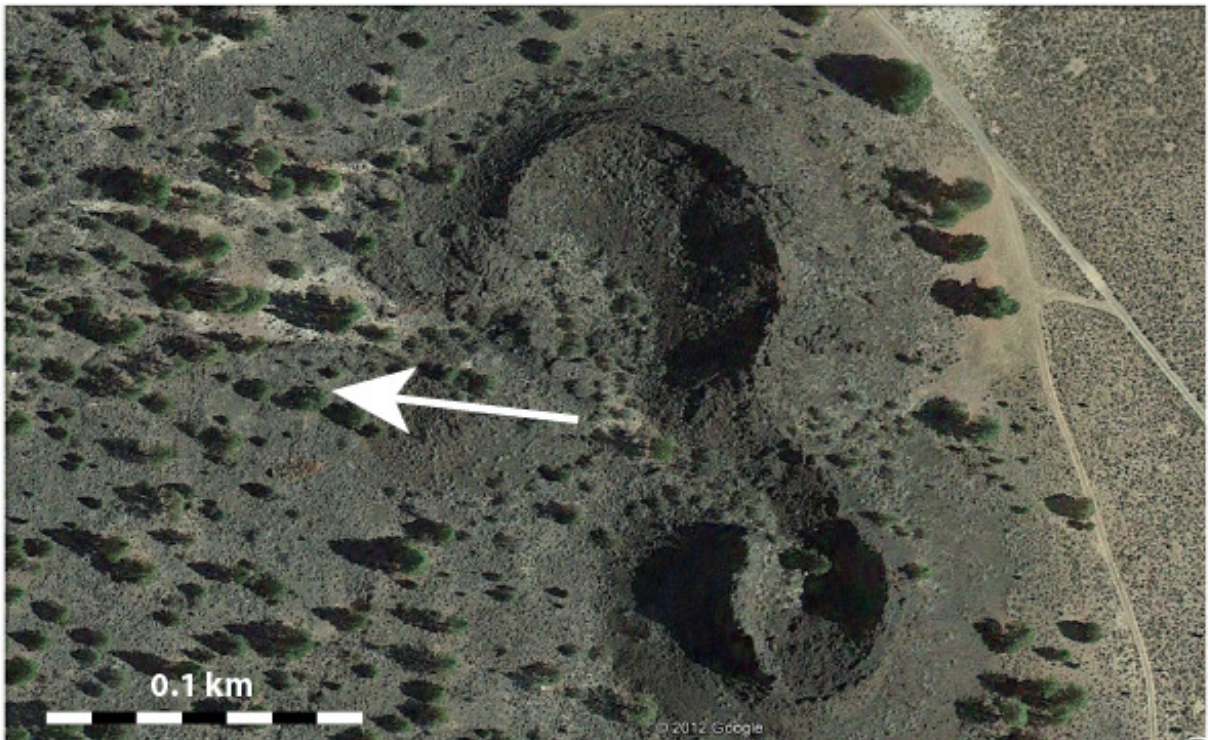


Figure 2. Aerial image of the Blowouts, Devil's Garden. This Google Earth image shows the orientation of these secondary vents, which produced small lava flows out to the west, as indicated by the white arrow.



Figure 3. Photo of cross-section of spatter pile at the Blowouts. Clasts can be hard to distinguish from one another without a view of the vesiculated core because they are so contorted and fused together.



Figure 4. Drips on the inside of Devil's Hot tub. These surfaces cooled slowly allowing the glaze to coat the droplets.

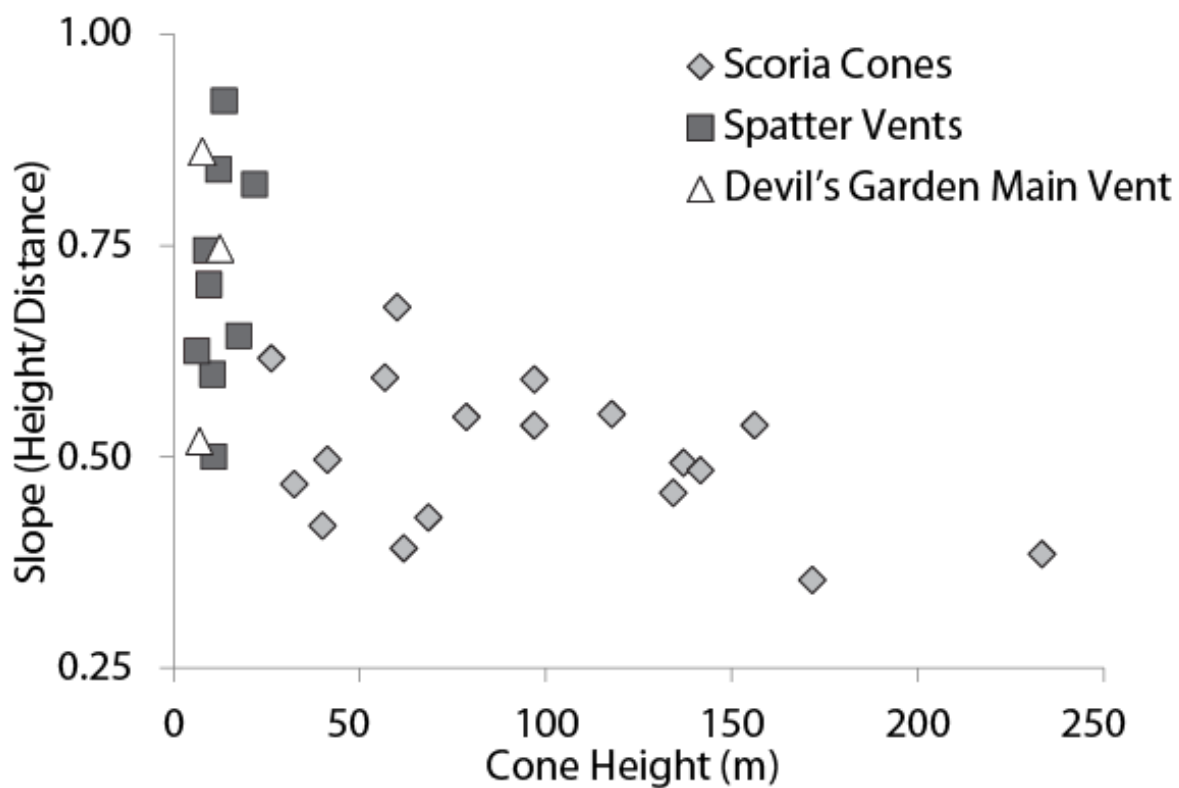


Figure 5. Slopes of scoria cones and spatter vents. Spatter vents (dark grey squares) have much higher slopes and also tend to be smaller than scoria cones (light grey diamonds). The white triangles are measurements taken from the main vent at Devil's Garden, which is constituted of both scoria and spatter.



Figure 6. Photo of two examples of glaze at Devil's Garden. Glaze is a thick, uncracked glassy rind that appears thick and uncracked, and is found in areas that were protected from air during and shortly after eruption, such as in caves or on the inside of the steep walls of the cone. It is likely a texture that forms from slow cooling that allows the glass to anneal.

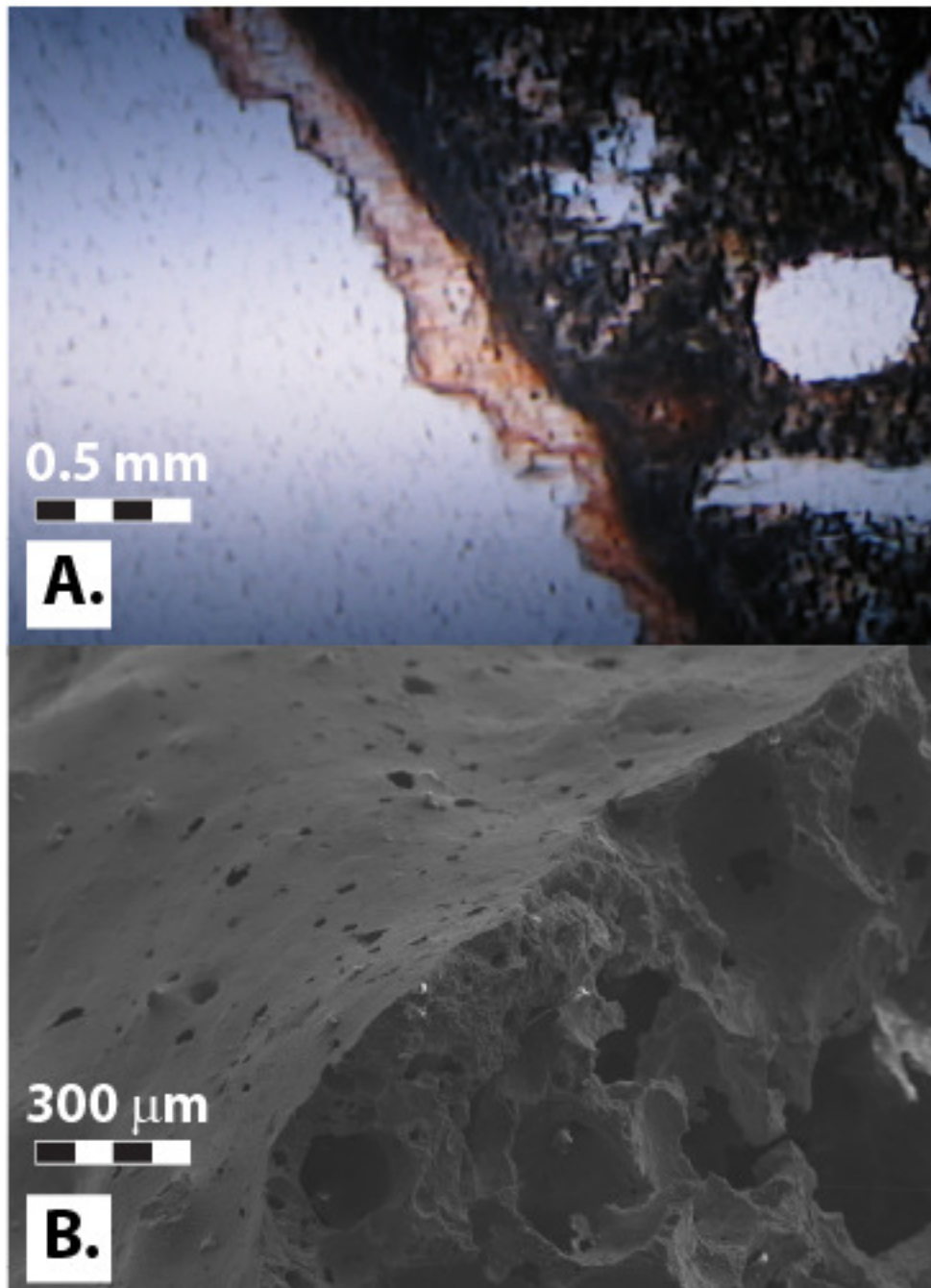


Figure 7. Photomicrograph (A) and SEM image (B) of glaze from Devil's Garden. Glaze is a rim of colored glass that can be hundreds of microns thick. Note concentration of oxide crystals line the inside of the glassy rim in A. In B., the highly vesiculated interior is truncated by the smooth exterior of the glaze.

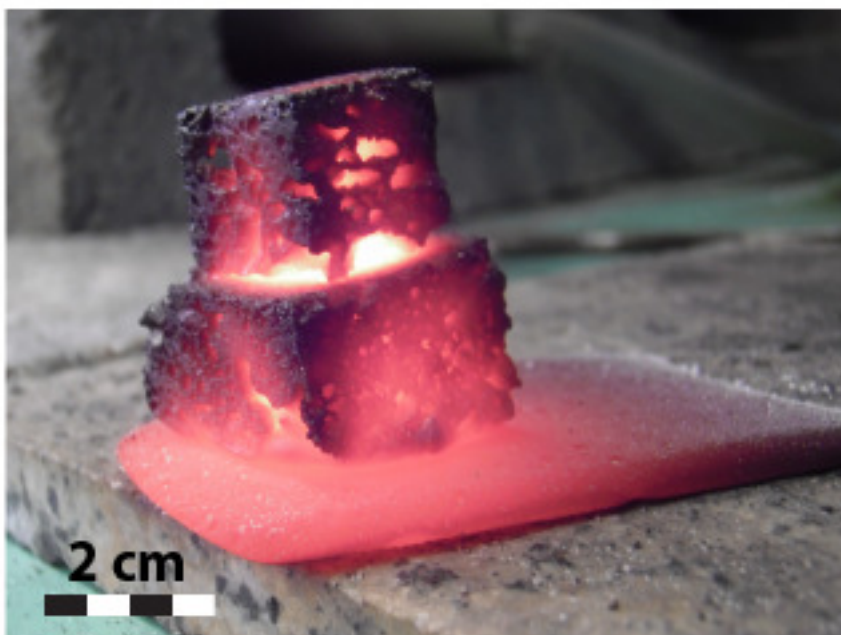


Figure 8. Cubes of sample stacked on a graphite plate. These had been heated in a tube furnace at  $1130^{\circ}\text{C}$  for 30 min, then were cooled below  $300^{\circ}\text{C}$  at cooling rates between 1 and  $10^{\circ}\text{C}/\text{min}$ .

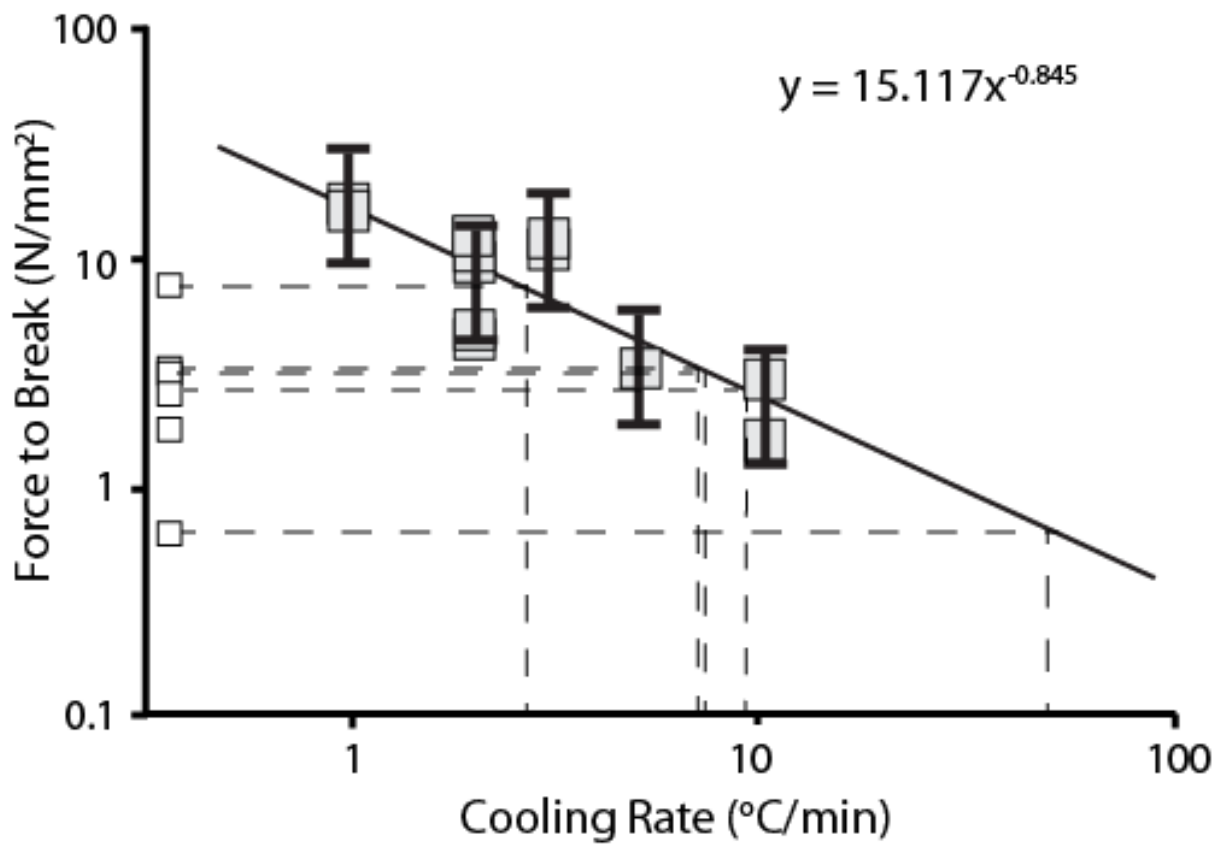
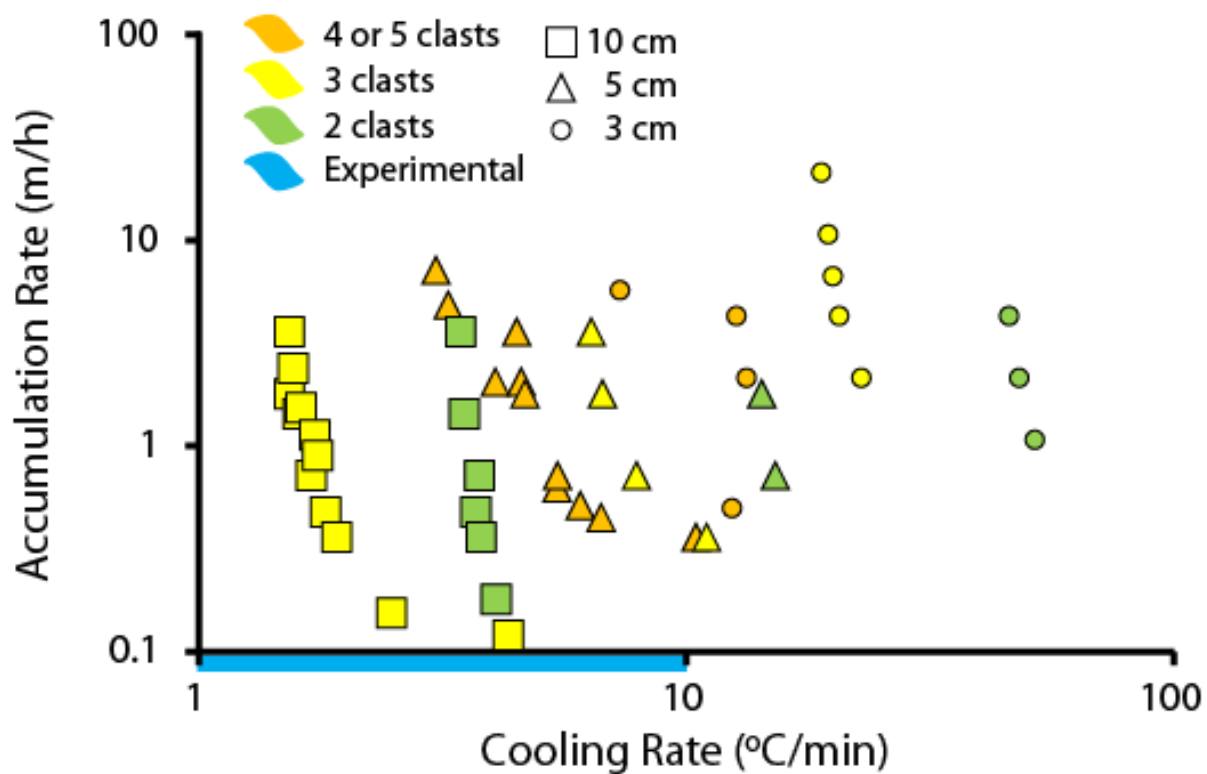


Figure 9. The tensile strength of artificial welds shows a strong anticorrelation to the cooling rate of spatter. Experiments are in grey squares and natural samples in white squares connected by dashed lines to the line fitted to the experimental data. Error bars are equal to 1 standard deviation of the 5 experiments repeated at a cooling rate of 2°C/min. All other repeats were below this standard deviation.



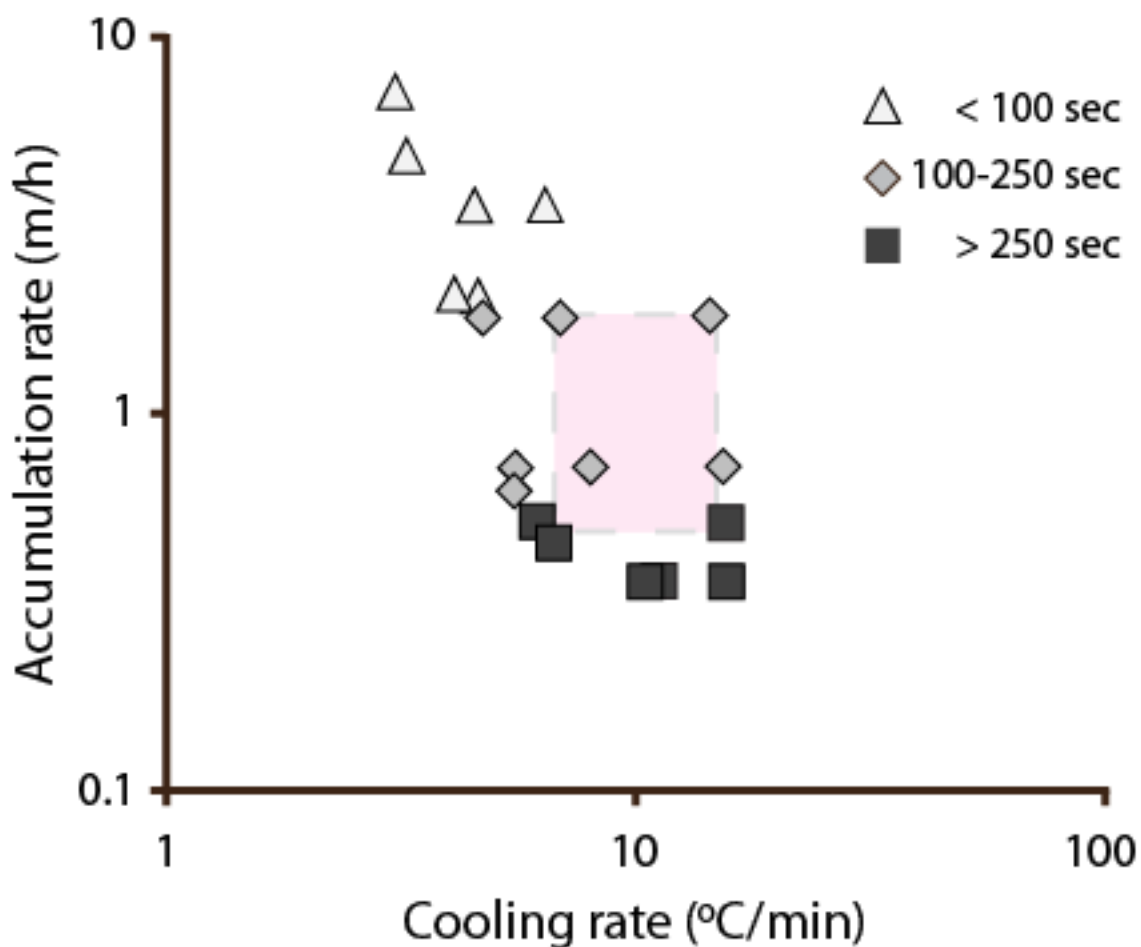


Figure 11. Model results for cooling and accumulation rates for 5 cm clasts, which is representative of clasts in the Blowouts at Devil's Garden. The symbols represent the frequency of deposition of clasts, the higher the frequency, the higher the accumulation rate. Light grey triangles represent runs with less than 100 seconds between clasts, dark grey diamonds :100-250 seconds, and black squares: intervals of greater than 250 seconds. The box outlines our estimates of the cooling regime of the natural samples from Devil's Garden.

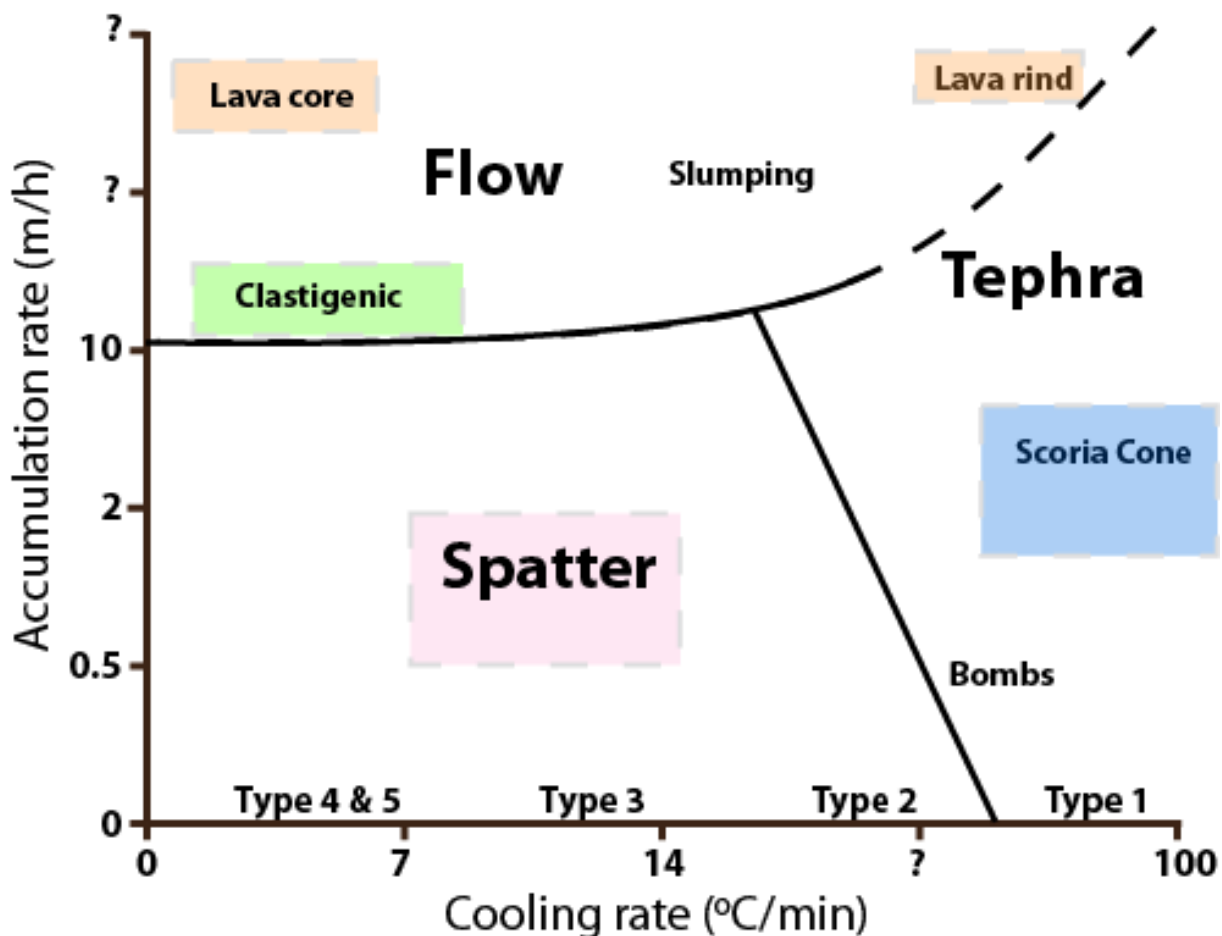


Figure 12. Schematic diagram for explosive basaltic products modified from Sumner et al. 2005. The cooling and accumulation rates from the spatter (pink box) in this study, clastogenic estimates from Sumner (1998) in the green box, scoria cone calculations (Riedel et al. 2003) in the blue box, and lava flow calculations in the orange boxes (Nichols et al., 2009, Bowles et al., 2005, Gottsmann & Dingwell 2004, Cashman 1999) allow us to assign values to this diagram. The exact locations of the lines are not yet known, and the axis are not yet to scale.